

Applications in Optical Coherence Tomography and Advances into a Photonic Integrated Device

Bernardo de B. C. Kyotoku

March 12th 2011

Abstract

Optical coherence tomography is a non-invasive imaging technique that uses non-ionizing infrared radiation to probe few millimeter depth of target at resolution of few micrometers. Here we expose the theoretical basis to understand the technique. The text covers the two varieties of OCT — time domain and frequency domain— and describe three applications of this technique to dentistry: a) One in the evaluation of crack propagation in fiber reinforced polymers used for dental restoration; b) The imaging of remains dentin and pulp chamber after dentin excavation for the purpose of measurement of dentin thickness, and c) a clinical evaluation of the integrity of dental restoration. In all these applications, OCT has outstanding imaging results and provides semiquantitative insight into the dental structure.

With the aim of developing optical coherence tomography integrated to a chip, we expose the theoretical basis of integrated photonics platform. After literature review, we detected that no integrated spectrometer, and OCT component, with the needed specifications exists. We, then, developed a spectrometer with the necessary features. This was possible due the creation of novel spectrometer architecture based on the combination of a ring resonator and a diffraction grating spectrometer.

Resumo

Tomografia por coerência óptica (OCT) é uma técnica de imageamento não invasiva que usa radiação infravermelho para sondar alguns milímetros the profundidade de um alvo com um resolução de poucos micrômetros. Aqui, nós expomos a base teórica para entender a técnica. O texto cobre as duas variedades de OCT — domínio temporal e domínio da frequência — e descreve três aplicações da técnica em odontologia: a) Um na avaliação the propagação rachaduras em polímeros reforçado com fibra usado em restauração dental; b) O imageamento da sobra de dentina e cavidade pulpar após excavação da dentina, com o propósito de medir a espessura da dentina, e c) uma avaliação clínica da integridade de restaurações dentais. Em todas essa aplicações, OCT gerou imagens marcantes e forneceu informações semiquantitativas sobre a estrura dentária.

Com o objetivo de desenvolver um sistema de tomografia óptica integrada em um chip. Nós expomos a base teórica da plataforma de fotônica integrada. Após uma revisão literária, nós descobrimos que não existe especlômetro integrado com a especificações necessárias para uso em OCT. Nós, então, desenvolvemos um especlômetro com a características necessárias. Isso foi possível devido a uma nova arquitetura de especlômetro baseada na combinação de um ressoador em anel e um especlômetro de grade de difração.

Contents

Introduction	1
1 Time Domain OCT	3
1.1 Theory	3
1.1.1 Michelson interferometer	4
1.1.2 Optical interferometry with coherent light	5
1.1.3 Low-coherence interferometry	6
1.1.4 Low coherence interferometry with multi-layer structures	7
1.1.5 Detector signal	8
1.2 Fourier delay line TDOCT	9
1.3 Implementation	10
1.4 Fourier delay line alignment	11
2 Fourier Domain OCT	13
2.1 Overview of Fourier domain OCT	13
2.2 Frequency domain OCT	15
2.3 Full range complex imaging reconstruction	17
2.4 First spectral radar implementation	18
2.5 Second spectral radar implementation	19
2.5.1 Spectrometer	20
2.5.2 Testing	20
3 Applications in Optical Coherence Tomography	21
3.1 Fiber reinforced composite analyses	21
3.1.1 Motivation	21
3.1.2 Conclusions	24

3.2	Imaging of dentin and pulp chamber by OCT	24
3.2.1	Materials and methods	25
3.2.2	Results	26
3.2.3	Conclusion	29
3.3	Clinical use of OCT to evaluate integrity of dental restorations	29
3.3.1	Introduction	30
3.3.2	Material and methods	30
3.3.3	Results	32
3.3.4	Discussion	35
3.3.5	Conclusion	38
4	Photonic Integrated Circuits	41
4.1	Broad picture	41
4.2	Slab waveguide	42
4.3	Rectangular waveguide	45
4.4	Ring resonators	46
4.5	Material optical properties	48
4.5.1	Material dispersion	49
4.5.2	Thermo optic effect	49
5	Diffraction Grating Spectrometers	51
5.1	Kirchhoff's diffraction theory	51
5.2	Diffraction grating	53
5.2.1	Free spectral range	57
5.3	Planar devices	58
5.4	Spectrometer architectures	59
5.4.1	Czerny-Turner	59
5.4.2	Rowland	61
5.4.3	Arrayed Waveguide Grating (AWG)	61
5.5	Grating illuminated by a gaussian beam	62
5.6	Aberrations	64
5.6.1	Aberration free conditions	65
5.6.2	One point stigmatic correction	66

5.7	Fresnel-Kirchhoff model	66
5.8	Numerical simulation of spectral defects and aberrations using Fresnel-Kirchhoff model	68
5.9	Implementation	68
5.9.1	Design	68
5.9.2	Effective index dispersion	71
5.9.3	Fabrication	72
5.9.4	Testing setup	73
5.9.5	Results	74
5.9.6	Conclusion	75
6	Ring Enhanced Spectrometer	77
6.1	Device theory	77
6.2	Design	78
6.3	Fabrication	78
6.4	Testing setup	80
6.5	Increasing channel density	82
6.6	Application of time serialization	84
6.7	Results	85
6.8	Device comparison	86
6.9	About the DG spectrometer channels spacing and resonator FSR mismatch	86
6.10	Conclusion	87
Bibliography		87
A Huygens-Fresnel Diffraction		89
A.1	Numerical calculation	89
A.2	Small aperture approximation	90
A.3	Numerical program validation	90
B Fourier transform		93
B.1	Relation	93
B.2	Common Fourier transforms	94

Introduction

In the middle of 2005, I started working in Prof. Anderson Gomes research group. At the time, my first assignment was to make improvements to the optical coherence tomography (OCT) system available, a time domain optical coherence tomography (TDOCT) system. The delay line was composed by a mirror that was scanned using a DC motor. Each scan would take about half a minute to complete. A whole image needed 2 hours to be acquired. During the acquisition time, the lab needed to be in silence. And the final image could only be seen after the whole acquisition was done. Because of the acquisition time, *in vivo* imaging was out of question. It used a table top femtosecond laser as the light source, and therefore, it could not be moved unless you take the whole laser with you. The system would misalign frequently, therefore a long trying period was needed to operate the system. Fast forward to today, we built a spectral radar optical coherence tomography (SROCT) which can acquire an image in few seconds. Clinical trials have been performed. The system can be transported anywhere in a car by a single person.

In 2008 we started an effort to integrate the whole OCT system into a single chip. For this we started a cooperation with prof. Michal Lipson from Cornell University. She was leading her research group to develop photonics integrated in silicon chips component and systems. I was suppose to leverage the group technical knowledge to build the desired device. We quickly learned that no integrated spectrometer with the specifications needed to compose a OCT has ever been made. So we set to design such component. After two years we were able to achieve an integrated spectrometer with unprecedent resolution and compactness.

This thesis is divided in two parts. The first part, comprised of the first three chapters, concerns only optical coherence tomography. There are two modalities of OCT, time or frequency domain. And a review of each modality is given in the first two chapters. In its respective chapter, the implementations of each modality is described. In the third chapter we present three applications where these OCT systems were used. In the first application we use OCT to evaluate crack evolution in fiber reinforced polymers after mechanical cycling. The main used of this material is as a teeth prosthetic. We showed the possibility of OCT to non destructively evaluate of the prosthetic integrity. In the second application we report the generation of images of the remaining dentin and pulp chamber of *in vitro* human teeth. Last, in the

third chapter we report a clinical assessment of dental restoration in humans, where lesions and failed restorations were successfully identified where conventional visual and X-ray examination failed.

The second part of the thesis deals with subject needed in the design of spectrometers integrated on silicon chips. Fourth chapter provides a review on chip photonics circuit, laying the theoretical basis used throughout the remaining of the thesis. In the fifth chapter, the basics of free space and integrated spectrometers is given, and a first implementation of an integrated device is described. In the sixth chapter we describe the principle and details of the implementation of a technique that greatly improves the resolution and compactness of the integrated spectrometer.

Chapter 1

Time Domain Optical Coherence Tomography

I can only show you the door. You have to walk through it.

Morpheus

Superman's ability to see through walls always fascinated us. We have walked great lengths to achieve the same ability. Rottingen X-rays, ultrasound, nuclear magnetic resonance, computed tomography are some of the attempts to do this. Unfortunately any technique has a limited operational range which it works. X-rays cannot distinguish small density contrast, and is highly carcinogenic. Ultrasound does not achieve the same resolution possible by X-rays, nor can it achieve high velocity contrast. Although, in principle the problem could be circumvented, nuclear magnetic resonance does not work on non hydrogenated targets. Furthermore, its high maintenance cost restricts its use to high value applications. Here we discuss another prospective method, called optical coherence tomography. This technique is based on infrared interferometric measurements. It features, resolution on the order of its probing wavelength, real-time video imaging capability. The observable depth is limited by the absorption and scattering of the material being probed, which is typically a few millimeters for biological samples.

1.1 Theory

In OCT, the kind of interferometry used is the low-coherence type. In this section, we describe how low-coherence interferometry is used to measure the distance of an object with more than one reflecting surface.

1.1.1 Michelson interferometer

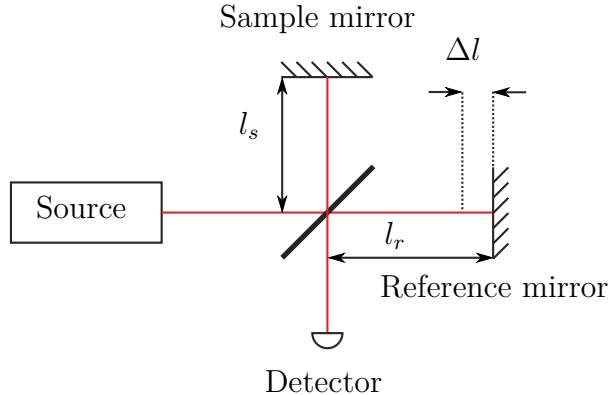


Figure 1.1.1: Michelson interferometer

Consider the interferometer shown in figure 1.1.1. To simplify the analysis, ignore the light polarization and dispersion effects. A light source emits a radiation, whose electric field is described by $E_{\text{in}}(t)$, upon a beam splitter. This light is divided and a fraction D of its power is directed to mirror S with reflectivity R_s . The light is reflected and returns to the beam splitter, where a fraction $(1 - D)$ of its power goes to the detector. Similarly, in the other interferometer arm, $(1 - D)$ of the light emitted by the light source is redirected to the mirror R_r , which is reflected and returns to the beam splitter, where a fraction D of this light is redirected back to the detector. The electric field at the detector can be described by

$$E_{\text{out}} = \sqrt{K_0} E_{\text{in}}(t - \tau_s) - \sqrt{K_r} E_{\text{in}}(t - \tau_r), \quad (1.1.1)$$

where $K_i = R_i D (1 - D)$ is the light power fraction that is shined to the detector and τ_i is the time the light takes to go from the beam splitter to the mirror i and back.

The relationship between the output light intensity $\langle I \rangle$ and the mean electric field is:

$$\langle I \rangle = \left\langle \frac{|E(t)|^2}{2\eta_0} \right\rangle, \quad (1.1.2)$$

where $\eta_0 = \sqrt{\frac{\mu_0}{\epsilon_0}}$ is the free space impedance. Using 1.1.1 and 1.1.2, we get the intensity at the detector

$$\langle I \rangle = \langle I_{\text{DC}} \rangle + \sqrt{K_s K_r} \Re(\Gamma(\tau_{s,r})) \quad (1.1.3)$$

where $\tau_{r,s} = \tau_s - \tau_r$ and $\Re(x)$ is the real part of x . We define the autocorrelation function for the electric field as

$$\Gamma(\tau) = \frac{E(t - \tau) E^*(t)}{\eta_0} \quad (1.1.4)$$

and

$$\langle I_{DC} \rangle = \sum_j K_j \langle I_0 \rangle, \quad (1.1.5)$$

where $\langle I_0 \rangle = \left\langle \frac{|E_0(t)|^2}{2\eta_0} \right\rangle$ is the mean light intensity that leaves the source, which in this case is constant. More specifically, it is of interest that the light source should be stationary in the wide sense, which means

1. $\langle E(t) \rangle$ is independent of t .
2. $\langle E(t_1) E^*(t_2) \rangle$ depends only on the difference $\tau = t_2 - t_1$, not the absolute values of t_1 and t_2 .

1.1.2 Optical interferometry with coherent light

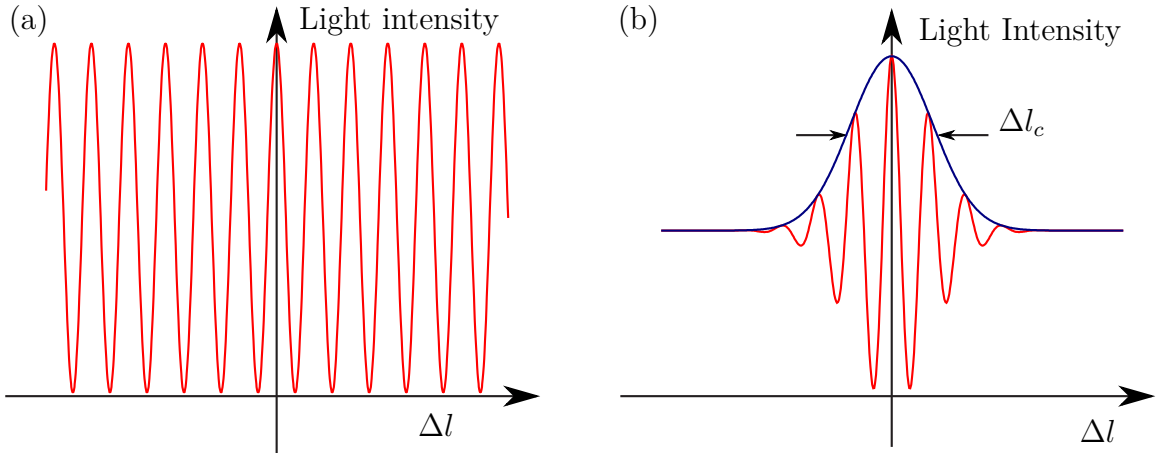


Figure 1.1.2: Light intensity at the interferometer output for input source of (a) coherent light. (b) light with coherence length Δl_c .

If the light is perfectly coherent (i.e. monochromatic), then its electric field can be described as $E_{in}(t) = E_0 e^{-i2\pi\nu t}$ where ν is the optical frequency and E_0 is the field amplitude. Replacing $E_{in}(t) = E_0 e^{-i2\pi\nu t}$ in equation 1.1.4 and using 1.1.3, we get

$$\langle I \rangle = \langle I_{DC} \rangle + 2 \langle I_0 \rangle \sqrt{K_s K_r} \cos(2\pi\nu\tau_{s,r}), \quad (1.1.6)$$

or, using $\lambda = c/\nu$ and $\Delta l = \frac{c}{2}(\tau_s - \tau_r)$

$$\langle I \rangle = \langle I_{DC} \rangle + 2 \langle I_0 \rangle \sqrt{K_s K_r} \cos\left(2\pi \frac{\Delta l}{\lambda/2}\right). \quad (1.1.7)$$

Equation 1.1.7 says that the light intensity in the detector varies periodically with the interferometer arm length difference Δl , with period $\lambda/2$. In special, in the case where $K_s = K_r$ we

get points of zero intensity, as illustrated in 1.1.2(a).

1.1.3 Low-coherence interferometry

In practice, the longitudinal coherence of a light source is always limited. In a real case, overlapped with the rapid intensity oscillation with period $\lambda/2$, we will notice a gradual decrease of oscillation amplitude. The full width a half maximum of the oscillation envelope is called coherence length Δl_c , which we are going to show to be inversely proportional to the light source bandwidth.

Consider the interferometer in figure 1.1.1, now illuminated with a low coherence light, whose spectrum lineshape is described by $G(\nu)$. The mean light intensity at the detector can be described by the equation 1.1.3. According with the Wiener-Khinchin theorem¹², the autocorrelation of the signal and its power spectrum density (PSD) are related by a Fourier transform

$$G(\nu) = \int_{-\infty}^{\infty} \Gamma(\tau) e^{i2\pi\nu\tau} d\tau \quad (1.1.8)$$

$$\Gamma(\tau) = \int_{-\infty}^{\infty} G(\nu) e^{-i2\pi\nu\tau} d\nu \quad (1.1.9)$$

If the light source PSD lineshape is Gaussian

$$G(\nu) = \frac{\langle I_0 \rangle}{\Delta\nu} \sqrt{\frac{4 \ln 2}{\pi}} e^{-4 \ln 2 \left(\frac{\nu - \nu_0}{\Delta\nu} \right)^2}, \quad (1.1.10)$$

where ν_0 is the central optical frequency, $\Delta\nu$ is the full width half maximum (FWHM) of the Gaussian. The autocorrelation of this spectrum is

$$\Gamma(\tau) = \langle I_0 \rangle e^{-i2\pi\nu_0\tau} e^{-\ln 2\tau^2/\Delta\tau_c^2} \quad (1.1.11)$$

where $\Delta\tau_c = \frac{2 \ln 2}{\pi \Delta\nu}$ is called the *coherence time*, or alternatively using $\tau = \frac{2\Delta l}{c}$

$$\Gamma(\Delta l) = \langle I_0 \rangle e^{-i2\pi \frac{\Delta l}{\lambda_0/2}} e^{-\ln 2 \frac{\Delta l^2}{(\Delta l_c/2)^2}} \quad (1.1.12)$$

where $\Delta l_c = \frac{2 \ln 2 c}{\pi \Delta\nu} = \frac{2 \ln 2 \lambda_0^2}{\pi \Delta\lambda}$ is defined as *coherence length*. λ_0 the central wavelength. Replacing 1.1.12 on 1.1.3 we get

$$\langle I \rangle = \langle I_{SD} \rangle + 2 \langle I_0 \rangle \sqrt{K_s K_r} \cos \left(2\pi \frac{\Delta l}{\lambda_0/2} \right) e^{-i2\pi \frac{\Delta l}{\lambda_0/2}} e^{-\ln 2 \frac{\Delta l^2}{(\Delta l_c/2)^2}} \quad (1.1.13)$$

¹http://en.wikipedia.org/wiki/Wiener-Khinchin_theorem

²Goodman, *Statistical Optics*.

Equation 1.1.13 justifies the behavior of the light intensity at the interferometer output described in the beginning of section and illustrated in 1.1.2 (b). The cosine is responsible for the rapid oscillation and the Gaussian modulates the oscillation amplitude, which falls to half at a distance $\Delta l_c/2$. As described earlier, the coherence length is inversely proportional to the light spectrum. The specific power spectrum lineshape of the source alters the autocorrelation function, but the fact that the coherence length decreases with the increase of the power spectrum width of the light source is not altered.

1.1.4 Low coherence interferometry with multi-layer structures

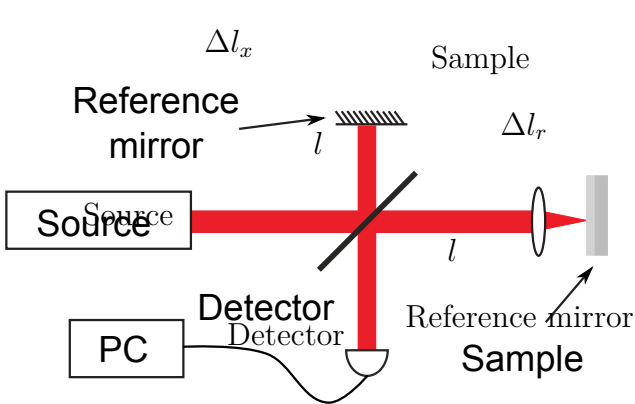


Figure 1.1.3: Interferometer with low coherence light source and micro-structured sample.

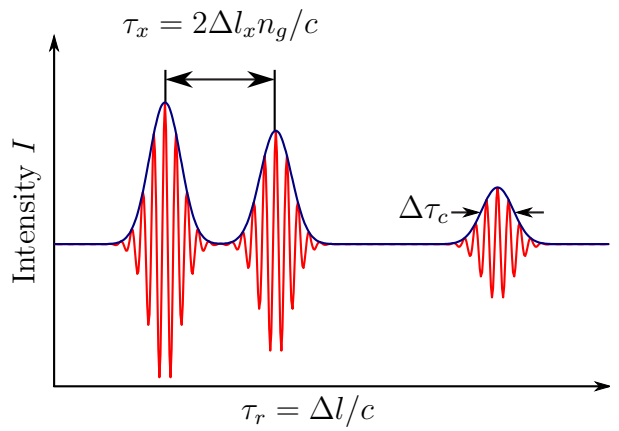


Figure 1.1.4: Intensity at detector as the reference arm is scanned.

To describe the reconstruction of the longitudinal image of a structure, we replace the s mirror by a sample with dielectric layers. The input beam is focused onto the sample surface, as shown in figure 1.1.3. We can model the electric field at the interferometer output coming from the sample arm as

$$E_s(t) = \sum_i K_i E_0(t - \tau_i), \quad (1.1.14)$$

where $E_0(t)$ is the light source field and $K_i = R_i(1 - D)D$, D being the beam splitter splitting ratio, R_i is the reflectivity of the i -th sample interface and τ_i is the round-trip time from the beam splitter to the i -th sample interface. The intensity at the detector will then be

$$\langle I \rangle = \left\langle \frac{|E_s(t) + E_r(t)|^2}{2\eta_0} \right\rangle = \langle I \rangle + \sum_i \sqrt{K_i K_r} \Re[\Gamma(\tau_{r,i})] \quad (1.1.15)$$

where $E_r(t) = K_r E(t - \tau_r)$ is the light electric field that comes from the reference mirror and $\tau_r = 2\Delta l/c$. For a sample shown in figure 1.1.3, the intensity as a function of the delay τ_r , will

be as shown in the black line in figure 1.1.4, what we call *interferogram*. In it, we can identify three packets, each corresponding to a light returning from each of the sample interfaces. The interval time between packages is equal to the time light takes to go from one interface to the other and return, $\tau_x = n_g \Delta l_x / c$, where n_g is the group index of the material that the light is propagating at.

An interferogram can be acquired by detecting the output light as the reference mirror is scanned, and this is denominated A-Scan. The detected electronic signal passes through an envelope detector circuit. This circuit eliminates the oscillation within the packets, leaving the envelope of the signal, as shown in red on the graph 1.1.4, to which we call *tomogram*. An image is made by translating the beam transversally to the beam direction and taking a tomogram after a chosen step size.

1.1.5 Detector signal

The mean current generated by the photo-diode can be described as

$$\langle i \rangle = \frac{e\eta}{\eta\nu_0} \langle P \rangle, \quad (1.1.16)$$

where $\langle P \rangle = A \langle I \rangle$ is the mean light power that hits the detector in the area A , η is the detector quantum efficiency, e is the electron charge and h is the Planck constant. If we scan the reference mirror at a velocity u_r in the low coherence interferometer described previously, the current will be

$$\langle i \rangle = \frac{e\eta}{\eta\nu_0} \left[\langle P_{DC} \rangle + 2 \langle P_0 \rangle \sqrt{K_s K_r} \cos(2\pi\nu_r t) e^{-i2\pi\frac{\Delta l}{\lambda_0/2}} e^{-\ln 2 \frac{u_r^2 t^2}{(\Delta l_c/2)^2}} \right], \quad (1.1.17)$$

where $\nu_r = \frac{u_r}{\lambda_0/2}$. To remove some noise in the detector current, the signal is filtered using an electronic pass band filter centered at ν_r with bandwidth B ,

$$B \approx \frac{u_r \Delta \nu}{c} \sqrt{\frac{\pi}{\ln 2}} \quad (1.1.18)$$

which removes the DC current due to the term $\langle P_{DC} \rangle$.

The electric peak current of the interference pattern at $\Delta l = 0$ is

$$\langle i \rangle = \frac{2e\eta}{h\nu_0} \langle P_0 \rangle \sqrt{K_r K_s}. \quad (1.1.19)$$

Equation 1.1.19 shows that the electric current is proportional to the square root of the light power fraction that returns form the sample K_s and the reference mirror K_r , which shows a heterodyne amplification of the signal coming from the sample.

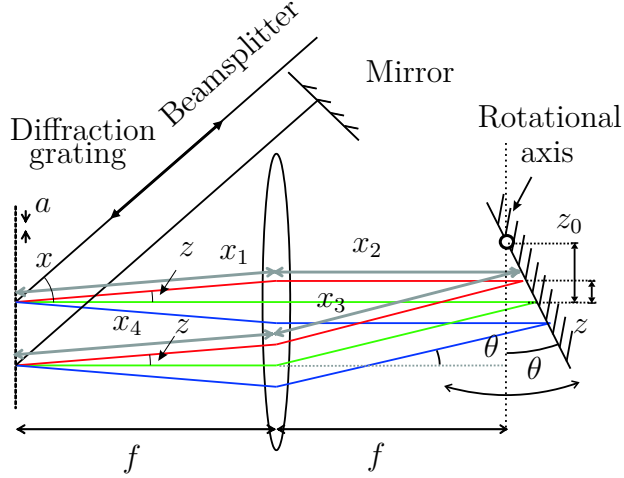


Figure 1.2.1: Fourier delay line schematics.

1.2 Fourier delay line TDOCT

One of the models of TDOCT built used a Fourier delay line. This delay line allows a high A-scan frequency. The basic idea consists of adding, to the light beam, a linear phase delay in the frequency domain, which in the time domain correspond to a temporal delay. This effect is produced by resolving spatially the light wavelength and adding a different time delay to each different wavelength by using a lens and a mirror, as shown in figure 1.2.1. The temporal delay to each optical frequency is³

$$\phi(\theta) = \frac{8\pi\nu z_0 \theta}{c} - \frac{8\pi f (\nu - \nu_0) \theta}{a\nu_0}, \quad (1.2.1)$$

where f is the lens focal length, a is the grating pitch, θ is the angle between the mirror surface and the lens plan, z_0 is the distance between the mirror rotation axis and the trajectory of the beam central optical frequency ν_0 . The effect of replacing the standard delay line by a Fourier delay line can calculated as follows. Considering the incoming beam in the reference arm as $E(t)$, whose spectrum amplitude is $g(\nu)$. Returning from the delay line the returning beam spectrum amplitude will be

$$\tilde{g}(\nu) = g(\nu) e^{i\phi(\theta)}, \quad (1.2.2)$$

and the electric field will be $\tilde{E}(t)$. The power intensity of the beam coming from both arms of the interferometer, as described at section 1.1.1, will be

$$\langle I \rangle = \frac{\langle \sqrt{K_0} E_0 (t - \tau_s) + \sqrt{K_r} E_0 (t - \tau_r) \rangle}{2\eta_0} \quad (1.2.3)$$

$$= \langle I_{DC} \rangle + \langle I_0 \rangle \sqrt{K_s K_r} \Re[\Xi(\tau)], \quad (1.2.4)$$

³Rollins et al., “In vivo video rate optical coherence tomography”.

where τ is the delay due to the path-length difference between the interferometer arms when $\phi = 0$, and

$$\Xi(\tau) = \langle E(t) \tilde{E}^*(t - \tau) \rangle \eta_0, \quad (1.2.5)$$

is the cross correlation between $E(t)$ and $\tilde{E}(t)$. According to the cross correlation theorem

$$\Xi(\tau) = \int_{-\infty}^{\infty} \langle g(\nu) \tilde{g}^*(\nu) \rangle e^{-i2\pi\nu\tau} d\nu, \quad (1.2.6)$$

knowing that $|g(\nu)|^2 = G(\nu)$. Using 1.2.2, 1.2.1 and 1.2.4

$$\langle I \rangle = \langle I_{DC} \rangle + \langle I \rangle \sqrt{K_r K_s} \cos \left[2\pi\nu_0 \left(\tau + \frac{4}{c} z_0 \theta \right) \right] \Gamma \left[\tau + 4 \left(\frac{z_0}{c} - \frac{f}{a\nu_0} \right) \theta \right] \quad (1.2.7)$$

where $\Gamma(t)$ is the same as defined before. From the auto-correlation function argument, we observe that the group delay τ_g varies linearly with the mirror angle *theta*

$$\frac{d\tau_g}{d\theta} = 4 \left(\frac{z_0}{c} - \frac{f}{a\nu_0} \right), \quad (1.2.8)$$

and the phase delay τ_f we can obtain from the cosine argument

$$\tau_f = \frac{4z_0}{c}\theta. \quad (1.2.9)$$

Varying the group delay τ_g , by changing θ , we execute an axial scan, while the variation on the phase delay τ_f causes an oscillation of any constructive interference. The A-scan is described by

$$\Delta l_g = \tau_g \frac{c}{n_g} = \frac{4}{n_g} \left(z - \frac{f\lambda_0}{a} \right) \Delta\theta. \quad (1.2.10)$$

During scan the carrier frequency is dependent on the phase delay scan and will be equal

$$\nu_f = \frac{8\pi\nu_0 z_0}{c} \frac{d\theta(t)}{dt}, \quad (1.2.11)$$

which is of interest when choosing the frequency at which the signal will be filtered, the signal bandwidth will be

$$B = 2\Delta\nu \sqrt{\frac{\pi}{\ln 2}} \left(\frac{z_0}{c} - \frac{f}{a\nu_0} \right) \frac{d\theta(t)}{dt}. \quad (1.2.12)$$

1.3 Implementation

Figure 1.3.1 shows the schematic of the time domain OCT system operating at the central wavelength of 1280 nm, maximum average power 5 mW, delivered by a superluminescent diode

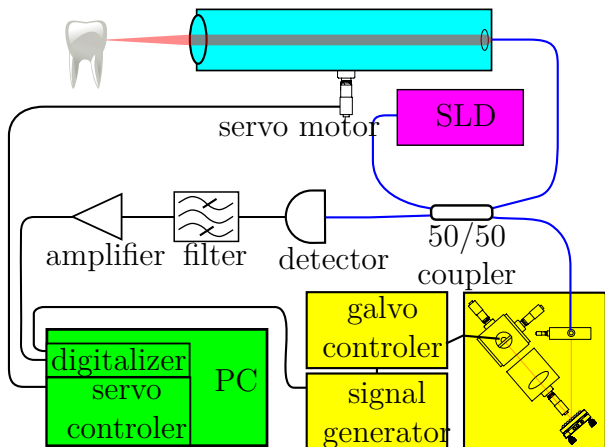


Figure 1.3.1: OCT setup with Fourier delay line.

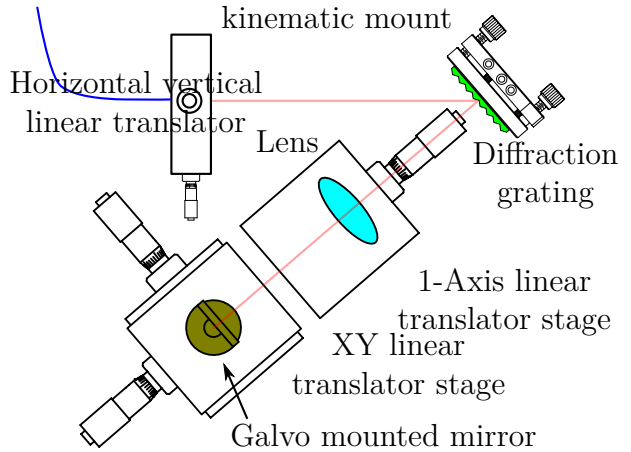


Figure 1.3.2: Fourier delay line setup.

model no. SLD-571, SUPERLUM, Moscow, Russia, with a 64.6-nm bandwidth, which represents an axial resolution of 11 μm . As with the system in figure 1.1.3, we have a Michelson interferometer, but in this case the delay line is a Fourier domain delay line⁴, shown in detail in figure 1.3.2. The recombined beams are fed into a photodetector and the signal is sent to a band-pass filter, a transimpedance amplifier and finally to a computer digitalizer, NI PCI-5122. The galvo motor signal is produced by a signal generator Agilent. The signal generator trigger signal is also sent to the PC digitalizer. The sample arm is carried by a 1-D linear translation stage powered by a computer controlled servo DC motor (Z625B, Thorlabs), and is responsible for beam transversal scan. The galvo scan rate was 100 Hz, while the transversal scanning speed was 1 mm/s. Envelope detection was performed computationally using a band pass filter.

1.4 Fourier delay line alignment

Referring to figure 1.3.2 a fiber optic coupler facilitated the system alignment since the alignment of the delay line could be uncoupled from the other arms. The first thing that needs to be done is to properly align the Fourier delay line (FDL) making sure that the first order diffraction central wavelength is orthogonal to the grating. This can be done by exploring the fact that the second order diffraction of the central wavelength must return to the input. Monitoring the return light using a fiber optic coupler connected to a spectrometer, the grating angle can be adjusted until the returning wavelength is the central wavelength. The galvo mirror can then be mounted and aligned such that the diffracted light central wavelength after reflection on the galvo mirror couples back to the fiber optics. Lens can then be placed and adjusted

⁴Cense et al., “Ultrahigh-resolution high-speed retinal imaging using spectral-domain optical coherence tomography”.

in the direction transversal to the beam until the the beam couples back to the fiber. Galvo mirror and lens should be roughly placed on the axial position. Fiber optic coupler should then be translated vertically by a few millimeters and the mirror M can be placed and aligned such that the returning beam couples back to fiber. FDL is roughly aligned to be placed in the interferometer. With a test sample, a polished surface, placed at half the FDL path-length distance from the sample fiber optic coupler. Setup the OCT interferometer with the output detector and a test sample and find an interference on a oscilloscope. Lens and galvo mirror axial rough adjustment will cause severe group velocity dispersion (GVD) therefore do not expect clear interference signal. Couple the oscilloscope to AC and amplify the as much as the noise level clearly. After the interference is found, adjust the lens and galvo mirror axial position until the interference is as sharp as possible. The Fourier delay line is now adjusted.

Chapter 2

Fourier Domain Optical Coherence Tomography

In 1995, Fercher et al.¹ modified Wolf's solution of the optical inverse scattering problem to the one-dimensional problem of length measurement. The solution allowed the reconstruction of the scattering target structure through the Fourier transform of the backscattered light field for a bounded range of wavelengths. Due to the high frequency of light, it is not possible to directly measure its field. But using interferometric methods, one can back calculate the field, except for an ambiguity of π in the field phase. This method is known as Fourier domain optical coherence tomography (FDOCT). By measuring the contribution of each wavelength separately a sensitivity higher than with TDOCT can be achieved. This enabled the achievement of clinical 3D imaging with ultra-high resolution and in-vivo.

The first section of this chapter contains a rough picture of how FDOCT works, followed by a more rigorous modeling and description of two variants of FDOCT. A section on how to deal with the field phase π ambiguity is also presented. The chapter is completed with details of one implementation of a FDOCT system.

2.1 Overview of Fourier domain OCT

Before going through a more rigorous derivation, we will show a more intuitive picture on how frequency domain OCT reconstructs its image. Consider the Michelson interferometer illustrated on 2.1.1 and described in section 1.1.1. It was shown in section 1.1.1 that the light intensity in the interferometer output is described by

$$\langle I \rangle = \langle I_0 \rangle + \frac{\sqrt{K_r K_s}}{\eta_0} \cos(2\pi\nu\tau_{r,s}). \quad (2.1.1)$$

¹Fercher et al., "Measurement of intraocular distances by backscattering spectral interferometry".

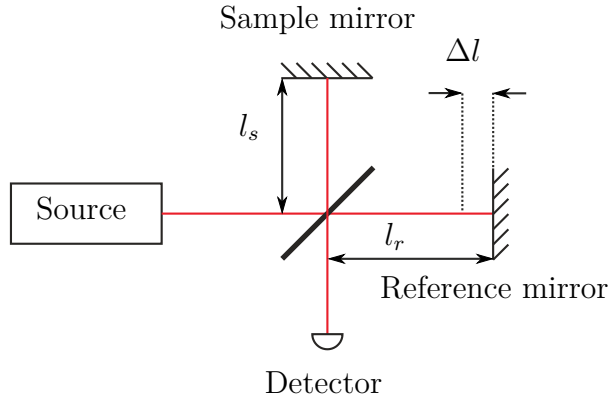


Figure 2.1.1: Michelson interferometer.

Notice that the equation has a dual behavior relative to optical frequency ν and the time delay τ . Usually, it is easier to vary the interferometer arm length keeping the optical frequency (or wavelength) constant and observe the light intensity at the interferometer output. We will then see interference fringes as graph on figure 2.1.2. But if we keep the arms length difference constant and equal $\Delta l = c\tau/2$, we can rewrite equation 1.1.7 as

$$\langle I \rangle = \langle I_0 \rangle + \frac{\sqrt{K_r K_s}}{\eta_0} \cos \left(2\pi \frac{2\Delta l}{c} \nu \right). \quad (2.1.2)$$

Notice that the oscillation period is inversely proportional to Δl . Therefore, if we know the period of the intensity oscillation in optical frequency $\Delta\nu$, we can calculate the difference of optical path-length between the interferometer arms, $\Delta l = \frac{c}{2\Delta\nu}$.

If we put dielectric sample in place of a sample mirror, as shown in figure 2.1.3, instead of getting a simple intensity oscillation, we will obtain a superposition of several sinusoids described by the equation below

$$\langle I \rangle = \langle I_0 \rangle [1 + F_{r,1} \cos(2\pi\tau_{r,1}\nu) + F_{r,2} \cos(2\pi\tau_{r,2}\nu) + F_{1,2} \cos(2\pi\tau_{1,2}\nu)]. \quad (2.1.3)$$

The second and the third terms in the brackets are related to the interference between the light from the reference mirror and the interfaces 1 and 2. The fourth term is due to the interference of the interfaces 1 and 2 between themselves. As can be seen in figure 2.2.1, it is difficult to identify the frequencies of each harmonic associated with the interference of light coming from two interfaces. However, we can identify the contribution of each harmonic by taking the Fourier transform of the power spectrum as illustrated in figure 2.2.2.

The presence of the peaks due to the interference between the two interfaces of the sample are called *self-interference*, and as can be seen, it creates reconstruction artifacts that obstruct

the reconstructed image. However, note that the distance of the peak is equal to the sample thickness, and is independent of the distance between the interfaces and the reference distance. Therefore, if the distance of the sample surface to the reference is greater than the sample thickness $\Delta l_{1,r} > \Delta l_{1,2}$, all peaks after the position $\Delta l_{1,2}$ are free of these artifacts. In the following section we will show other methods to suppress these artifacts.

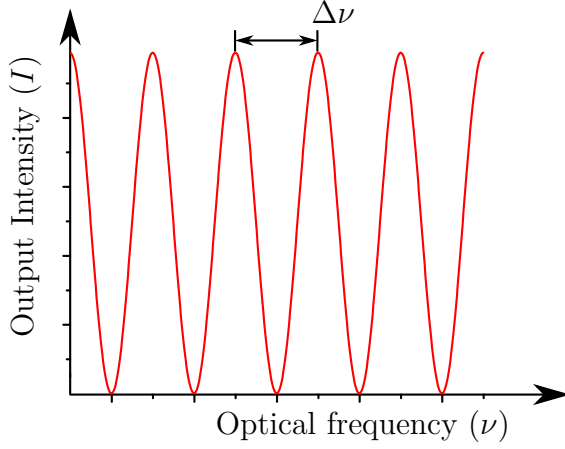


Figure 2.1.2: Light intensity at the Michelson interferometer output as a function of the source optical frequency. The interferometer arms length difference can be calculated as $\Delta l = \frac{c}{2\Delta\nu}$.

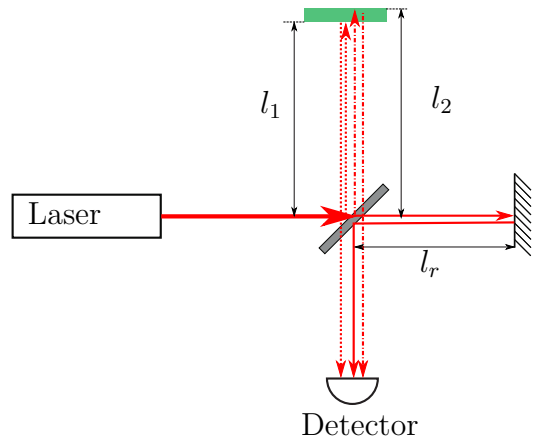


Figure 2.1.3: Michelson interferometer with semi-transparent sample.

In principle Fourier transform assumes the integration for infinite spectral range. In practice this is not possible, and this limitation causes the decrease of the precision with which the oscillation frequencies are estimated and therefore decreasing the resolution to which we can observe the interface.

In the shown example, the output spectrum is measured by varying the light source wavelength. This type of operation is called swept source. However, it is possible to use a light source with broad spectrum, and distinguish the contribution of each optical frequency using a spectrometer principle as in the spectral radar OCT.

2.2 Frequency domain OCT

Consider the interferometer depicted in 2.1.3. As explained in the TDOCT chapter the electric field at the interferometer output can be modeled as

$$E(t) = \sqrt{K_r} E_0(t - \tau) + \sum_i \sqrt{K_i} E_0(t - \tau_i) \quad (2.2.1)$$

where K_j is the fraction of the light power coming from the point j and arriving at the interferometer output, and τ_j is the time the light take to go and return from the beam-splitter to the point j , where j can be r or i . The autocorrelation function of the output light electric field $\Gamma(\tau) = \langle E(t) E^*(t - \tau) \rangle$

$$\Gamma(\tau) = \left[K_r + \sum_i K_i \right] \Gamma_0(\tau) + \sum_i K_{r,i} \Gamma_0(\tau + \Delta\tau_{r,i}) + \sum_i K_{r,i} \Gamma_0(\tau - \Delta\tau_{r,i}) + \sum_{i \neq j} K_{i,j} \Gamma_0(\tau - \Delta\tau_{i,j}), \quad (2.2.2)$$

where $K_{a,b} = \sqrt{K_a K_b}$, $\Delta\tau_{a,b} = \tau_a - \tau_b = \frac{2\Delta l_{a,b}}{c}$ and $\Gamma_0(\tau) = \langle E_0(t) E_0^*(t - \tau) \rangle$. And a and b can be either r, i or j .

Before describing Γ , it is worth to recall that Γ_0 is a complex function and therefore so is Γ . However, we are interested on the $|\Gamma|$. In section 1.1.3 we discussed the types of $|\Gamma_0|$ and how they are related to the light source power spectral density. For this section it is just worth remembering that it is a peak function centered at argument.

The first term of the equation 2.2.2 will give rise to a peak centered at the origin, called the DC term. The second term is constituted of several peaks each centered at its respective delays $\Delta\tau_{r,i}$ and height proportional to its reflectance. This is the information which we are going to use in the image reconstruction. The third them as repeated information of the second term but inverted relative to the origin, called *mirror image*. The fourth term are self interferences, due to the interference of backscattered light in the sample only.

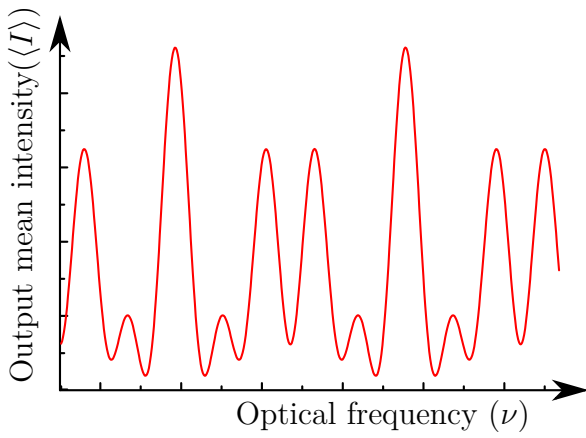


Figure 2.2.1: Light intensity at the Michelson interferometer with a semi-transparent sample as a function of the source optical frequency ($\langle I \rangle$).

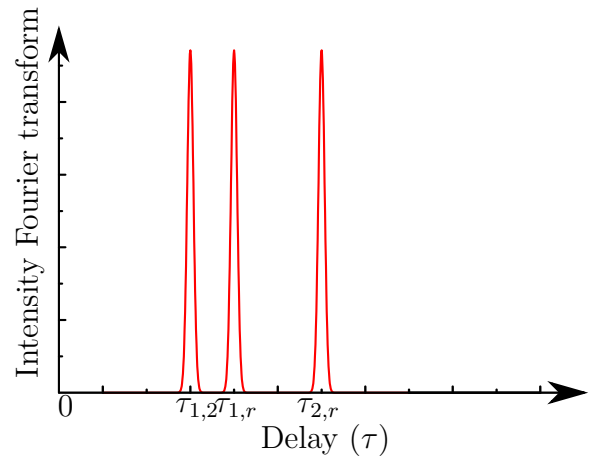


Figure 2.2.2: Fourier transform of $\langle I \rangle$. Each peak is due to interference between the light coming from the combination of any two interfaces.

The principle of FDOCT is based on calculating the autocorrelation function of the interferometer output light from its power spectrum density. According to the Wiener-Khinchin theorem the autocorrelation of a function and its power spectral density are related by a Fourier Trans-

form. Therefore, the power spectral density at the interferometer output is

$$G(\nu) = G_0(\nu) \left[\left(K_r + \sum_i K_i \right) + 2 \sum_i K_{r,i} \cos(2\pi\nu\Delta\tau_{r,i}) + 2 \sum_{i \neq j} K_{i,j} \cos(2\pi\nu\Delta\tau_{i,j}) \right], \quad (2.2.3)$$

where G_0 is the light source PSD. We see that the interferometer output PSD is composed of interference fringes whose frequencies grows with the delays $\Delta\tau_{a,b}$, and is modulated by a envelope equal to the input light PSD.

2.3 Full range complex imaging reconstruction

The modulus of the autocorrelation of the interferometer output light can be calculated from the output PSD. But as stated before we are only interested in the second term of the auto-correlation function.

$$|\Gamma_2| = \sum_i K_{r,i} |\Gamma_0(\tau + \Delta\tau_{r,i})|, \quad (2.3.1)$$

Several methods were developed to extract the this term from the autocorrelation function. Each method having it own virtues and shortcomings in terms of processing power, additional equipment, sensitivity to sample motion (relevant for in vivo imaging). Here we describe the method we used, which was the *quadrature delayed spectrum*.

The method consists of acquiring the imaginary part of the two spectra, with the reference arm $\lambda_0/8$ shorter than the other. According with equation 2.2.3, if we add a small temporal delay $\delta\tau$ by changing the reference arm length by $\delta L = c\delta\tau/2$ the output spectrum will be

$$G_\delta(\nu) = G_0(\nu) \left[\left(K_r + \sum_i K_i \right) + 2 \sum_i K_{r,i} \cos(2\pi\nu\Delta\tau_{r,i} + 2\pi\nu\delta\tau) + 2 \sum_{i \neq j} K_{i,j} \cos(2\pi\nu\Delta\tau_{i,j}) \right], \quad (2.3.2)$$

if

$$2\pi\nu\delta\tau = -\frac{\pi}{2}, \quad (2.3.3)$$

then the output spectrum can be approximated to

$$G_\delta(\nu) = G_0(\nu) \left[\left(K_r + \sum_i K_i \right) + 2 \sum_i K_{r,i} \cos(2\pi\nu\Delta\tau_{r,i}) + 2 \sum_{i \neq j} K_{i,j} \cos(2\pi\nu\Delta\tau_{i,j}) \right]. \quad (2.3.4)$$

With the above spectrum at hand it is possible to make the complex Fourier transform. Straight Fourier transform will conserve the DC level and the auto-correlation terms. These terms can

be eliminated by subtracting a spectrum from another, leaving us with

$$\Gamma = |FT[G + iG_\delta] - FT[G_\delta + iG]| + |FT[G + iG_\delta]| - |FT[G_\delta + iG]|. \quad (2.3.5)$$

The above equation proposed by Gotzinger² is one used by us to obtain the tomograms in FDOCT setups.

For the condition 2.3.3, a delay varying linearly with optical frequency needs to be performed. Although there are ways to do it, we preferred to rely on the fact that optical frequency does not change much over the spectrum, and approximate 2.3.3 by $2\pi\nu_0\delta\tau = -\frac{\pi}{2}$. Due to this approximation there is a polychromatic phase error³ which we neglected in our device.

2.4 First spectral radar implementation

Two SROCT setups were built. The first version was built only with components available in the laboratory, while the required parts were acquired to implement the new design.

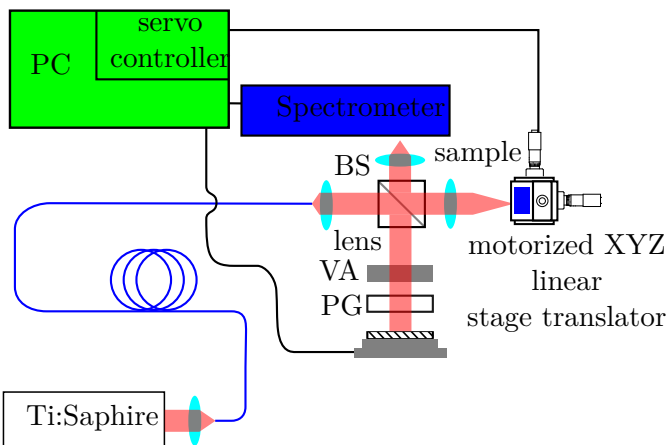


Figure 2.4.1: First spectral radar setup.

Figure 2.4.1 shows the setup schematics of the first version of SROCT. A titanium:sapphire mode-locked optical oscillator, operating at 800 nm with a spectral width of 10 nm and emitting pulses of 150 fs, was used as the initial system light source. The laser beam was coupled into 2.2 m of a monomode fiber (FS-SN-4224, Thorlabs), leading to a spectral broadening, due to dispersive self-phase modulation⁴. The initial 10 nm spectral width and 500 mW of power was broadened to 50 nm. Apart from fiber optics for spectral broadening, the setup was built in free space. On the reference arm, the beam passes through a variable attenuator (VA1), a piece

²Götzinger et al., “High speed full range complex spectral domain optical coherence tomography”.

³Leitgeb et al., “Phase-shifting algorithm to achieve high-speed long-depth-range probing by frequency-domain optical coherence tomography”.

⁴Hsu et al., “Optical coherence tomography using nonlinear optics in fiber for broadband source generation”.

of glass for dispersion compensation, and is reflected on a mirror fixed to a piezo buzzer as a translator. In the probe arm, the beam passes through an achromatic lens which focuses the beam onto the sample which is supported by a computer controlled XYZ translation stage. The combined light from the sample and reference arms are then focused to a spectrometer (USB2000, OceanOptics), which measures the light spectrum and sends it to a PC through USB port.

An axial resolution of $6 \mu\text{m}$ was achieved where the theoretical value was $5.6 \mu\text{m}$. With 2 mW of optical power incident on the sample, a system sensibility of $98 \pm 5 \text{ dB}$ was measured, following the procedure by Leitgeb⁵. The data acquisition and image generation were controlled by a LabView supported software. The quadrature delayed spectrum2.3 technique was used to eliminate mirror image and DC components, where a piezo was used to add the quadrature phase shift.

This setup was used in the study of crack propagation in fiber reinforced polymers accounted in section 3.1.

2.5 Second spectral radar implementation

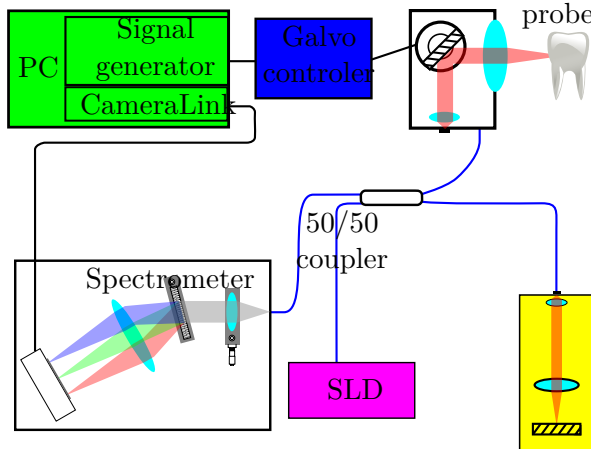


Figure 2.5.1: Spectral radar setup.

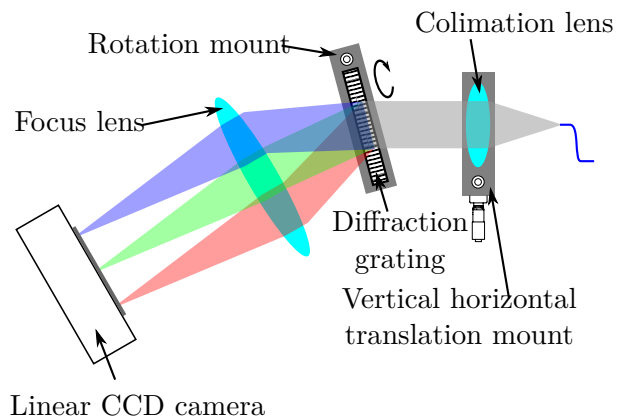


Figure 2.5.2: Spectrometer schematics.

The schematic setup of the second version of SROCT is shown in figure 2.5.1. The broadband source is a superluminescent diode Broadband SLD Light source (S840, SUPERLUM) with central wavelength 850 nm and delivering up to 25 mW and with a 49.9-nm bandwidth, which gives an axial resolution of $6 \mu\text{m}$. After traveling through the all-fiber beam splitter, the reflected beams from the sample and mirror are recombined and sent through a purpose-designed

⁵Leitgeb, Hitzenberger, and Fercher, “Performance of fourier domain vs. time domain optical coherence tomography”.

spectrometer, subsection 2.5.1. The maximum incident power on the sample was 5 mW. The output is sent to a personal computer with a LabView-based imaging program.

2.5.1 Spectrometer

In FDOCT a spectrometer with high acquisition rate (tens of thousand spectrums/second) and high resolution (<100 pm) is necessary. Due to these restrictive features there was no such device commercially available, leading us to develop our own spectrometer, schematics in figure 2.5.2. For high acquisition rate, a linear CCD camera (SM2-CL-2014, Atmel) was used. This camera features a line reading rate of 10k lines/s, with each line containing 2048 pixels with bit depth of 12 bits. The amount of data generated by such configuration is 60 MB/s, which is not easily handled by most computer-device communication interfaces. This camera transferred data to the computer through a CameraLink interface. The diffraction grating used was a 1200 lines/mm volume phase holographic transmission grating (Wasatch Photonics), capable to diffract >0.6 of the incident light to the first order diffraction, enabling us to construct highly sensitive spectrometer. A resolution of 100 pm was achieved.

2.5.2 Testing

To test the setup, OCT images were obtained from slices of a tooth. Figures 2.5.3(a), 2.5.3(c), 2.5.3(e) and 2.5.3(g) represent OCT images of different samples restored in composite resin, and 2.5.3(b), 2.5.3(d), 2.5.3(f) and 2.5.3(h), their respective optical microscopy images. In figures 2.5.3(a) and 2.5.3(b) we can see an example of a well placed and sound restoration, whilst 2.5.3(c)/2.5.3(d) and 2.5.3(e)/2.5.3(f) show the presence of an air bubble (within the circle) close to the tooth restoration interface, as well as the dentin-enamel junction. The white appearance of the air bubbles in the optical microscopy images is due to the smear layer impregnation during the teeth sectioning with diamond wheel. Figures 2.5.3(g) and 2.5.3(h) show an aesthetic facet, in which it is possible to observe the tooth-restoration limits (arrows), the dentin-enamel junction and, specially, the use of different shades of composite resin (large rectangles).

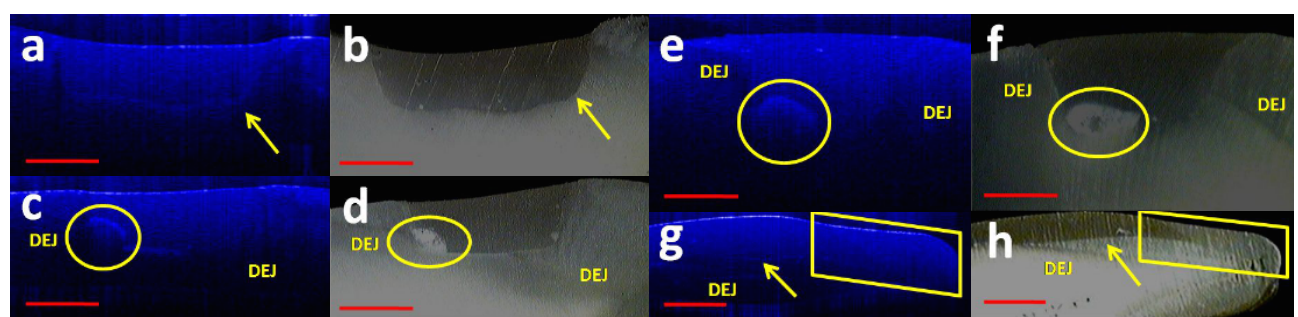


Figure 2.5.3: Images of transversal section of teeth. (a),(c),(e) and (g) are OCT images. (b),(d),(f) and (h) are are micrographs of the respective OCT images

Chapter 3

Applications in Optical Coherence Tomography

Several essays were made using the two OCT system previously described. Not being an exhaustive list we show here three applications made using those systems. The research effort were all published and were done mainly by Deborah Fonsêca¹, Cláudia Mota and Ana Karla Braz². Most of the time the OCT systems were stable and easy to use, no direct assistance from my person was needed.

3.1 Fiber reinforced composite analyses

We used an OCT system to image the sites of fracture initiation and slow crack propagation in a fiber reinforced composite. Bar specimens ($2 \times 3 \times 25$ mm) of fiber reinforced composite were mechanically and thermally cycled to emulate oral conditions. The interior of the samples were analyzed prior and after the emulations. We analyzed the specimens that were intact after the loading cycling. The results demonstrated the capacity of the OCT technique to generate images of the site fracture initiation, crack propagation, and regions surrounding the fracture, and that it can be used in the future for quantitative analysis, thus complementing other existing methods, with the main advantage of being non-destructive and non-invasive.

3.1.1 Motivation

In the oral cavity, prosthetic reconstructions usually suffer from variable temperature and load conditions. Such thermal and loading cycling may cause fractures during long-term clinical

¹Fonsêca et al., “In vitro imaging of remaining dentin and pulp chamber by optical coherence tomography: comparison between 850 and 1280 nm”.

²Braz et al., “Evaluation of crack propagation in dental composites by optical coherence tomography”.

use³. Fatigue fracture after years in clinical use was found to be a common failure reason. The longevity of restorations is dependent upon many factors, including operator skill, the materials and techniques used, the criteria for replacement, patient compliance with oral hygiene advice, the oral environment and its contribution to the patient's susceptibility to caries. Relatively few studies have investigated these factors⁴. Fatigue in dental restoratives is also influenced by corrosive water attack at a certain temperature (37°) and by cycling masticatory forces. The naturally occurring loading of a filling was estimated⁵ at between 5 and 20 MPa. Contemporary approaches to fatigue principles consider a fracture process in three phases: crack initiation, slow crack growth, and fast fracture. The latter phase is very short in duration and thus the time of crack initiation and of slow crack growth account for the useful fatigue resistance of a material. Crack initiation nucleates at heterogeneities like surface and subsurface microcracks, porosities, filler particles, crazes, etc. within the materials.

Cycling loading is able to drive a crack, called slow crack growth. Additional water exposure causes a variety of weakening effects on resin composites: degradation of the filler-matrix interface, elation, and swelling or a viscoelastic effect on the matrix which all accelerate slow crack growth⁶.

To assess the possibility of fracture initiation and crack evolution analysis, sample bars of dimensions 2 × 3 × 25 mm were prepared. Using a split mold, 1 mm layer of particulate filler CR (Suprafil 3M/ESPE) was placed into the split mold, then a dental fiber DF (Interlig, Angelus) was placed. Another layer of CR was applied immediately after polymerization of DF on the top of the fiber reinforced composite (FRC) substructure, leaving the thickness of the specimen at 2.00 mm. The light polymerization was performed with a halogen light. figure 3.1.1.a shows a photograph of a section of the FRC where we can see the fiber. The OCT image, figure 3.1.1.b, confirms the ability to see the substructure of the composite. Because of the refractive index of the resin, the vertical dimensions inside sample needs to be corrected by a factor of 1.5.

Before the load test, all the specimens were thermally cycled in 1000 cycles between 5 and 55 °C. The thermal cycling consisted of a 5 s transfer between temperature baths. From the OCT images, no difference in the samples were detected by analyzing the images before and after the thermal cycles⁷.

For the mechanical cycling, the specimens were tested in three point loading, depicted in figure

³Lassila et al., "Flexural properties of fiber reinforced root canal posts"; Rantala et al., "Fatigue resistance of removable orthodontic appliance reinforced with glass fibre weave".

⁴Burke et al., "Influence of patient factors on age of restorations at failure and reasons for their placement and replacement".

⁵Braem, Lambrechts, and Vanherle, "Clinical relevance of laboratory fatigue studies".

⁶Söderholm and Roberts, "Influence of water exposure on the tensile strength of composites".

⁷Kyotoku et al., "Fiber-reinforced composite analysis using optical coherence tomography after mechanical and thermal cycling".

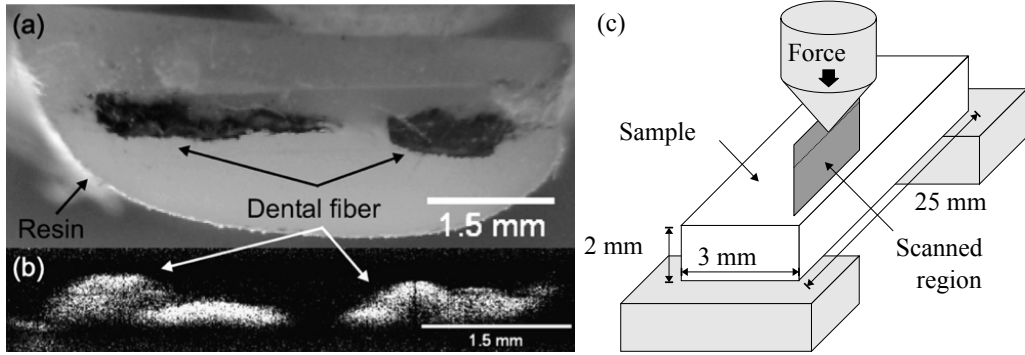


Figure 3.1.1: (a) Photograph of a section of the FRC where we can see the dental fiber. (b) OCT image confirms the ability to see the substructure of the composite, resin boundary is not shown. Because of the refractive index of the resin the vertical dimensions inside sample need to be corrected by a factor of 1.5. (c) Three point loading schematics with scanned region indicated.

3.1.1.c, in a universal testing machine (Kratos Equipamentos Industriais LTDA, SP, Brazil). The load was applied to standard bar specimens with a loading angle of 90° , a crosshead speed of 3.0 mm/min and the distance between the two supports was 8 mm. Cyclic loading was carried out to 100 cycles or until the specimens failed. figure 3.1.2 a and b show the OCT images of the sample, for a particular cycling load of 60 N. The images were taken as schematized in figure 3.1.1. Scanning was not straightforward because the cycling cracked the resin surface leaving particles that scattered the light obfuscating the region below the point of contact and often saturating the detector.

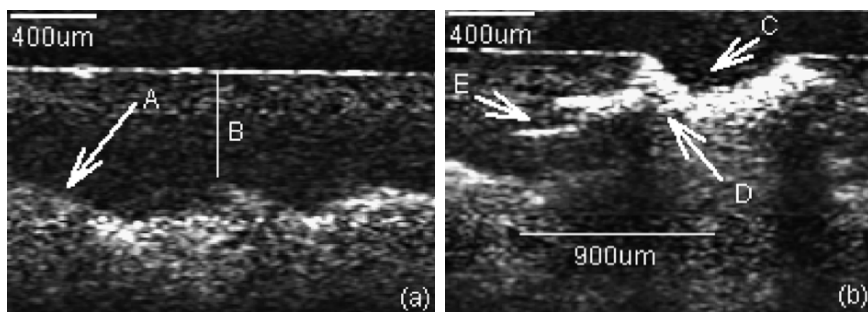


Figure 3.1.2: Slow crack growth (a) image is prior the cycling and (b) image after the cycling of 60 N load. (A) Dental fiber. (B) Distance from the surface of the beam to the top of the dental fiber. (C) Flaw initiation site. (D) Splinter region. (E) Hackle region.

There are three characteristics regions surrounding the fracture origin on the fracture surface of brittle material. The first region is generally a relatively smooth (mirror) region, the second is a slightly stippled (mist) region and the third is a very coarse (hackle) region. This last region leads to macroscopic crack branching that is, the bifurcation of the main crack. The formation

of these three regions occurs at a constant characteristic stress intensity factor⁸.

In figure 3.1.2.a, it is shown the OCT image prior the cycling. A indicates the image of dental fiber and B shows the distance from the surface of beam to the top of dental fiber (about 400 μm). On the right hand side, figure 3.1.2.b, shows the results after cycling. We can note the extension of propagation about 900 μm from the flow initiation site to the end of hackle region. This result demonstrates the possibility to study how crack initiates and propagates inside the dental material. It should be pointed out that, at 40 N load (not shown) the crack starts to form, but the resin is still intact. At 80 N load, the sample was fractured.

3.1.2 Conclusions

In conclusion, we have used the SDOCT technique to generate images of a FRC embedded in a composite resin. The results demonstrated the capacity of the OCT technique to generate images of the sites fracture initiation, crack propagation, and, regions surrounding the fracture. It is known that the penetration depth in real tooth can cover the whole enamel extension⁹ and therefore imaging fiber to a 2 mm depth is feasible in real life.

Since fracture is a major reason for clinical failure of dental restoration, and is generally preceded by slow crack propagation, the method shown here can be used for analysis of in-service failure of dental materials and, although it was only qualitatively analyzed here, it can be used in the future for quantitative analysis thus complementing other methods¹⁰.

3.2 *In vitro* Imaging of remaining dentin and pulp chamber by optical coherence tomography: comparison between 850 and 1280 nm

Citotoxicity of the dental material, deep cavity preparation, and accidental exposition of pulp tissue are factors that can be involved with the pulp irritation. The OCT is a new modality of image capable to diagnose the complex dentin pulp and to produce images through the dentin substratum, being able to measure with precision the distance between the endings of the cavity to pulp chamber. OCT provided images into reminiscent dentinal to pulp cavity of about 1000 μm (1280 nm) and 600 μm (850 nm) in depth.

Before any restoring procedure, care must be taken to properly evaluate and protect the dentin and the pulp against physical, chemical, and bacterial aggressions. The protection strategies

⁸Mecholsky, “Fractography: determining the sites of fracture initiation”.

⁹Melo et al., “Evaluation of enamel dental restoration interface by optical coherence tomography”.

¹⁰Loughran, Versluis, and Douglas, “Evaluation of sub-critical fatigue crack propagation in a restorative composite”.

depend basically on the depth of the cavity, the age of the patient, the remaining dentin thickness, and the indicated restoring material. The depth is determined by the remaining dentin thickness between cavity floor and the pulp chamber's ceiling. The remaining dentin thickness of 500 µm should be enough to protect the pulp tissue against the cytotoxic effects of dental materials¹¹, and the remaining dentin thickness of 300 µm may provoke a persistent inflammatory pulpal response.

The OCT is a potential image technique that may contribute to prevent accidental pulp exposures in clinical practice and help pulp protection, by quantitatively determining the remaining dentin, thus helping to make the excavation procedures more predictable and safe.

During excavation procedures and cavity and crown preparation, the pulp may be accidentally exposed. Knowledge of the configuration of the pulpal space and the pulp-dentin complex morphology plays an important role to prevent iatrogenic or so-called accidental exposure of the pulp. It is often difficult in clinical practice and with conventional image techniques, such as X-ray, to identify the exact dimensions of the internal tooth anatomy¹².

To detect the depth of the dental cavity in relation to the pulpar chamber, the professionals withhold information collected through the clinical examination—visual and tactile inspection—and of the radiographic examination. These methods are subjective, which may lead to the wrong choice for the ideal treatment. Moreover, the radiographic procedure possesses some limitations for presenting overlapping of anatomical structures, for being a static method and emitting ionizing radiation.

More recently, besides evaluation of enamel interface restoration¹³, also early caries diagnostics¹⁴ and the analysis of the performance of the dental materials¹⁵ have been studied and reported by our group. In 2006, Kauffman et al. performed the first OCT image of dental pulps using rat's teeth¹⁶.

This work reports the first research comparing images obtained by OCT of the complex dentin-pulp of in vitro human teeth, using two different wavelengths in the near infrared, and also using a conical beam tomography as the gold standard. The results are compared, and the conclusion that OCT at 1280 nm performs better than at 850 nm is obtained, besides corroborating the feasibility of OCT for potential clinical use to prevent accidental exposure of the pulp and to promote preventive restoration treatment.

¹¹Hanks et al., "Cytotoxicity of dental composites and other materials in a new in vitro device".

¹²Mjör, *Pulp-dentin biology in restorative dentistry*.

¹³Melo et al., "Evaluation of enamel dental restoration interface by optical coherence tomography".

¹⁴Freitas et al., "Imaging carious human dental tissue with optical coherence tomography".

¹⁵Braz et al., "Evaluation of crack propagation in dental composites by optical coherence tomography"; Kyotoku et al., "Fiber-reinforced composite analysis using optical coherence tomography after mechanical and thermal cycling".

¹⁶Kauffman et al., "Characterization of the dental pulp using optical coherence tomography".

3.2.1 Materials and methods

The experimental study was carried out in accordance with the ethical guidelines in research with human participants by Center of Health Sciences, Universidade Federal de Pernambuco, Brazil.

Higid molar teeth from humans were used in this research. The occlusal surfaces of the teeth were prepared with a perpendicular carbide bur along the axis of the teeth producing a plane on that surface, which were subsequently polished manually with a 400, 600, and 1200 sand-paper sheet. Wear was performed perpendicular to the long axis of teeth and lasted until the occurrence of minimal cavity pulpal exposure creating a plane on occlusal surface. The wear stopped until the occurrence of minimal cavity pulpal exposure. In practice, polishing or surface preparation is not required to obtain the images.

The images of the remaining dentin thickness and pulp chamber were taken by scanning the occlusal surface in a vestibule-lingual direction. The laser penetrated into the teeth structure and a tomographic image of the frame, parallel to the axis of teeth was obtained.

After the image construction by OCT 1280 and 850 nm, the teeth were tomographically analyzed using the i-CAT cone beam volumetric tomography (CBVT) imaging system Imaging Sciences International, LLC, Pennsylvania, which radiates from an X-ray source in a cone shape, encompassing a large volume with a single rotation about the sample. This tomography system is a technology used to analyze both double jaw anatomies in patients by dentistry when more accuracy is required on complementary exams. The CBVT produces volume imaging in an easier and faster way than conventional medical computed tomography¹⁷. The scan offers times at 10, 20, and 40 s, with standard reconstruction taking <30 s, providing dentists with near-instant data for the best possible patient diagnosis, treatment, and surgical predictability. The pictures obtained are then reconstructed using algorithms to produce three-dimensional images at high resolution. Using the i-CAT software, it was possible to generate sliced 2-D images with thickness of 0.12 mm limited by the instrument resolution, eliminating the problem of superposition, and these images were then compared to the OCT images.

3.2.2 Results

For comparison purposes, we first show in figures 3.2.1.a and 3.2.1.b images by i-CAT CBVT of the pulp chamber region studied. The white area is the dentin (D), whereas the pulp chamber (PC) region is the dark area inside. The square region marked is the zoom region shown in figure 3.2.1.b. The dimensions in figures 3.2.1.a and 3.2.1.b are shown by the scales. figure 3.2.1 shows a remaining dentin thickness of $\sim 120 \mu\text{m}$, which was thick enough to avoid pulpar exposition.

¹⁷Danforth, “Cone beam volume tomography: a new digital imaging option for dentistry”.

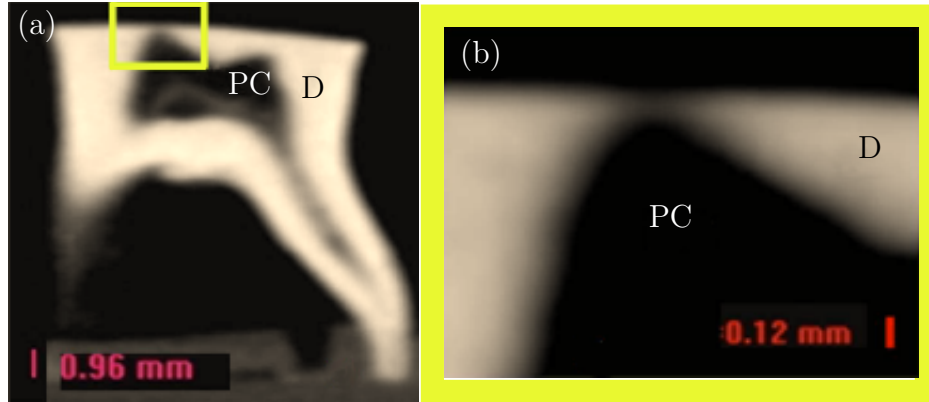


Figure 3.2.1: i-CAT cone beam volumetric tomography image of the dentin and pulp chamber studied: (a) 0.12 mm slice longitudinal of the tooth and (b) zoom 400% at the dentin-pulp interface.

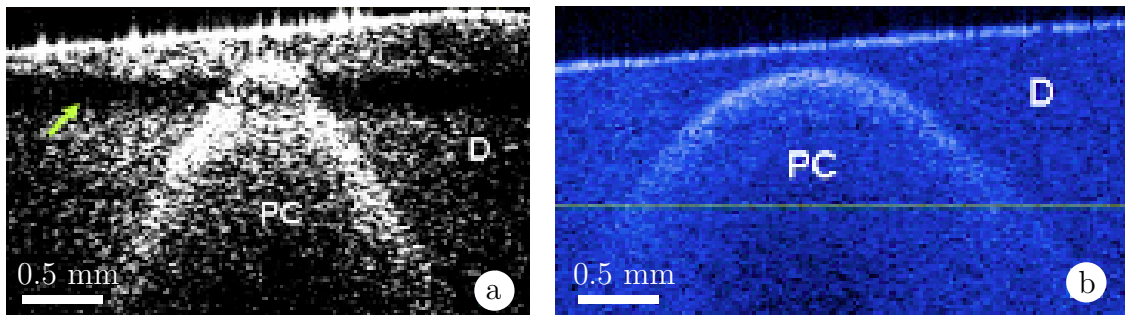


Figure 3.2.2: OCT images of the Dentin (D) and pulp chamber (PC) corresponding to the i-CAT CBVT image of fig. 3.2.1.b: (a) OCT at 1280 nm and (b) OCT at 850 nm. The black transversal region in (a) is an artifact (indicated by the arrow).

The OCT images at the wavelengths of 1280 and 850 nm for the zoomed-in region shown in the i-CAT CBVT image of figure 3.2.1.b are seen in figures 3.2.2.a and 3.2.2.b, respectively, which also show the structural components of the pulp-dentin complex. The structures in the OCT images are distinguished due to the different gray levels (or blue levels, in the case of the 850 nm system), where the contour of the chamber to pulp appears whiter (highest scattered intensities) and the dentin with the darker level (lowest scattered intensity). Those structures are clearly delineated due to influence of the structure of the biological components with distinct refractive indices, which backscatters light in very different ways. No pulp exposition is observed, as confirmed by the i-CAT CBVT, and comparing figures 3.2.1.b, 3.2.2.a, and 3.2.2.b, it clearly demonstrates the capacity of quantitative measurement by the OCT with remaining dentin thickness measured as $\sim 120 \mu\text{m}$. Note that the depth dimension in the OCT must be divided by the refraction index of dentin $\sim 1.5^{18}$. The black transversal region, indicated by the arrow in figure 3.2.2.a, is an artifact.

¹⁸Colston et al., “Imaging of hard-and soft-tissue structure in the oral cavity by optical coherence tomography”.

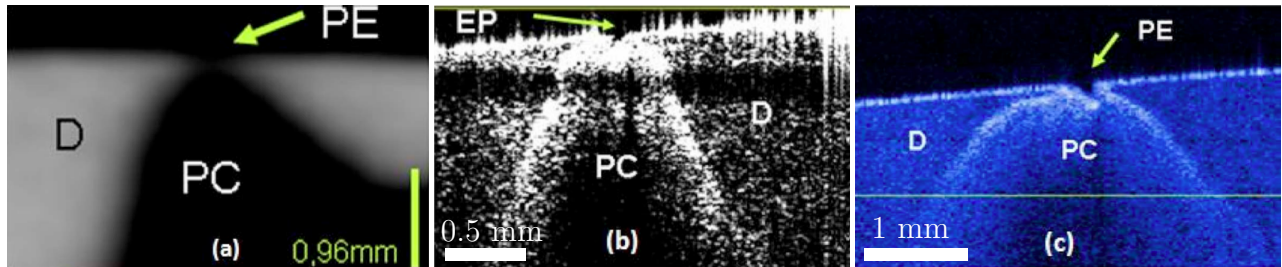


Figure 3.2.3: Dentin (D), pulp chamber (PC), and site of the pulpal exposure (PE). Image of the pulp-dentin complex acquired with (a) i-CAT CBVT , (b) OCT 1280 nm image (c) OCT 850 nm image.

Figure 3.2.3 shows an image where the exposition of the pulp cavity is clearly seen. Figure 3.2.3.a is the i-CAT CBVT image section, figure 3.2.3.b the OCT at 1280 nm, and figure 4(c) the OCT at 850 nm. Once again, D and PC are clearly delineated in the OCT image. The pulp exposition site (PE) is seen as a discontinuity at the dentin surface, which is the homogeneous white line of high intensity. The OCT images shown allow the direct measurement of the observed region depth.

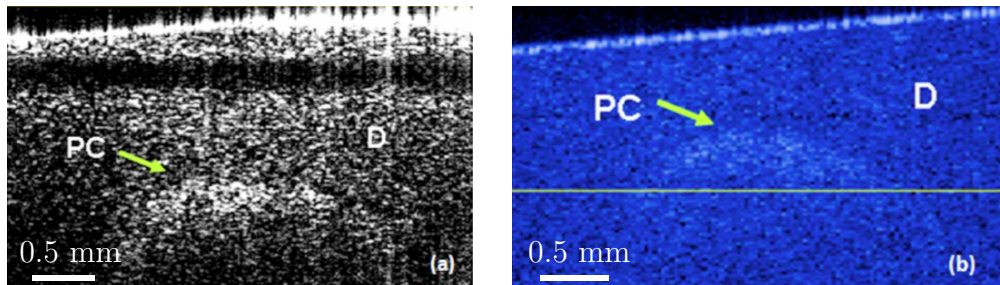


Figure 3.2.4: Image of the deeper pulp ceiling visualized by the OCT. (PC) beginning of the contour of the pulpar ceiling, (D) dentin: (a) 1000 μm visible depth of the pulp cavity at 1280 nm. The black transversal region is an artifact (b) 600 μm visible depth of the pulp cavity at 850 nm.

In order to verify the maximum depth that could be achieved for each OCT system, we carried out a series of measurements whereby the studied dentin region was being reduced by polishing until the pulp could be identified. The scale shown in figures 3.2.4.a and 3.2.4.b clearly demonstrate the capacity of quantitative assessment of the OCT, as well as the maximum penetration depth of the radiation inside of the dentin region. Comparing the measurements of the deeper ceiling of the pulp chamber visualized at the two different wavelengths 1280 and 850 nm, respectively, the remaining measured dentin thickness was $\sim 1000 \mu\text{m}$ at 1280 nm and $600 \mu\text{m}$ at 850 nm system. These values had already been corrected for the dentin refractive index $\sim 1.5^{19}$.

¹⁹Ibid.

The deeper penetration depth of the light at 1280 nm compared to 850 nm is due to a reduction of absorption and scattering coefficients of the dentin at 1280 nm²⁰.

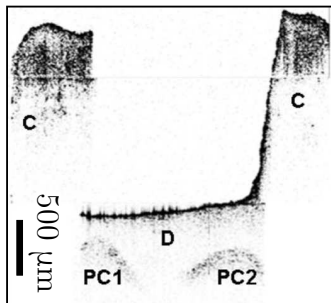


Figure 3.2.5: OCT image composition showing the dentin (D) and pulp chamber (PC1 and PC2) with wavelength of 1280 nm. Notice the thin layer of remaining dentin about 260 μm to PC1 and 600 μm to PC2.

As a final example, figure 3.2.5 shows a composition of three different images from OCT at 1280 nm, taken at the same sample, showing the view of the longitudinal slice detecting cusps (C), D, and the vestibular and palatine pulp horn, where it is possible to identify a remaining thin layer of dentin of roughly 260 and 600 μm (PC1 and PC2) between the cavity floor and pulp chamber. This is another clear demonstration of the potential of OCT for pulp chamber assessment.

3.2.3 Conclusion

The OCT clearly demonstrate the capacity of quantitative assessment and penetration of the radiation on the pulp chamber and the remaining dentin, compared to the scan in i-CAT CBVT. In accordance with the results presented for the OCTs with a wavelength of 1280 and 850 nm, the two techniques presented effectiveness. Furthermore, our experiment corroborated the depth of penetration almost two times bigger for 1280 nm OCT. OCT is a non-invasive and non-destructive technique; as a consequence, it possesses great potential for use routinely in clinical practice for the diagnosis of the complex dentin pulp, preventing accidental exposure of the pulp and promoting preventive restoration treatment. For practical use, a hand piece or an appropriate head for the imaging acquisition is required, which is a technologically solvable issue.

²⁰Drexler, “Ultrahigh-resolution optical coherence tomography”.

3.3 Clinical use of optical coherence tomography to evaluate the integrity of dental restorations

We have applied Optical Coherence Tomography (OCT) clinically to assess dental restorations in humans. Twenty patients with resin composite restorations in anterior teeth were selected and evaluated using a conventional radiographic examination, visual inspection and OCT. Images were obtained using a home built OCT system operating in the spectral domain, with an 850 nm superluminescent diode light source. The results were analyzed with respect to the integrity and marginal adaptation of the restoration. Using appropriate software failed and failing restorations, including those with lesioned regions, could be located prior to the placement of a new restoration. Lesions and failed restorations were identified with the OCT system that could not be seen by conventional visual and X-ray examinations and these were found to be present on surgical intervention. This *in vivo* study demonstrates that the OCT technique has a great potential to be used in clinical practice to assess dental restorations and prevent recurrent caries.

3.3.1 Introduction

Dental restorations provide a barrier restricting oral fluids and bacteria from entering the tooth after the removal of any damaged or missing tissue. An inadequate marginal seal can result in gap formation that leads to microleakage, which may be responsible for marginal breakdown, recurrent caries, increased post-operative sensitivity, pulpal inflammation, and staining²¹.

The success of the restorative treatment depends on the integrity of the tooth-restoration interface and this particular region is the subject of much research and discussion in the dental community. Clinically, the most common tools for detection of restorative failures are by tactile, visual inspection or radiographic examination. However, since initial microleakages can be clinically and radiographically imperceptible, secondary caries may currently progress before the problem can be detected by the dental practitioner.

Here we present an *in vivo* study to detect failures at the enamel-dental restoration interface, and the integrity of superficial and internal structures of restorations in a clinical setting using OCT. This study was undertaken with 20 patients attending the Dentistry College of the Universidade Federal de Pernambuco. The relatively large number of attending patients allowed us to obtain and analyze the results in a very consistent manner. Results were compared to conventional radiographs and clinical examination, represented here by photographs.

²¹Attar et al., “Microleakage of class V cavities with different adhesive systems prepared by a diamond instrument and different parameters of Er:YAG laser irradiation”.

3.3.2 Material and methods

This study was developed according to the guidelines given by Ethical Committee in Human Research of the Universidade Federal de Pernambuco, Brazil. Twenty patients with resin composite restorations in upper anterior teeth were selected. These patients were between 18 and 45 years old, both male and female, and had their restorations performed between 1999 and 2009. All the restorations had a superficial satisfactory clinical aspect with no obvious aesthetic failures such as staining, undesirable shape or obvious missing material.

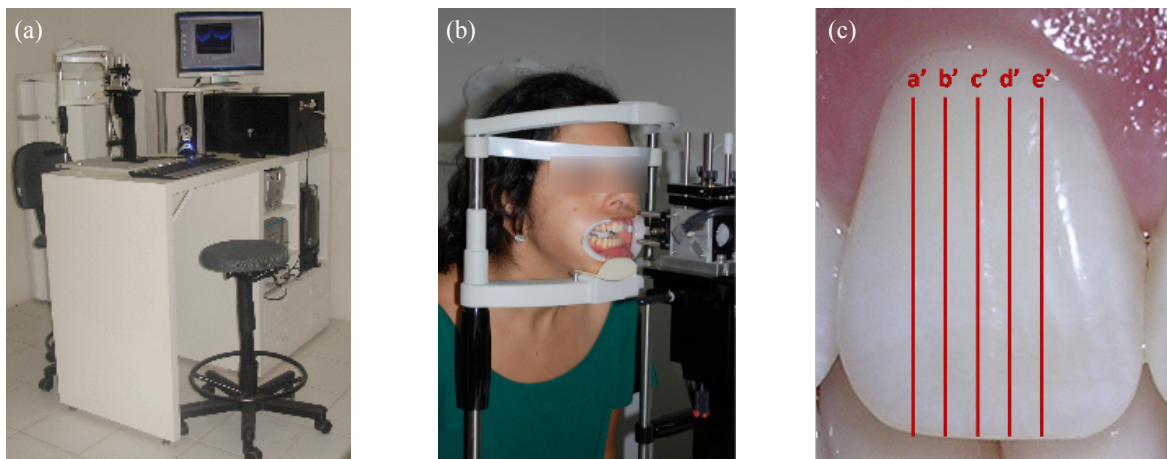


Figure 3.3.1: (a) SDOCT adapted for clinical essays; (b) Positioning the patient; (c) Sequence indicating the scan positioning in the patient's teeth. identifying the tomographic slices.

To perform the OCT examination, a lip retractor was used on the patients, and their heads were positioned in an appropriate support, in front of the sample arm, seen in figures 3.3.1.a and 3.3.1.b. The image acquisition time is less than one second (for each image, there was 0.1 second of pre-scan settling time and 80 μ s of integration time) but even so the support was used to minimize movement which would otherwise blur the high optical resolution images. We analyzed the results with respect to the integrity and marginal adaptation of the restoration by visual inspection of the images in real time as well as on the images produced from the subsequent image processing.

As comparison criteria to OCT, we employed the diagnostic methods most widely used in dentistry: a clinical examination composed of visual and/or tactile inspection (shown in this paper by photographs) and a conventional X-ray. The dental X-Ray equipment used was the Spectro 70X (Dabi Atlante), operating at 70 kVp head power and a head current of 8 mA. The radiographic film used was Kodak Dental Intraoral E-Speed Film (Carestream Health), and the dental developer and fixer, was from the same manufacturer.

During a clinical examination, it is possible to detect changes in resin composite color, polishing failures, contact point problems and major gaps and fissures; radiographic images can show

excess or lack of restorative material, large areas of demineralization (typically greater than 30% of mineral loss), and gaps or fractures points larger than the minimum detection size observed by OCT.

To evaluate the presence, or otherwise, of failures in the restorations, three experienced professionals, all of them Restorative Dentistry professors, were trained to interpret OCT images. Each professor was then individually shown the clinical photograph of each restoration in question, and requested to complete a form describing what they could see in that patient's image in terms of the restoration extension, and if there was any form of failure. In case of detected failure they were then asked to classify the failure. Then, the radiographic images were shown, in the same way and, last, the OCT images. To analyze the data a Kappa coefficient test was applied. Kappa coefficient is a statistical measure of the agreement for qualitative/categorical items; its aim is not to compare the diagnostic potential between the three techniques employed, but to compare how the evaluators agree among themselves in each form of diagnostic technique separately. After the analysis all of the patients that presented failures in their restorations were recalled to the clinic and had new procedures performed after a discussion with the patient following the approved clinical procedure.

3.3.3 Results

Table 3.1 indicates a comparison between all the methods used in this work for the first three cases.

Patient #	Visual inspection defect	X-Ray defect	exam	OCT defect	Comment
1	No	No		No	A well placed and sound restoration
2	No	No		Yes	From visual inspection, it is only possible to observe that the restoration is not polished
3	No	Yes		Yes	X-ray exam only shows the excess of restorative material, but is not able to visualize the failures seen by OCT

Table 3.1: A summary of the preliminary results.

Figure 3.3.2 shows a sequence of examinations of a patient with a well placed and sound restoration in a central incisor, placed seven years before. Figure 3.3.2.a represents the clinical examination; 3.3.2.b, the conventional radiograph showing the restoration at the incisal region in the circle. Arrows in 3.3.2.c indicate the interface between the enamel and the restorative material, which can be clearly seen.

Figure 3.3.3.a shows a lateral incisor with an aesthetic facet (not polished) over an incisal and cervical restorations, confirmed by radiography in figure 3.3.3.b, performed two weeks before

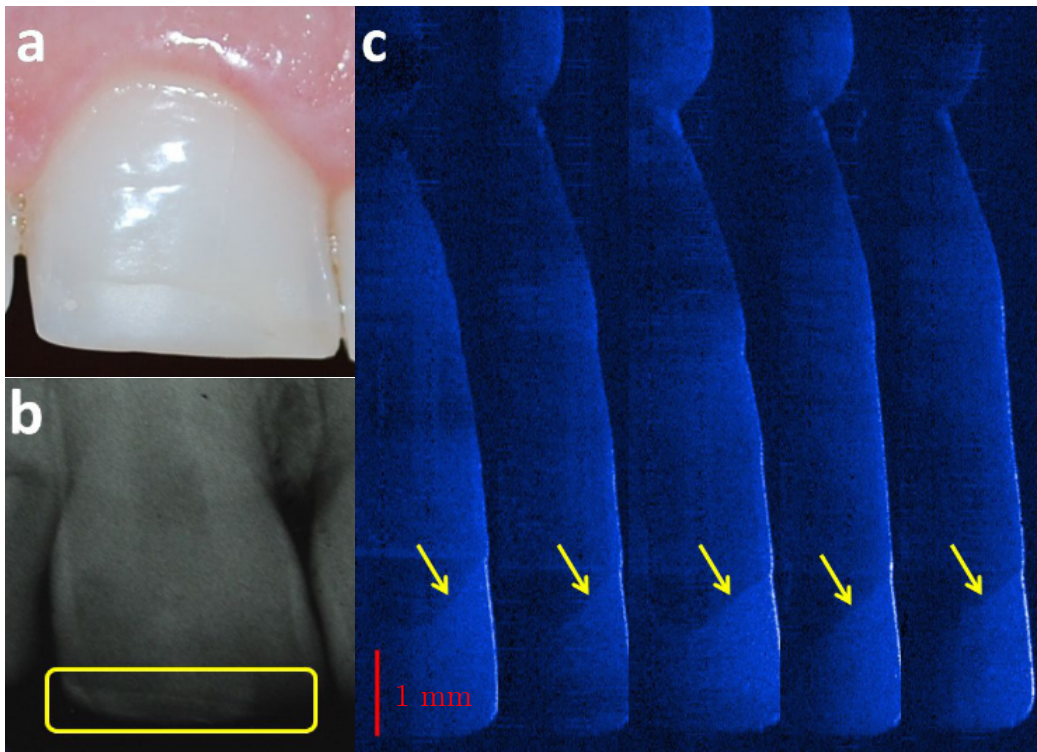


Figure 3.3.2: Well suited restoration of a central incisor. (a) clinical photograph; (b) conventional radiography; (c) sequence of OCT images: arrows indicate the integrity in the enamel-restoration interface.

the analysis reported here. In the OCT image, figure 3.3.3.b, an air bubble in the restoration (within the circle) can be seen and the dots indicate the points of microleakage at the enamel-restoration interface. The small rectangles indicate an extensive space under the restoration, probably due to resin polymerization contraction during the restorative procedure and the triangles indicate crack points between resin increments.

Restorations involving medium and incisal regions of a central incisor, performed in 2001 in another patient are shown in figure 3.3.4, where figure 3.3.4.a shows the clinical photograph with no sign of failure, and different colors between the resin composite and the dental enamel. In figure 3.3.4.b, the conventional radiograph, it is possible to observe excess restorative material at proximal surfaces; and figure 3.3.4.c shows the OCT image sequence. The arrow here indicates the well placed enamel-restoration interface. However, several undesirable features can be identified: air bubble (within the circle); evidence of a gap between the enamel and the restorative material (identified by the dots); superficial defects and internal fractures in the resin composite (identified by the triangles).

In some cases, a restoration does not necessarily need to present failures throughout its entire structure to be considered for replacement and they may well show one part which is well placed and intact whilst another area has problems. This can also be seen in figures 3.3.4.c

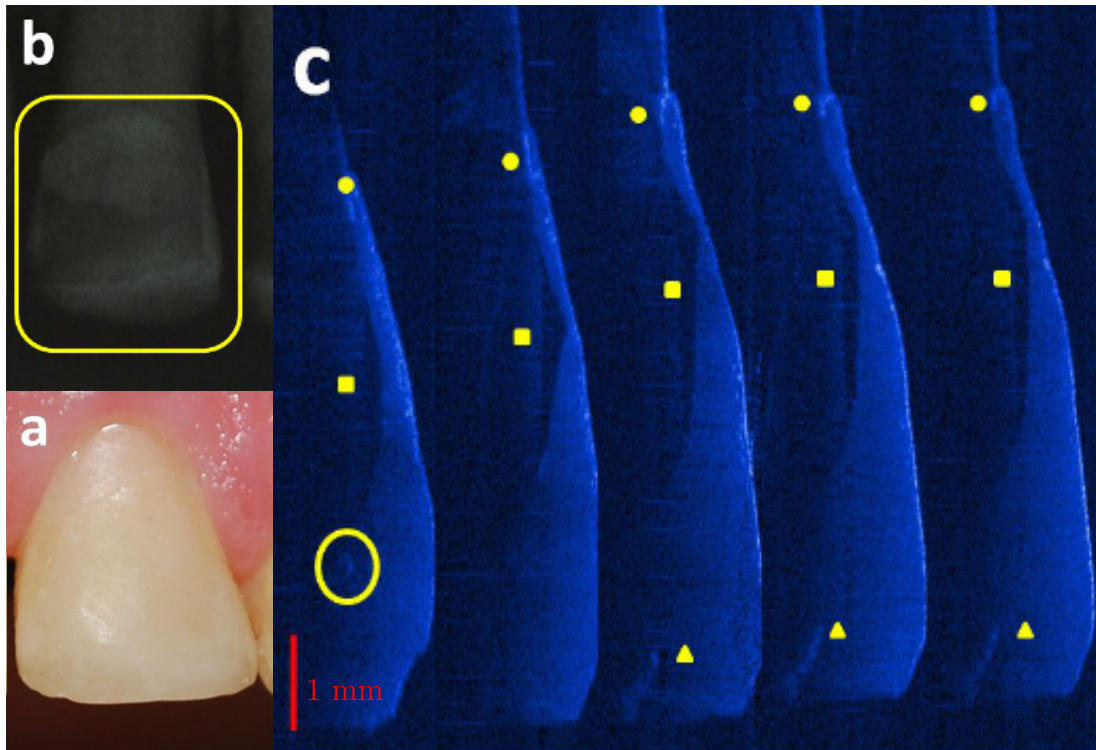


Figure 3.3.3: An aesthetic facet over an incisal restoration. (a) clinical photograph; (b) conventional radiography; (c) sequence of OCT images: air bubble (shown within the major circle); gaps at the interface enamel-restoration (indicated by the dots); small rectangles indicate an space under the restoration, probably due to polymerization

and 3.3.5. In the first slice of figure 3.3.4.c, we can see an arrow that indicates the well placed enamel-restoration interface, but in subsequent slices, we can see some failures, described previously. The same situation can be seen in figure 3.3.5, with a restoration involving medium and incisal regions. Arrows indicate the well placed enamel-restoration interface; dots indicate enamel-restoration microleakages; triangles indicate evidence of superficial fissures at the resin composite; another feature is the different pseudo color of the resin composite at the incisal region when compared to medium region, marked with the large rectangles. This can be seen by OCT because lighter colors of resin have lower refractive indices, and thus this modifies the scattering in this region. In figure 3.3.6, we can see a sequence of failures over the entire structure of an incisal restoration (dots), beside the enamel-dentin junction. Finally, in figure 3.3.7, we can observe three different aesthetic facets. In the region indicated by the diamonds, problems with the cervical adaptation of the restorations are identified in figures 3.3.7.a and 3.3.7.b, whereas a well suited adaptation is seen in figure 3.3.7.c. None of these clinically important defects, seen by OCT, could be observed in the clinical images and X-rays, even when they were subsequently examined after the detecting a problem in the OCT data sets.

Table 3.2 shows the Kappa coefficient results for each form of diagnostic examination. It can be

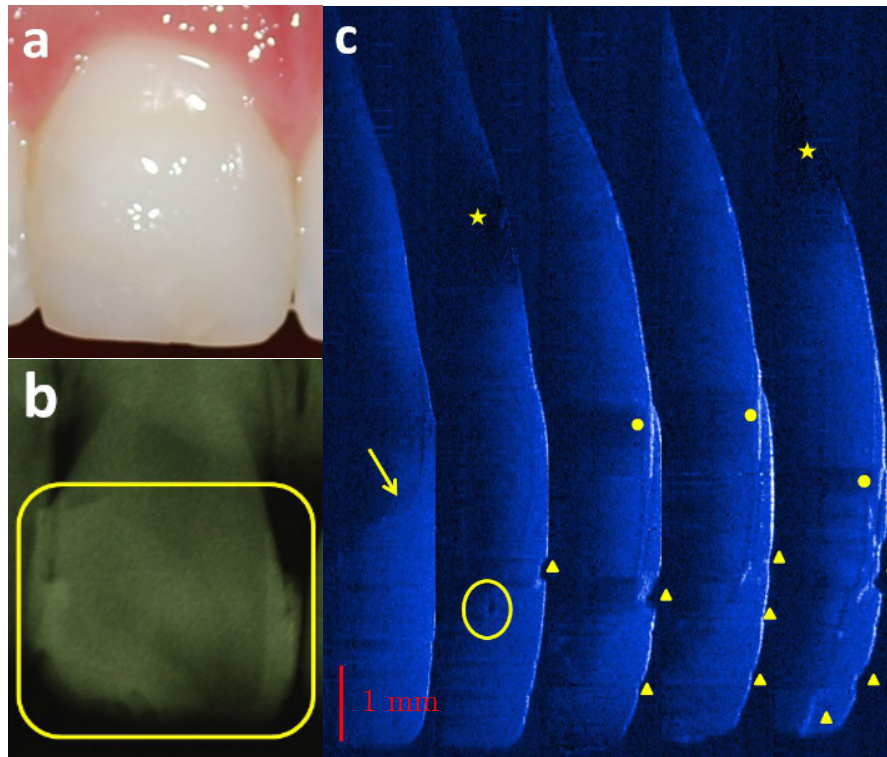


Figure 3.3.4: Restoration involving medium and incisal regions. (a) clinical photograph; (b) conventional radiography; (c) sequence of OCT images: arrow indicates the well suited enamel-restoration interface; within the circle, an air bubble; dots indicate gaps at the enamel-restoration interface; triangles shows superficial defects and internal fractures at the resin composite; stars indicate imaging artifacts.

seen that for clinical and radiographic examinations there was a substantial agreement between the evaluators, whilst for the OCT examinations the Kappa index obtained demonstrates perfect agreement: it means that the OCT images provide more accurate information to diagnostic than the clinical photographs and the X-ray exam. It was not possible to compare the kinds of failures seen in each type of examination, as the OCT is able to visualize internal structures that are impossible to be seen in the clinical inspection or radiographic examination.

	Clinical exam	Radiographic	OCT
κ	0.732	0.732	1.000
p-value	<0.001	<0.001	<0.001
κ 95% range trust	Upper	1.000	1.000
	Lower	0.374	0.642

Table 3.2: Kappa coefficient results.

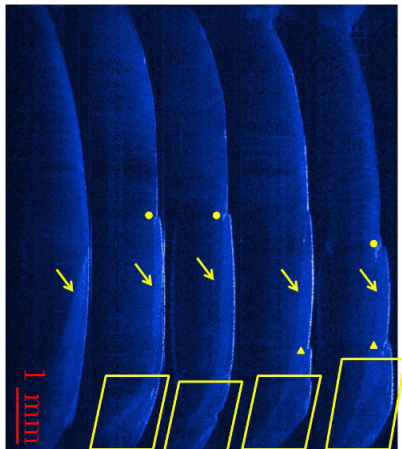


Figure 3.3.5: Restoration involving medium and incisal regions. Arrows indicate the well suited restoration with defects throughout the enamel-restoration interface; dots, the presence of entire structure. Dots indicate gaps between the restorative material and the resin composite; within the large rectangle, we can observe a darker region, corresponding to lightest resin color increment in the incisal part of the restoration.

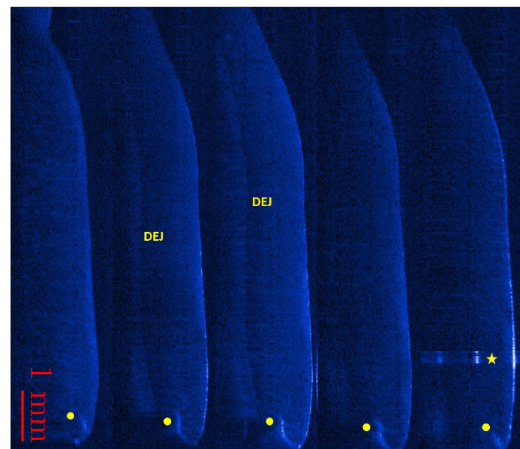


Figure 3.3.6: Sequence of an incisal edge. Dots indicate gaps between the restorative material and the dental enamel; in DEJ, we can observe the dentin-enamel junction; artifact imaging est resin color increment in the incisal part of the indicated by star.

3.3.4 Discussion

The improvements in the aesthetic and physical properties of composite resins over the past ten years have established them as the material of choice for restorations of anterior teeth when used in conjunction with the acid-etch technique and dental bonding systems²². However, their high aesthetic quality frequently makes it harder to see early signs of failure and due to the way that these materials behave, compared to traditional amalgam and gold restorations, early failure is more likely. Failures at the tooth-restoration interface can be associated with several factors including incorrect restorative technique, the physical properties of the materials used and, especially, the contraction of the material generated during the polymerization of the restorative material.

An adequate marginal adaptation and the integrity of the restoration are fundamental to the success of the dental treatment: failures in the marginal surface cause microleakage and bacteria infiltration; loss of integrity can be present in the internal or superficial structure of the restoration, and reduces the quality of the restoration, leading to early fracture of the restorative treatment. Some defects seen in this study are known to cause a loss of integrity in resin based composite restorations including air bubbles in the restoration, regions without material under the restoration (voids), cracks and fissures at the resin composite and gaps. When these

²²Garoushi, Lassila, and Vallittu, “Fatigue strength of fragmented incisal edges restored with a fiber reinforced restorative material”.

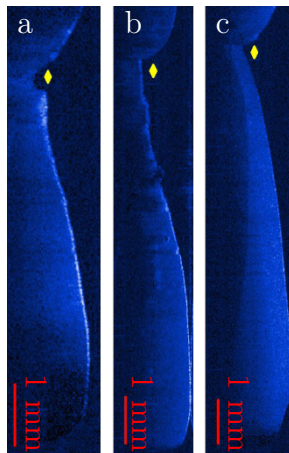


Figure 3.3.7: Three different aesthetic facets. Diamonds indicate problems with cervical adaptation of the restorations in a) and b), and a well suited adaptation in c).

kinds of failures are present and the restorative procedure is not adequate, a new treatment should be discussed with the patient.

The current methods clinically used to diagnosis are not able to visualize micrometric structures. In the radiographic examination, for example, an early enamel caries lesion is visible only after approximately 30%–40% mineral loss²³. This deficiency makes it difficult to diagnose early recurrent caries, when an earlier diagnosis means an easier and less traumatic treatment, leaving more enamel present in the tooth after treatment.

The Kappa coefficient was applied to analyze the agreement index of the diagnosis of the professionals selected for each examination modality separately, and the OCT method demonstrated perfect agreement between the evaluators, while there was a substantial agreement for the clinical and radiographic examinations. This indicates that OCT, besides being a good tool for diagnosis can be consistently interpreted by well trained dentists. However, it was not possible to use a statistical test to compare the clinical, X-ray and OCT examinations simultaneously. The first method (clinical observation) is only able to see defects at external surfaces; radiographic methods image across the tooth, but the resulting image inherently overlays the buccal and lingual 14 surfaces making it difficult to detect and determine internal problems. OCT can produce two dimensional and cross-sectional images, allowing the observer to see external and internal details, without overlap of structures, being able to accurately locate the visualized structures. Thus teeth were visualized in different forms in each type of examination, but many of the minor defects (air bubbles, for example) only can be seen by OCT. However, all defects detected by clinical and X-ray examinations were also detected using the OCT protocol.

This study demonstrates that OCT is a powerful tool for the early detection of failures on restorations, through visualization of microleakages, internal fractures, superficial cracks and

²³White and Pharoah, “Oral radiology: principles and interpretation”.

fissures, tooth demineralization under the restorative material and cervical adaptation of the restorations. Incipient lesions can be precisely located, their depth may be measured and their proximity to the dentin-enamel junction may be determined. The sensitivity of the OCT technique is sufficient such that details, including the use of different colors of resin composite used to increase the esthetic aspect of a restoration, can be identified due to the slightly different scattering properties (see figure 3.3.5).

As dentists are used to dental radiographs for diagnostic purposes, OCT imaging, which shows similar dental morphology, could be readily adopted²⁴ and, ideally, the number of conventional X-ray investigations would be reduced in order to minimize the patients exposure to ionizing radiation²⁵.

However, it is necessary to recognize some limitations of OCT: the system has a small depth penetration, (1-3 mm in teeth), which is, however, adequate for enamel and even dentin visualization. This is partly because we chose to use light at 850nm in order to increase the contrast between areas with only slightly different scattering properties. The use of longer wavelength sources (around 1300nm), with some slight loss of contrast, and hence sensitivity, may provide the best compromise between depth of imaging and sensitivity to minor alterations in structure. Furthermore, our current system does not allow to use the technique on every tooth, just incisors and canines. Thus for this first stage of our studies applying OCT *in vivo*, we only assessed anterior teeth, for two reasons: incisors and canines are the teeth that require better esthetic restorative procedures, and the unavailability of a handpiece probe, presently under development, to reach the posterior dentition.

Some difficulties were found during the data collection of this study: the major of them was to control the production of saliva and subsequent patient movement, which tended to produce image artifacts. Thus was minimized by careful explanation to the patient and the use of the stabilization bar. A further complication was to undertake the examinations in patients presenting a maxillary overjet (an orthodontic condition in which the third incisor is ahead of the cervical third in the upper incisors, and thus the teeth appear to be inclined horizontally) – this problem was solved by requesting the patient to bow their head slightly but, in a long term, the solution is in the development of a handpiece probe.

Further clinical studies covering cervical adaptation of aesthetics-facets and fixed crowns are currently underway. The high sensitivity of OCT to minor defects also opens up a further clinical question over which minor defects will progress to server complications and which may stay at the minor level. The development of such revised treatment protocols is beyond the scope of the present study but it is an area that will need to be investigated as OCT moves

²⁴Choo-Smith et al., “Shedding new light on early caries detection”.

²⁵Brandenburg, Haller, and Hauger, “Real-time *in vivo* imaging of dental tissue by means of optical coherence tomography (OCT)”.

towards a standard diagnostic instrument in clinical practice, as is the case with any new technological advance.

3.3.5 Conclusion

Compared to conventional radiography, OCT is a powerful tool for investigation of failures at the tooth-restoration interface. OCT is able to precisely visualize external and internal micro-metric structures, not perceived by clinical examination or conventional radiography, proving its superiority as a technique for early diagnosis of restoration failures and prevention of recurrent caries. However, because of the low penetration depth of OCT, conventional radiography imaging may not be totally substituted. This was a qualitative study applying OCT in dental clinics; we used conventional X-Ray, the most widely used modality of imaging for diagnostic assessment in dental clinics, and the clinical examination as the comparison for our study. We analyzed the differences between the modalities of exams mentioned above and the advantages and limitations of conventional radiography and OCT examinations. Besides other applications of the OCT technique *in vivo*, further complementary studies are under-way to determine dental composites failures in a quantitative manner, as well as their size or extent.

Chapter 4

Photonic Integrated Circuits

It is unnecessary to emphasize the importance of electronic integrated circuits in the present world, but it is worth to investigate if it is possible to create the same structure in different fields. In this investigation one can notice the two crucial feature of the success. The use of massively parallel device patterning enabled by photolithography and the search to decrease device size to its physical limits.

Three ramifications using the micro-fabrication process have come of age in the last decade: Microfluidics, micro-mechanical devices (MEM) and integrated optics. Microfluidics enables the possibility of massive chemical analysis which revolutionized genetic research, enabling operation such as DNA sequencing to be performed at a fraction of time that was done before. Integrated optics has the potential of large bandwidth data transfer and spectroscopic analysis, and possibly quantum processing.

Making use of this maturity, we started an effort for the integration of a optical coherence tomography system in a single chip. Here we report the results of such efforts.

4.1 Broad picture

The platform in which integrated photonic circuits works consists in the use of a high refractive index of refraction material surrounded by a material with lower index of refraction. This structure enables the most basic feature needed in the development of photonic integrated circuit which is to trap light in a single layer, in this case the higher refractive index dielectric, and to easily create lane where we can guide this light anywhere we want. We call this platform a slab waveguide. Light that is guided in the higher index material can be treated as a two dimensional wave, and a rigorous description to the waveguide is given in section 4.2. In this regime, knowledge of free space optics, appropriately adapted to two dimensions, can be applied to design photonic devices. Components like lenses, mirrors, concave mirrors, prisms, gratings

can be readily visualizable.

A good platform also needs a way to be manufactured. In this regard, photonic integrated circuit (PIC) are fortunate to be able to share the same platform as electronic integrated circuits, silicon-on-insulator, and therefore it can leverage all its fabrication and patterning know-how and infrastructure. Silicon has an index of refraction of 3.5 at wavelength 1500 nm together with its low index medium friend silicon dioxide, with 1.5 at 1500 nm. They make an excellent high index contrast composite that allows high light confinement and increasing circuit compactness.

Another component is the wire waveguide, where a high index of refraction material is surrounded by lower index material in two dimension. This structure transports light similar to a copper wire conducting electrons. This structure is widely used as fiber optics, and systems built on fiber optics can implemented on chip waveguides.

4.2 Slab waveguide

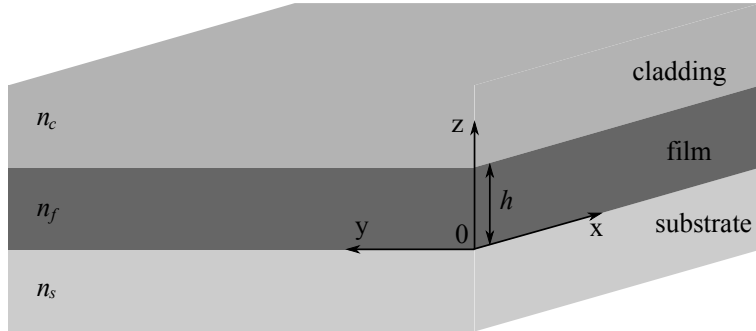


Figure 4.2.1:

We define a slab waveguide as medium comprised of an infinite film (which will be referred to as core) of thickness h and index of refraction n_f . This film is laid over a substrate with index of refraction n_s and covered with a material with index of refraction n_c . The guiding film (core) has an index of refraction greater than both the substrate and the cover, or more exactly $n_f > n_s \geq n_c$. The index of refraction field can be written as

$$n(z) = \begin{cases} n_c, & z \geq h \\ n_f, & 0 < z < h \\ n_s, & z \leq 0 \end{cases} \quad (4.2.1)$$

Over this field Maxwell's equations shown here assuming a harmonic mode with angular fre-

quency ω and magnetic permeability uniform and equal μ_0 .

$$\nabla \cdot \epsilon \mathbf{E} = 0, \quad (4.2.2a)$$

$$\nabla \cdot \mathbf{B} = 0, \quad (4.2.2b)$$

$$\nabla \times \mathbf{E} = i\omega \mathbf{B}, \quad (4.2.2c)$$

$$\nabla \times \mathbf{B} = i\omega \epsilon \mu \mathbf{E}. \quad (4.2.2d)$$

From these equation the following wave equations can be derived

$$\nabla^2 \mathbf{E} + k^2 \mathbf{E} = 0, \quad (4.2.3a)$$

$$\nabla^2 \mathbf{B} + k^2 \mathbf{B} = 0, \quad (4.2.3b)$$

where, $k = \frac{2\pi}{\lambda} = \frac{\omega}{c}$. The medium we are dealing with is symmetric by translation on the x and y axis. This allows us to have a solution in the following forms

$$\mathbf{E}(\mathbf{R}) = \Psi(\mathbf{r}) \Phi(z) \quad (4.2.4)$$

$$\mathbf{B}(\mathbf{R}) = \Psi(\mathbf{r}) \Phi(z) \quad (4.2.5)$$

where $\mathbf{r} = x\hat{i} + y\hat{j}$, $\Psi(\mathbf{r})$ is a scalar field that depends only on \mathbf{r} , and $\Phi(z)$ is a vector field that depends only on z , notice that it is $\Phi(z)$ that specifies the field polarization. Either assumption can be used. Naturally the electric and magnetic field are still connected through Maxwell equations 4.2.2c and 4.2.2d, properly rewritten below

$$\mathbf{B} = \frac{1}{i\omega} \nabla \times \mathbf{E}, \quad (4.2.6a)$$

$$\mathbf{E} = \frac{1}{i\omega \epsilon \mu} \nabla \times \mathbf{B}. \quad (4.2.6b)$$

We can break down the laplacian into an in-plane (∇_t^2) and a transversal to the plane ($\frac{\partial^2}{\partial z^2}$) component as $\nabla^2 = \nabla_t^2 + \frac{\partial^2}{\partial z^2}$, and separating variable we get

$$\frac{1}{\Phi(z)} \frac{\partial^2 \Phi(z)}{\partial z^2} + \frac{1}{\Psi(\mathbf{r})} \nabla_t^2 \Psi(\mathbf{r}) - k^2 n_i^2 = 0, \quad (4.2.7)$$

defining

$$\frac{\partial^2 \Phi(z)}{\partial z^2} - \kappa_i^2 \Phi(z) = 0 \quad (4.2.8)$$

$$\nabla_t^2 \Psi(\mathbf{r}) - \beta_i^2 \Psi(\mathbf{r}) = 0 \quad (4.2.9)$$

using this definitions on 4.2.7, we get

$$\kappa_i^2 + \beta_i^2 = k^2 n^2. \quad (4.2.10)$$

From equation 4.2.9, shows that in the plane the electromagnetic field behaves like a bi-dimensional wave with wave number β . In the direction orthogonal to the plane we have a one-dimensional wave equation, with potential defined by the index of refraction. For the refractive index considered in our case, the potential is a potential well. Equation 4.2.8 is actually a set of three equations, that can be divided in two categories, one deals with the component in the direction normal to the interface, denoted here as z , and two that deal with components parallel to the interface surface

$$\frac{\partial^2 \Phi_z(z)}{\partial z^2} - \kappa_i^2 \Phi_z(z) = 0, \quad (4.2.11a)$$

$$\frac{\partial^2 \Phi_t(z)}{\partial z^2} - \kappa_i^2 \Phi_t(z) = 0, \quad (4.2.11b)$$

where as before, i depends on the range of z . The linkage between neighboring ranges are described by the boundary conditions

$$\hat{n} \cdot (\epsilon_a \mathbf{E}_a - \epsilon_b \mathbf{E}_b) = 0 \quad (4.2.12a)$$

$$\hat{n} \cdot (\mathbf{B}_a - \mathbf{B}_b) = 0 \quad (4.2.12b)$$

$$\hat{n} \times (\mathbf{E}_a - \mathbf{E}_b) = 0 \quad (4.2.12c)$$

$$\hat{n} \times \left(\frac{1}{\mu_a} \mathbf{B}_a - \frac{1}{\mu_b} \mathbf{B}_b \right) = 0, \quad (4.2.12d)$$

where a and b can be either s, f or c . Using the assumption 4.2.4, these boundary conditions can be shown to be equivalent to

$$n_j^2 \Phi_{jz} = n_k^2 \Phi_{kz} \quad (4.2.13a)$$

$$\frac{\partial \Phi_{jz}}{\partial z} = \frac{\partial \Phi_{kz}}{\partial z}, \quad (4.2.13b)$$

where we did not show the equivalent boundary conditions for the tangential components Φ_t . Applying the boundary conditions on Φ_t will gives us a solution that is linearly independent to the solution of Φ_z . Although it is possible to obtain this second solution, it is easier make the assumption 4.2.5 and apply the boundary conditions, which this time will give rise to

$$\Phi_{jz} = \Phi_{kz} \quad (4.2.14a)$$

$$\frac{\partial \Phi_{jz}}{\partial z} = \frac{\partial \Phi_{kz}}{\partial z}. \quad (4.2.14b)$$

The wave equation 4.2.11a, with the potential 4.2.1, connected by conditions 4.2.13 is the problem of the wave in a square well. For a chosen value of k , continuous values of κ and therefore β exists. But for values of κ that solves the equation

$$\tan(h\kappa_f) = \frac{\kappa_c + \kappa_s}{\kappa_f \left[1 - \frac{\kappa_c \kappa_s}{\kappa_f^2} \right]} \quad (4.2.15)$$

solution of Φ are localized in the range $0 < z < h$, and hence, correspond to mode guided in the slab. In case boundary condition 4.2.14 is used then β will be

$$\tan(h\kappa_f) = \frac{\kappa_f \left[\frac{n_f^2}{n_c^2} \kappa_c + \frac{n_f^2}{n_s^2} \kappa_s \right]}{\kappa_f^2 - \frac{n_f^4}{n_c^2 n_s^2} \kappa_c \kappa_s} \quad (4.2.16)$$

Solution from assumption 4.2.4 together with boundary conditions 4.2.13 is called transversal electric (TE) mode, characterized by the absence of electric field in the direction of propagation, analogously the other solution is called transversal magnetic (TM), and features the absence of magnetic field in the direction of propagation.

It is worth remembering that the velocity which the phase propagates in plane is $v = \frac{\omega}{\beta}$ and group velocity $v_g = \frac{d\omega}{d\beta}$. From these we define effective index and group index as $n_{\text{eff}} = \frac{c}{v} = c \frac{\beta}{\omega} = \frac{\beta}{k}$ and $n_g = \frac{c}{v_g} = c \frac{d\beta}{d\omega}$.

4.3 Rectangular waveguide

In PIC, light guiding can be accomplished using rectangular waveguides. This is due to the fabrication process. It is important to note that the waveguide geometry and material dictates the dispersion relation of the guided light. Compared with the slab waveguide the rectangular waveguide has a symmetry in only one axis, labeled here as z . In this case the form which the solution to wave equation propagating takes in this medium is

$$\mathbf{E}(\mathbf{R}) = \Psi(\mathbf{r}) \Phi(z) \quad (4.3.1a)$$

$$\mathbf{B}(\mathbf{R}) = \Psi(\mathbf{r}) \Phi(z) \quad (4.3.1b)$$

where $\Psi(\mathbf{r})$ is a vector field and $\Phi(z)$ is a scalar function. Using separation of variables we arrive at the equations

$$\frac{\partial^2 \Phi(z)}{\partial z^2} + \beta(z)^2 \Phi(z) = 0 \quad (4.3.2)$$

$$\nabla_t^2 \Psi(\mathbf{r}) + (k^2 n^2 - \beta^2)^2 \Psi(\mathbf{r}) = 0 \quad (4.3.3)$$

where β is a propagation constant. Once found β we see that equation 4.3.2 is a one-dimension wave equation. β can be found by solving equation 4.3.3, considering the boundary conditions 4.2.12. For the rectangular waveguide, considered here, no analytical solution exist. A approximation for low index contrast was obtained¹, but is not the case for the system we are interested in (silicon and silicon oxide). In this work we resorted to solve this equation numerically using COMSOL² software package. This software uses a finite elements method³ to obtain numerical the solutions to the equation.

4.4 Ring resonators

Resonators are a distinguished technological element, and it couldn't be different for PICs. The kind of resonator we are interested in are ring resonators. Its main attractive feature is the ease with which we can design add and drop ports to it. We shall lay the definitions necessary to understand the resonance mechanism for later use. Consider the ring resonator with add and drop ports schematics⁴ in figure 4.4.1.

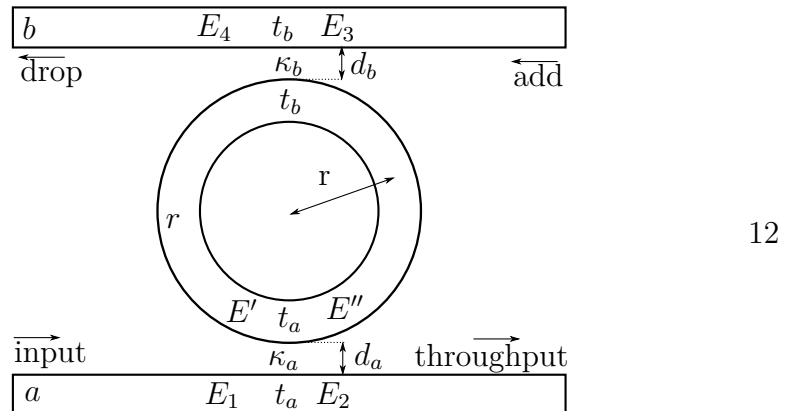


Figure 4.4.1: Ring resonator with input and drop waveguides schematics.

¹ Marcatili, “Dielectric rectangular waveguide and directional coupler for integrated optics”.

² <http://www.comsol.com/>

³ http://en.wikipedia.org/wiki/Finite_element_method

⁴ Little et al., “Microring resonator channel dropping filters”; Vorckel et al., “Asymmetrically coupled silicon-on-insulator microring resonators for compact add-drop multiplexers”.

The following equations describe how the field amplitude and phase are related

$$E_2 = t_a E_1 + i \kappa_a E', \quad (4.4.1a)$$

$$E'' = t_a E' + i \kappa_a E_1, \quad (4.4.1b)$$

$$E' = t_b E'' \tau e^{i\phi}, \quad (4.4.1c)$$

$$E_4 = i \kappa_b E'' \sqrt{\tau} e^{i\phi/2}, \quad (4.4.1d)$$

$$E_3 = 0, \quad (4.4.1e)$$

where κ_a and κ_b are the coupling coefficients between the ring resonator (r) and the signal waveguides (a, b), $t_{a,b} = \sqrt{1 - \kappa_{a,b}}$ the transmission coefficients, τ ring round trip field transmission and $\phi = k_0 n_{\text{eff}} L_{\text{eff}} = k_0 n_{\text{eff}} 2(\pi r + L_s)$ is the phase shift for one round-trip along the resonator. The efficiency at which light power is transmitted from the input to the drop port D (drop efficiency) is

$$D = |S_{41}|^2 = \left| \frac{E_4}{E_1} \right|^2 = \frac{\kappa_a^2 \kappa_b^2 \tau}{1 + t_a^2 t_b^2 \tau^2 - 2 t_a t_b \tau \cos \phi} \quad (4.4.2)$$

and the transmission efficiency from input to the throughput port T is

$$T = |S_{21}|^2 = \left| \frac{E_2}{E_1} \right|^2 = \frac{t_a^2 + t_b^2 \tau^2 - 2 t_a t_b \tau \cos \phi}{1 + t_a^2 t_b^2 \tau^2 - 2 t_a t_b \tau \cos \phi} \quad (4.4.3)$$

It is interesting to observe the following derivation of equation 4.4.2 considering that the field (E_4) at the drop port can be obtained by sum over all possible paths

$$E_4 = \kappa_b \kappa_a E_1 \tau^{1/2} e^{i\phi/2} \left[1 + t_a t_b \tau e^{i\phi} + (t_a t_b \tau e^{i\phi})^2 + \dots + (t_a t_b \tau e^{i\phi})^n \right] \quad (4.4.4)$$

reminding that more than one path is possible if we count multiple round trips. Notice that the above relation is a geometrical sum, but it is also the Fourier series of exponential decaying constant. Which can be written with the sum notation as

$$E_4 = \kappa_b \kappa_a E_1 \tau^{1/2} e^{i\phi/2} \sum_{n=-\infty}^{\infty} e^{n \ln(t_a t_b \tau)} S(n) e^{in\phi} \quad (4.4.5)$$

where $S(x)$ is the Heaviside step function. According to relation B.1.1 we have

$$E_4 = \kappa_b \kappa_a E_1 \tau^{1/2} e^{i\phi/2} \sum_{n=-\infty}^{\infty} FT \left[e^{x \ln(t_a t_b \tau)} S(x), x \right] \left(\frac{\phi}{2\pi} - m \right) \quad (4.4.6)$$

where $FT[f(x), x]$ denotes the Fourier transform of function f relative to x . From this it is clear that the drop port transfer function is dependent on how the field amplitude varies in each

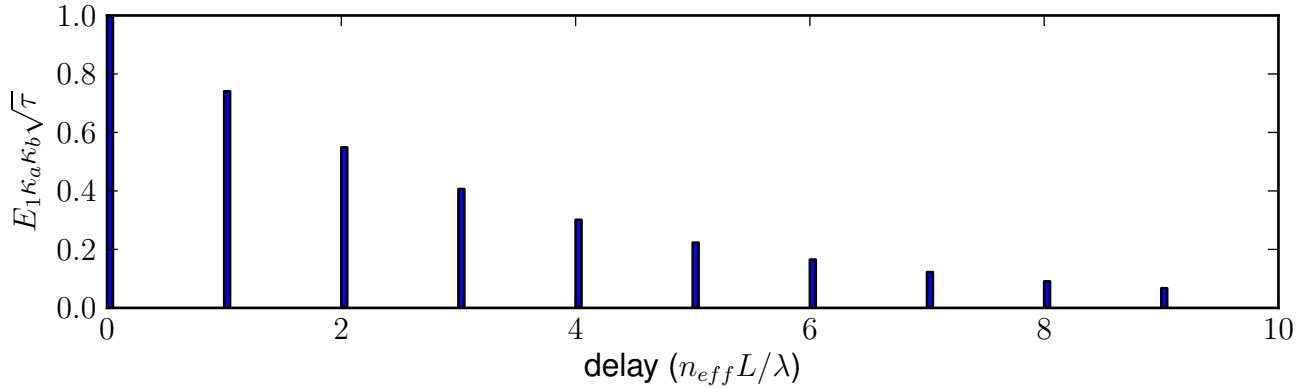


Figure 4.4.2:

path. In this case the field amplitude varies as an exponential decay whose Fourier transform is a Poisson function. The contribution of the sum will be a comb of Poisson functions, with maximum each time $\phi/(2\pi)$ is an integer. Which translates to

$$\lambda m = n_{\text{eff}} L_{\text{eff}}, \quad (4.4.7)$$

the cavity optical path-length is equal to a integer number of wavelength. The distance between peaks, called free spectral range (FSR), is

$$\text{FSR} = \frac{c}{n_g L_{\text{eff}}}, \quad (4.4.8)$$

Another important equation that can be derived from 4.4.2 is the Q factor

$$Q = \frac{\lambda_0}{\Delta\lambda_{\text{FWHM}}} = \frac{\pi L_{\text{eff}} n_g}{\lambda_0 \arccos \left(\frac{1-t_a^2 t_b^2 \tau - 4t_a t_b \tau}{-2t_a t_b \tau} \right)}, \quad (4.4.9)$$

where we see that it depends mainly on the coupling between the cavity to the waveguides and the intrinsic loss.

4.5 Material optical properties

Geometric variation of components allows for the properties shown so far, although to guide light it was key to leverage difference in index of refraction of distinct materials. But a diversity of other material optical properties can be exploited for a variety of ends. Thermo-optic effect allows for an easy way to change materials index of refraction, despite the fact that is relatively slow. Plasma dispersion together with electron injection can be used to rapidly and electrically change the index of refraction of semiconductors.

4.5.1 Material dispersion

Material index of refraction varies with the frequency of the electromagnetic radiation propagating on it. This dispersion modifies light group velocity determines the resonators FSR, and therefore, it cannot be ignored. Good estimation of materials index of refraction can be made using Sellmeier's empirical relation⁵

$$n^2(\lambda) = 1 + \sum_i A_i \frac{\lambda^2}{\lambda^2 - \lambda_i^2}. \quad (4.5.1)$$

where λ is the vacuum wavelength is in micrometers, A_i and λ_i are the Sellmeier coefficients. The table 4.1 shows the Sellmeier's coefficients for Si⁶ and SiO₂.

	λ_1	λ_2	λ_3	A_1	A_2	A_3
Si	0.301516485	1.13475115	1104.0	10.6684293	0.00304347484	1.54133408
SiO ₂	0.0260605	0.116241	9.89616	0.6961663	0.4079426	0.8974794

Table 4.1: Sellmeier coefficients for silicon and silicon oxide.

4.5.2 Thermo optic effect

The refractive index of optical materials is not a constant parameter over the temperature region in which the materials, such as crystals, semiconductor, and glasses are used. The variation of refractive index with the temperature at a constant pressure is called the thermo-optic coefficient. It is denoted as dn/dT , where n and T are the refractive index and temperature, respectively. Its unit is per degree centigrade or Kelvin. In comparing with silica, silicon has a relatively high thermo-optic coefficient of $\partial n/\partial T = (1.86 \pm 0.08) \times 10^{-4} K^{-1}$ ⁷. Although this property is hurdle for in the stability of electro optic silicon modulator, it is also a convenient way to tune the refractive index.

⁵http://en.wikipedia.org/wiki/Sellmeier_equation

⁶Tropf, Harris, and Thomas, "Optical Materials: Visible and Infrared".

⁷Cocorullo and Rendina, "Thermo-optical modulation at 1.5 mu m in silicon etalon".

Chapter 5

Diffraction Grating Spectrometers

It is difficult to enumerate all the contributions to society that the use of diffraction gratings has brought. Its role on identifying the discrete energy levels of atoms provided a significant amount of information to the development of quantum mechanics. Currently its use in the identification or quantification of chemical compounds and its structure constitutes the majority end usage of diffraction gratings.

5.1 Kirchhoff's diffraction theory

To establish the terminology we give a brief review of diffraction theory. We start with Huygens principle that states that each point of a wavefront is a new wave source. With such principle in mind, the problem of the diffraction by a small aperture, depicted at figure 5.1.1, can seen in the following way. If waves are generated by a point source P_0 at a point Q the wave field

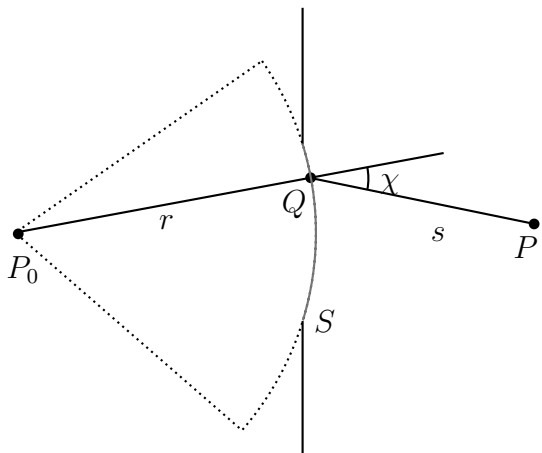


Figure 5.1.1:

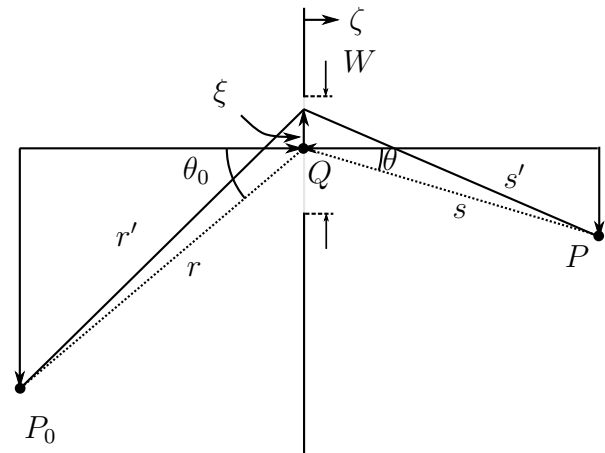


Figure 5.1.2:

should be

$$E(Q) = E(P_0) \frac{e^{ikr}}{r}, \quad (5.1.1)$$

where r the distance between P_0 and Q , and k is the wavenumber. The field at a point P due to source at Q is then

$$E(P) = E(P_0) \frac{e^{ikr}}{r} \frac{e^{iks}}{s} K(\chi), \quad (5.1.2)$$

where $K(\chi)$ is an inclination factor which describes the variation with direction of the amplitude of the secondary waves, χ been the angle between the primary wavefront normal and the direction of QP . The electric field at P due to all wave sources at surface S will then be

$$E(P) = E(P_0) \int_S \frac{e^{ikr}}{r} \frac{e^{iks}}{s} K(\chi) dS. \quad (5.1.3)$$

The Huygens principle was then place on a sounder mathematical basis by Kirchhoff¹. Using Green's theorem on the time-independent wave equation $(\nabla^2 + k^2) E = 0$, one can derive that

$$E(P) = \frac{1}{4\pi} \int_S \left[E(Q) \frac{\partial}{\partial n} \left(\frac{e^{iks}}{s} \right) - \frac{e^{iks}}{s} \frac{\partial E}{\partial n}(Q) \right] dS, \quad (5.1.4)$$

where $\partial/\partial n$ is the differentiation along the normal to S . This is one form of the integral theorem of Helmholtz and Kirchhoff. Since $\frac{\partial}{\partial n} \left(\frac{e^{iks}}{s} \right) = \frac{e^{iks} ik}{s} \left[1 - \frac{1}{iks} \right] \cos(n, s)$, considering that $ks \gg 1$

$$E(P) = \frac{1}{4\pi} \int_S \frac{e^{iks}}{s} \left[ikE(Q) \cos(n, s) - \frac{\partial E}{\partial n}(Q) \right] dS, \quad (5.1.5)$$

For a point source at P_0 the field at Q is $E(Q) = E(P_0) \frac{e^{iks}}{s}$. The Fresnel-Kirchoff formula will be

$$E(P) = \int_S E(P_0) \frac{-ik}{4\pi} \frac{e^{ikr}}{r} \frac{e^{iks}}{s} [\cos(n, r) - \cos(n, s)] dS, \quad (5.1.6)$$

which is known as the Fresnel-Kirchhoff diffraction formula. Since $\cos(n, r) = 1$ and $(n, s) = \pi - \chi$ the above integral is

$$E(P) = E(P_0) \int_S \frac{e^{ikr}}{r} \frac{e^{iks}}{s} \frac{-ik}{4\pi} (1 + \cos \chi) dS. \quad (5.1.7)$$

This validates the Huygens principle. Comparing with 5.1.3 we note that

$$K(\chi) = \frac{-ik}{4\pi} (1 + \cos \chi). \quad (5.1.8)$$

A special case of the Fresnel-Kirchhoff diffraction formula is the Fraunhofer diffraction, in

¹Section 8.3 Born and Wolf

this case, the diffracting element is much smaller than the distances where the field is being evaluated. Figure 5.1.2, depict such case. Where the assumption is that $\frac{W}{r}$ and $\frac{W}{s} \ll 1$. In such case we have that

$$s' \approx s + \xi \sin \theta \quad (5.1.9)$$

$$r' \approx r + \xi \sin \theta_0 \quad (5.1.10)$$

which will cause the Fresnel-Kirchhoff formula to be approximated to

$$E(P) = C \int_{-W/2}^{W/2} e^{ik\xi(\sin \theta_0 + \sin \theta)} d\xi, \quad (5.1.11)$$

where $C = E(P_0) \frac{-ik}{4\pi} \frac{e^{ikr}}{r} \frac{e^{iks}}{s} (\cos \theta - \cos \theta_0)$

$$E_{\text{aperture}} = CW \text{sinc} \left[(\sin \theta_0 + \sin \theta) \frac{Wk}{2\pi} \right]. \quad (5.1.12)$$

5.2 Diffraction grating

A diffraction grating may be defined as any arrangement which imposes on an incident wave a periodic variation of amplitude, phase, or both. Let us now consider a one-dimensional grating consisting of N parallel apertures on one surface. Let the ξ -plane coincide with the plane face of the plate, and let d be the period in the ξ direction. As shown in figure 5.2.1. Assume that the direction of propagation of the wave incident upon the grating is in the plane of the figure, making an angle θ_0 with $O\xi$, and let θ denote the angle which $O\xi$ makes with the line joining a very distant point of observation P with the grating.

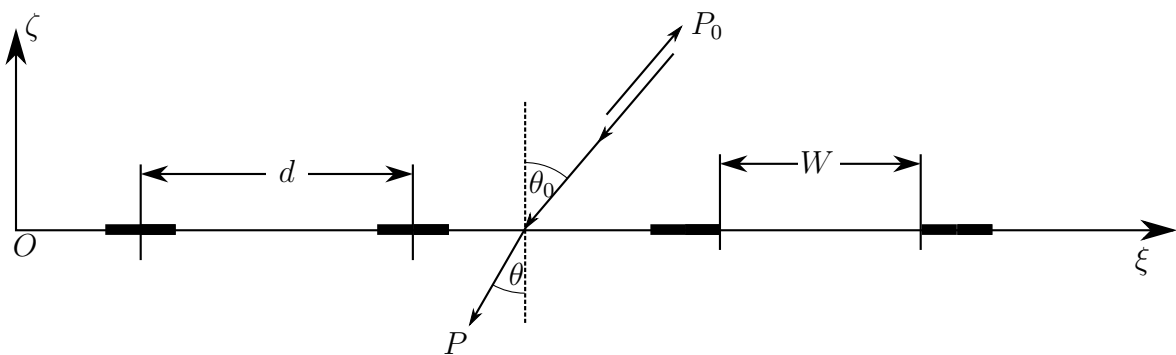


Figure 5.2.1: Diffraction grating cross section.

Fraunhofer aperture formula 5.1.11 can be analogously used to calculate the field at P

$$E(P) = C \sum_{n=0}^N \int_{nd-W/2}^{nd+W/2} e^{ik\xi(\sin \theta_0 + \sin \theta)} d\xi, \quad (5.2.1)$$

making the change of variable $\xi = \xi' - nd$, taking out of the integral all terms factors that don't depend on ξ' we arrive at

$$E_{\text{grating}} = E_{\text{aperture}} \sum_{n=0}^N e^{-iknd(\sin \theta_0 + \sin \theta)}, \quad (5.2.2)$$

Hence

$$I(p) = |E(p)|^2 = I_{\text{aperture}} \frac{1 - \cos Nkdp}{1 - \cos kdp} \quad (5.2.3)$$

where $I(p) = |E(p)|^2$ and $p = \sin \theta_0 + \sin \theta$. If we introduce the function

$$H(N, x) = \left(\frac{\sin Nx}{\sin x} \right)^2, \quad (5.2.4)$$

the formula 5.2.3 for the intensity may be written as

$$I(p) = H\left(N, \frac{kdp}{2}\right) I_{\text{aperture}}. \quad (5.2.5)$$

Before discussing the implications of this formula we note that according to 5.2.2, the light distribution is the same as that due to a set of coherent secondary sources each characterized by the same amplitude function $|E^{(0)}(p)|$ and with phases that differ from each other by integral multiples of kdp . To see the significance of this phase difference consider two corresponding points A and B in the neighboring grooves of the grating (Fig. 5.2.2). Since the effect of the grating is to impress a periodic variation onto the incident wave, it follows that the path difference between the light arriving at A and at B is the same as in the absence of the grating, i.e. it is equal to $AK = d \sin \theta_0$, K denoting the foot of the perpendicular from B on to the ray incident at A . Further, the light path from B in the direction θ exceeds the light path from A by $BL = d \sin \theta$, L being the foot of the perpendicular from A on to the ray diffracted at B in the direction θ . Hence the total path difference between light arriving at the distant point of observation from corresponding points in two neighboring grooves is

$$BL - AK = d(\sin \theta - \sin \theta_0) = dp, \quad (5.2.6)$$

and the corresponding phase difference is $2\pi dp/\lambda = kdp$.

Formula 5.2.5 expresses $I(p)$ as the product of two functions: one of them, I_{aperture} , represents the effect of a single period of the grating; the other, H , represents the effect of the interference of the light from different periods. The function $H(N, x)$ has maxima, each of height N^2 , at all points where the denominator $\sin^2 x$ vanishes. Hence $H(N, kdp/2)$ has maxima of height N^2 when

$$p \equiv \sin \theta - \sin \theta_0 = \frac{m\lambda}{d}, \quad (5.2.7)$$

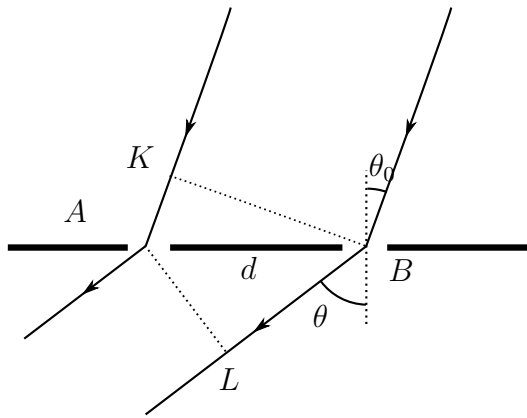


Figure 5.2.2: Illustrating the theory of diffraction grating.

where m is an integer.

The integer m represents, according to 5.2.6, the path difference in wavelengths between light diffracted in the direction of the maximum, from corresponding points in two neighboring grooves. We call m the *order of interference*. Between these principal maxima there are weak secondary maxima (see figure 5.2.3), the first secondary maximum being only a few percent of the principal maximum when N is large. The maxima are separated by points of zero intensity at $x = kdp/2 = \pm n\pi/N$, i.e. in directions given by

$$p \equiv \sin \theta - \sin \theta_0 = \frac{n\lambda}{Nd} \quad (5.2.8)$$

where n is an integer, and the case where n/N is an integer being excluded.

The function I_{aperture} depends on the form of the period. Suppose that it has principal maximum for some direction $p = p'$ and that on both sides of the maximum it falls off slowly in comparison with H . Then $I(p)$ will have the general form of the interference function H , but will be 'modulated' by I_{aperture} . Thus $I(p)$ will still have sharp maxima near the directions $p = m\lambda/d$. Since these directions (except for $m = 0$) depend on the wavelength, we see that the grating will decompose a beam of non-monochromatic light into *spectral orders*.

It is evident that if the width of each aperture is very small, of the order of a wavelength (as is often the case in practice) the formula derived on the basis of Kirchhoff's approximation, can evidently no longer be expected to hold. In such cases more refined considerations must be made to determine the detailed distribution of the intensity. We may, however, expect that the main qualitative features indicated by our elementary theory, namely the existence of sharp maxima whose positions are essentially determined by the interference function H , remain even when the grooves are very narrow, provided, that the intensity function of a single period varies slowly in an interval of the order $\Delta p = \lambda/d$. Let us now consider the resolution

that may be attained with a grating. The separation between a primary maximum of order m and a neighboring minimum is, according to 5.2.8, given by

$$\Delta p = \frac{\lambda}{Nd}. \quad (5.2.9)$$

If the wavelength is changed by an amount $\Delta\lambda$, the m th-order maximum is according to 5.2.7, displaced by an amount

$$\Delta'p = \frac{|m|}{d}\Delta\lambda. \quad (5.2.10)$$

Assuming that the lines of wavelength $\lambda \pm \frac{1}{2}\Delta\lambda$ will just be resolved when the maximum of the one wavelength coincides with the first minimum of the other we have on he limit of resolution in the m th order, $\Delta p = \Delta'p$, i.e.

$$\frac{\lambda}{\Delta\lambda} = |m| N. \quad (5.2.11)$$

Thus, *the resolving power is equal to the product of the order number m and the number N of the grooves*. For the m th order we have, according to, that $d(\sin\theta - \sin\theta_0) = m\lambda$, so that we may also express the resolving power in the form

$$\frac{\lambda}{\Delta\lambda} = \frac{Nd |\sin\theta - \sin\theta_0|}{\lambda}. \quad (5.2.12)$$

Because of 5.2.6 this implies that *the resolving power is equal to the number of wavelengths in the path difference between rays that are diffracted in the direction θ from the two extreme ends (separated by distance Nd) of the grating*. It is to be noted that since $|\sin\theta - \sin\theta_0|$ cannot exceed 2, the resolving power that can be attained with a grating of overall width w can never exceed the value $2w/\lambda$.

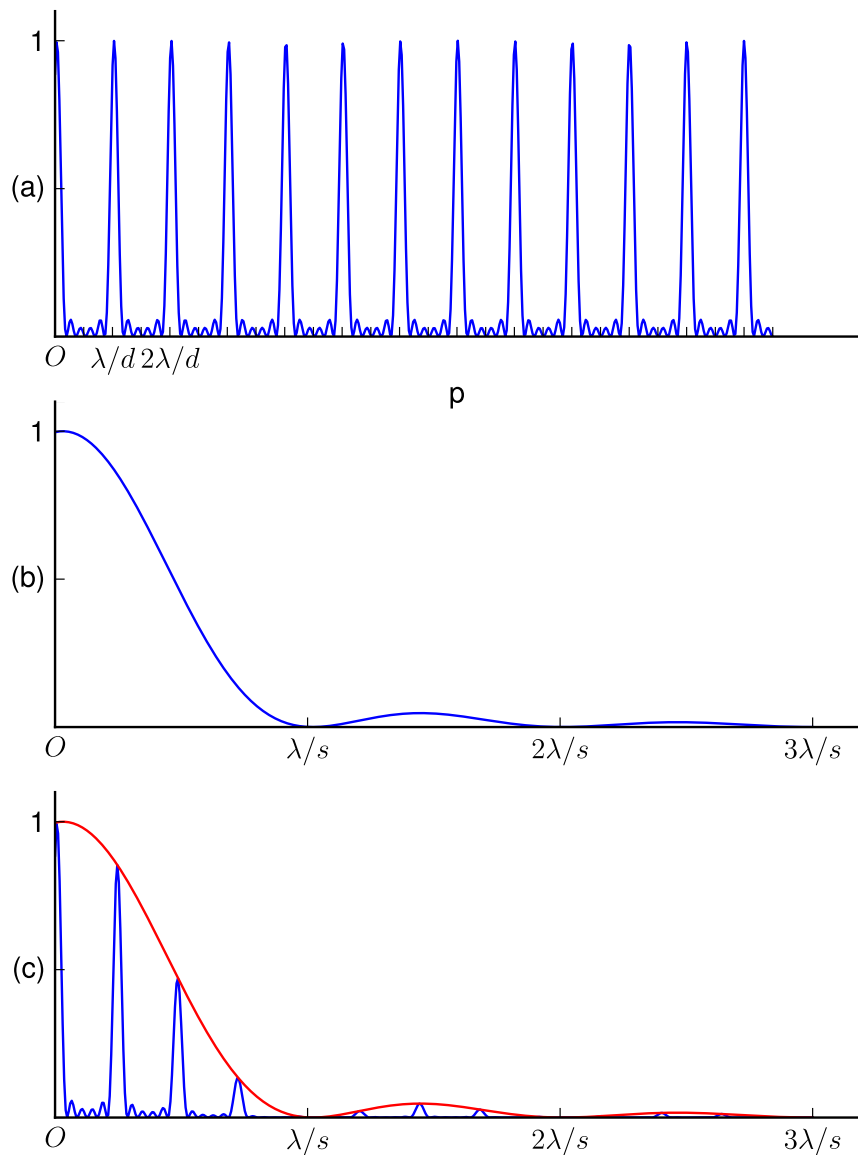


Figure 5.2.3:

5.2.1 Free spectral range

From the resolving power equation 5.2.11, we conclude that spectrometer should be operated on high diffraction order so as to minimize the device size for a given resolution. Unfortunately, from the grating equation 5.2.7, $p \equiv \sin \theta - \sin \theta_0 = \frac{m\lambda}{d}$, we see that it is possible for light from different wavelength in different diffraction orders to be diffracted to the same angle θ ,

sufficing that

$$m_i \lambda_i = m_j \lambda_j \quad (5.2.13)$$

for $i \neq j$, so for example light diffracted in order 1 at wavelength 1500 nm is diffracted in the same direction as light diffracted from order 2 wavelength 750 nm. To avoid this ambiguity, it is of interest to know when this condition happens. From the grating equation we see that p does not make sense outside the interval $[0,1]$, therefore, $0 \leq \frac{m\lambda_m}{Nd} \leq 1$ we then find that for the diffraction order m the wavelength range that is going to be diffracted is:

$$0 \leq \lambda_m \leq \frac{d}{m}. \quad (5.2.14)$$

So for the first order the wavelength range that exists is every wavelength below Nd , for order 2 every wavelength below $Nd/2$ and so on. We see then, that for order 1 the range $[Nd, Nd/2]$ is occupied solely by order one. For order 2 the range $[Nd/2, Nd/3]$, for order m , $[Nd/m, Nd/(m + 1)]$. We see that the range width $\Delta\lambda_m$ for which there is no overlapping diffraction, called *free spectral range*, can be computed as

$$\Delta\lambda_m = \frac{d}{m} - \frac{d}{m+1} = \frac{d}{m(m+1)}, \quad (5.2.15)$$

we can replace the dependence on d for the wavelength in the center of the free spectral range λ_{Cm} ,

$$\lambda_{Cm} = \frac{d}{m} - \frac{\Delta\lambda_m}{2} = \frac{d}{m(m+1)}(m + 0.5), \quad (5.2.16)$$

It is worth noting that although λ_{Cm} is in the middle of the spectral range $\Delta\lambda_m$ the wavelengths are not linearly distributed along the angle range that it is diffracted to, and therefore λ_{Cm} is not located at the center of the angle range of the m th order free spectral range. We see then that the free spectral range depends inversely with the diffraction order used,

$$\Delta\lambda_m = \frac{\lambda_{Cm}}{m + 0.5}. \quad (5.2.17)$$

This fact, ties to use a maximum operating diffraction order to the wavelength range and central wavelength we want the diffraction grating to operate.

5.3 Planar devices

The previous exposition on diffraction grating does not change with the medium in which the device is built on. But since we are interested in spectrometer integrated on chips, it is worth highlighting the characteristics of this device. From this point two features stand out as very

different from regular free space spectrometer. First is that light is always guided in a slab waveguide, the confinement of light in one dimension changes the nature of the system from a three dimensional to bi-dimensional one, and this fact causes the light power to decay with the inverse of the distance as it moves away from the source. The other difference is the change of the dispersion due to both the material and the confinement effect. The outcome of this is that for all the results in the previous section, the wavelength variable that needs to be considered is the effective wavelength in the medium.

$$\lambda_{\text{eff}} = \frac{\lambda}{n_{\text{eff}}} \quad (5.3.1)$$

5.4 Spectrometer architectures

Several architectures to build diffraction grating spectrometer exist. Due to the compromise between lowest size \times resolution of the Rowland design, it was chosen to build the spectrometers. The Czerny-Turner is presented here to introduce spectrometer because its design is easily understandable. Arrayed waveguide grating has been the most used planar (on chip) version of spectrometer. Marketed as wavelength division multiplexer (WDM) in the telecommunication sector, this layout is shown in order to understand why it is not fit for the role as a high resolution on-chip spectrometer.

5.4.1 Czerny-Turner

Due to its modularity this architecture is probably the best to introduce spectrometers. It is composed of two slits, two concave mirrors and a diffraction grating. As shown in figure 5.4.1, the light to be analyzed is shone through the entrance slit. Due to diffraction, the light fans out as it propagates to the collimating concave mirror where light is collimated and reflected in the direction of the diffraction grating. The diffraction grating then, deviates light from each different wavelength (optical frequencies) into different angles following the equation 5.2.7. A focusing concave mirror focus the light coming from the diffraction grating and deflects it to the detector slit.

The function of the entrance slit is to filter spatial optical modes that are inputted into the system. For best filtering the slit has to transmit only a single spatial mode. This is achieved by making the slit width of the order of the light wavelength. Decreasing slit width will increase the beam spread angle, as depicted in figure 5.4.2, for a chosen final beam width this will allow the collimating concave mirror to be placed nearer to the slit decreasing the device size. However, reducing the slit width will also decrease the fraction of transmitted light, therefore lowering the device sensitivity.

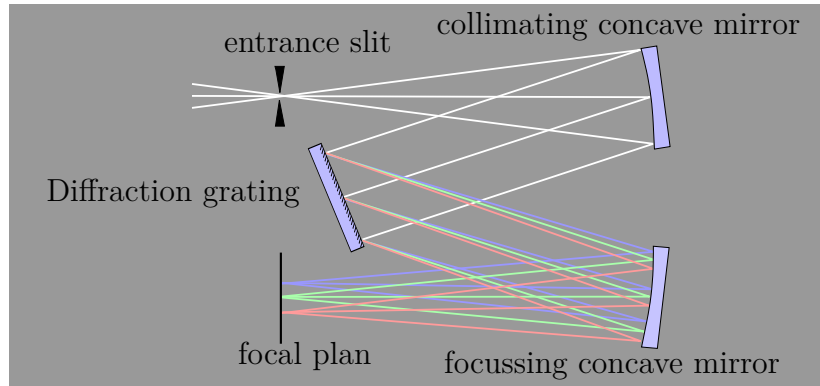


Figure 5.4.1: Czerny-Turner architecture.

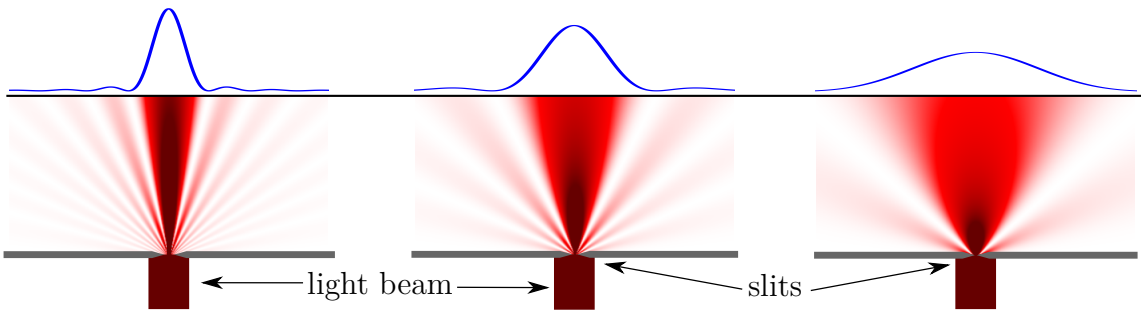


Figure 5.4.2: Different effects of slit width.

As described by its name the collimating concave mirror collimates the light coming from the entrance mirror and redirects it to the diffraction grating. In order to collimate² the input light, the curvature radius should be equal twice the distance from the entrance slit to the center of the collimating concave mirror. The mirror diameter must be bigger than the beam width arriving at it to avoid light leakage through the mirror edges.

The diffraction grating deviates light from each different wavelength into different angles, as described by equation 5.2.7. Details on how the light is diffracted were explained in section 5.2. Roughly, the number of illuminated grooves, which is equal to the beam diameter divided by the groove pitch, will determine the resolving power of the spectrometer, as shown in equation 5.2.11.

To quantify the amount of light deviated in each direction, we use a focusing concave mirror which will map light with different direction and focus them each into a distinct point in a plane. Clearly, the size of the focusing mirror must be such that it collects most of the light coming from the diffraction grating. This means that it must be bigger than the beam size and account for the spread of different wavelengths.

A detector is placed at a point in the focus plan to measure the light power. Optimum detector size is of the order of the entrance slit width, limited also by the resolving power of the diffraction

²http://en.wikipedia.org/wiki/Collimated_light

grating. Placing a exit slit in the focus plane followed by a detector, can be used as an alternative for the slit size detector.

5.4.2 Rowland

Rowland³ found a way to incorporate the collimating and focusing elements into the diffraction grating. This layout not only decreased the final device size, but also eliminates spherical and astigmatism aberrations due to the auxiliary concave mirrors.

The design consists in the use of a concave diffraction grating of radius $2R$. The entrance and exit slits positions are located in a circle of radius R tangent to the diffraction grating sphere. Or more precisely tangent to one of the equator of the diffraction grating sphere. For optimum area usage, the equator should be perpendicular to the diffraction grating grooves and passing through the grating center.

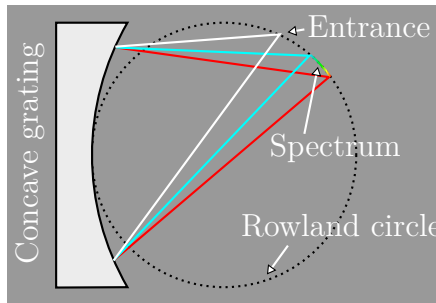


Figure 5.4.3: Rowland design.

5.4.3 Arrayed Waveguide Grating (AWG)

The resolving power of a diffraction grating is proportional to the number of grooves and diffraction order, as shown in equation 5.2.11. Diffraction grating based on ruled surfaces can not achieve diffraction order greater than 20. Introduced by Takahashi et. al.⁴, this limitation can be overcome by replacing the grating grooves by an array of waveguides. To understand how the introduction of waveguide helps it is necessary to understand more generally what diffraction order is. We say that certain diffraction peak is of order m if each wave from the set that was constructively interfered to form the interference peak is delayed from one another by m periods. On traditional ruled surface diffraction gratings, wavefront from different period are made to interfere by making the wave travel different path lengths by taking path that deviates from the equal angle reflection.

³Rowland, “On concave gratings for optical purposes”.

⁴Takahashi et al., “Arrayed-waveguide grating for wavelength division multi/demultiplexer with nanometre resolution”.

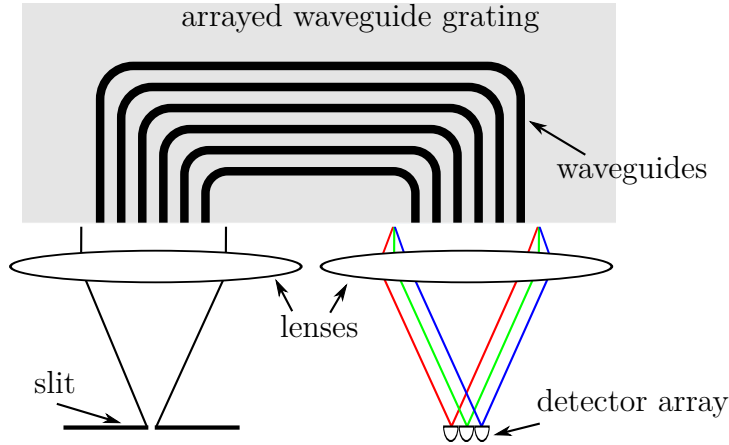


Figure 5.4.4: Arrayed waveguide grating schematics. Notice that each waveguide has a different path-length.

By guiding light through waveguide it is possible to increase the difference of paths length among different waveguides, achieved by only changing the waveguides lengths. Each waveguide of the waveguide array would function like a groove in the diffraction grating, but since waveguide length is only limited by its intrinsic loss, the difference of paths length can be on the order of hundreds of wavelength, corresponding to a grating that operate at a diffraction order of hundreds.

Unfortunately there is a drawback in increasing diffraction order, the free spectral range as described in 5.2.17, decreases with the inverse of the of the diffraction order. For instance, an arrayed waveguide grating working on diffraction order 100 at wavelength 1500 nm would have a FSR of only 15 nm. Although this range is useful for fiber optics telecommunications, this bandwidth is too small for most spectroscopic applications, optical coherence tomography or ultra-fast oscilloscopes⁵. Since we want to achieve a wide spectrum range, this architecture is not fit for us.

5.5 Grating illuminated by a gaussian beam

In section 5.2, it was assumed that the whole grating was uniformly illuminated. In practice, this case not always occurs. Light source is normally a collimated light from a slit, pin hole or fiber optics, where for best resolution, single mode output should pass through. In those cases the transversal power profile is better modelled by a Gaussian than by a square profile, see figure 5.5.1. To adjust the resolving power equation 5.2.11 to account for the Gaussian profile illumination we have to alter the squared illumination assumption in equation 5.2.2. Using this

⁵Foster et al., “Silicon-chip-based ultrafast optical oscilloscope”.

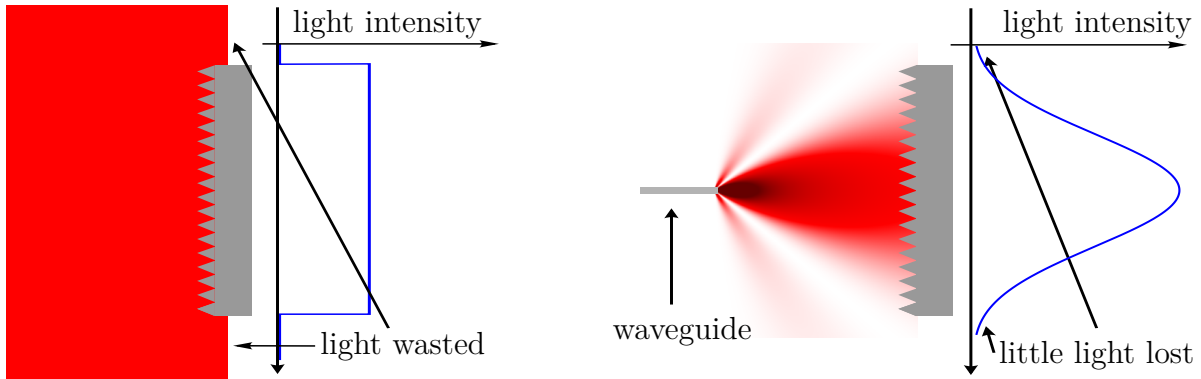


Figure 5.5.1: Diffraction grating illuminated by a (a) uniform intensity beam, (b) Gaussian beam.

relation we can equate

$$E(p) = E_{\text{aperture}}(p) \int \sum_{n=-\infty}^{\infty} \delta(x-n) \text{rect}\left[\frac{x}{2(N-1)}\right] e^{-ikxdp} dx \quad (5.5.1)$$

where

$$\text{rect}(x) = \begin{cases} 0 & \text{if } |x| > \frac{1}{2} \\ \frac{1}{2} & \text{if } |x| = \frac{1}{2} \\ 1 & \text{if } |x| < \frac{1}{2}. \end{cases} \quad (5.5.2)$$

the $\text{rect}(x)$ function corresponds to the squared illumination assumption, for a Gaussian illumination we simply replace the function by a Gaussian function

$$\text{gauss}(x) = \exp\left[-4 \ln 2 \left(\frac{x}{w/d}\right)^2\right] \quad (5.5.3)$$

where d is the grating pitch, and w is the Full Width at Half Maximum field amplitude of the illuminating beam at the grating. Replacing the Dirac delta comb by its Fourier series

$$\sum_{k=-\infty}^{\infty} \delta(x-k) = \sum_{m=-\infty}^{\infty} e^{i2\pi mx}, \quad (5.5.4)$$

we get

$$E(p) = E_{\text{aperture}}(p) \sum_{m=-\infty}^{\infty} \int \exp\left[-4 \ln 2 \left(\frac{x}{w/d}\right)^2\right] e^{-i2\pi x(kdp/2\pi-m)} dx \quad (5.5.5)$$

performing the integral we obtain a comb of Gaussian

$$E(p) = E_{\text{aperture}}(p) \frac{w}{\sqrt{2}} \sum_{m=-\infty}^{\infty} \exp \left[-\frac{1}{4} \left(\frac{kdp}{2\pi} - m \right)^2 \frac{(w/d)^2}{4 \ln 2} \right], \quad (5.5.6)$$

where each Gaussian is centered on the diffraction order m . From 5.5.6 we get

$$\frac{kdp}{2\pi} = m \text{ or } p = \frac{\lambda m}{d}. \quad (5.5.7)$$

From equation 5.5.6 we can define the wavelength width $\Delta\lambda$ such that the power of wavelength λ at diffraction order m , is halven as a been

$$\Delta p = 2 \ln 2 \frac{\lambda}{w}, \quad (5.5.8)$$

or using the grating equation 5.5.7 e define the resolving power for a Gaussian beam illuminated diffraction grating as

$$\frac{\lambda}{\Delta\lambda} = 4\sqrt{2} \ln 2 \frac{wm}{d} \quad (5.5.9)$$

It is worth noting that the relationship between the electric field amplitude FWHM w at the grating and the power FWHM W is

$$W = \frac{w}{\sqrt{2}} \quad (5.5.10)$$

Therefore

$$\frac{\lambda}{\Delta\lambda} = 8 \ln 2 \frac{Wm}{d}. \quad (5.5.11)$$

5.6 Aberrations

The resolving power equation 5.2.11 states that the resolution of a diffraction grating depends linearly with the wavelength. Unfortunately, that relation is only valid for plane waves. To use the segregation capability of the diffraction grating, it is necessary to have a source of plane waves and to measure the light power that goes to a different direction after diffraction from the grating. Sources and detector are space localized at endpoints. But employing lenses, it is possible to convert a space localized mode to an angle localized mode, as discussed on the Czerny-Turner configuration in section 5.4.1. This conversion, however, is not perfect. In geometrical optics terms, this means that rays that enter parallel in a lens (or any other focusing device) does not converge to a single point after the lens and with the phase arriving at exactly the same time. Integrating the lens into the grating, as done in Rowland configuration in section 5.4.2, does not readily eliminate the problem, but the potential to fabricate designs with freedom to choose any geometry and dispersion might be the solution.

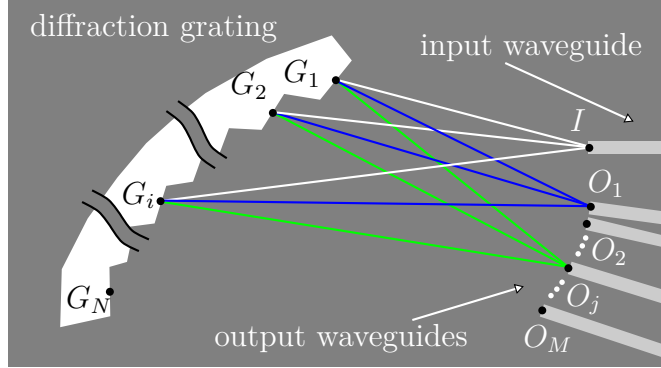


Figure 5.6.1: Diffraction grating spectrometer point problem sketch.

First we will state formally what conditions need to be satisfied in the design of an aberration free spectrometer. No mathematical solution exists, but we can show two corrections, named one point and two point stigmatic correction, that reduce aberrations.

5.6.1 Aberration free conditions

The problem can be stated as follows: Light coming from a point I fan out to a diffraction grating where the i -th groove, of N grooves, is located at G_i . At each groove light is reflected, fans out again and propagates to a set of M output waveguides which the j -th waveguide is located at O_j , as shown in figure 5.6.1. To perfectly separate light from different wavelengths, we would like that all light which has wavelength λ_j coming from each groove arrive in phase at the output point O_j . Furthermore, we would like that light coming from each different groove arrives at O_j in a different period. The previous conditions can be expressed by a system of $N \times M$ nonlinear algebraic equations with the prototype

$$\overline{IG_i} + \overline{G_iO_j} = \lambda_j (a_j + mi) \text{ for } (i = 1, 2, \dots, N) \text{ and } (j = 1, 2, \dots, M), \quad (5.6.1)$$

where m is an integer number which defines the diffraction order and a_j is a constant that states that the absolute path length does not matter, only the path length difference between light coming from different routes do. It is worth emphasizing that the path length evaluation should consider the medium refractive index, from this perspective one can interpret that light is propagating in a non-Euclidean space.

For the case of a flat space in a plane, equation 5.6.1 can be expanded to

$$\sqrt{(I_x - G_{ix})^2 + (I_y - G_{iy})^2} + \sqrt{(O_{jx} - G_{ix})^2 + (O_{jy} - G_{iy})^2} = \lambda_j (a_j + mi), \quad (5.6.2)$$

for $(i = 1, 2, \dots, N)$ and $(j = 1, 2, \dots, M)$. As discussed in sections 5.2 and 5.5, high resolution implies in the use of a high number of grooves N with numbers typically achieving, thousands

to millions. The number of channels M is, of course, as a wish of the costumer but numbers around thousands are very typical. These implies that the set of equations 5.6.2 is comprised of $M \times N$ equations with and $2N + 2M + 1$ variables.

Using a different approach it was shown that there was no configuration in a flat surface that has no aberration⁶, but nothing has been shown for non-Euclidean surfaces. Fabrication of non-Euclidean surfaces have been used to demonstrate cloaking devices⁷. Although it is not possible to find a solution for all equations, solving for one and two points dramatically improves aberration.

5.6.2 One point stigmatic correction

Although no aberration free configuration for all spectrometer channels exists, it can be easily seen the the equation system 5.6.2 is solvable for $M \leq 2$. This means that it is possible to find a configuration where there is no aberration for up to two channels, or also known as stigmatic point.

For one stigmatic point, a degree of freedom is left undefined. We can use the freedom to choose the surface in which the diffraction grooves are going to be positioned⁸. Using the Rowland design as a basis, we show here how to place the grooves on a circle in order to have a wavelength free of aberration.

Integrated device using two stigmatic points were also made⁹. Due to the optimization it is the best configuration for integrated diffraction grating devices with small aberration.

5.7 Fresnel-Kirchhoff model

Numerical calculation where carried out using a Fresnel-Kirchhoff method adapted to a bi-dimensional world¹⁰. The implementation was done in a Python script program, and the program is available at Google Code¹¹. The adaptation to bi-dimensional field amplitude will decays as $1/\sqrt{r}$ instead of $1/r$ in the tri-dimensional case.

⁶Beutler, “The theory of the concave grating”; Marz and Cremer, “On the theory of planar spectrographs”; Namioka, “Theory of the Concave Grating. II. Application of the Theory to the Off—Plane Eagle Mounting in a Vacuum Spectrograph”; Velzel, “A general theory of the aberrations of diffraction gratings and gratinglike optical instruments”.

⁷Gabrielli et al., “Silicon nanostructure cloak operating at optical frequencies”.

⁸McGreer, “Theory of concave gratings based on a recursive definition of facet positions”.

⁹Gidon, Jadot, and Valette, “Multiplexer-demultiplexer using an elliptical concave grating and produced in integrated optics”; Horst et al., “Silicon-on-insulator Echelle grating WDM demultiplexers with two stigmatic points”.

¹⁰Brouckaert et al., “Planar concave grating demultiplexer fabricated on a nanophotonic silicon-on-insulator platform”.

¹¹<http://code.google.com/p/khsimulator/>

Figure 5.7.1 shows a sketch of the geometry of the simulated grating. The simulation was carried in two steps. First the field in the grating groove were calculated assuming that the field in the input waveguide had a cosine mode line shape. Then, the field in the output waveguide was calculated using the field on the grating computed in the previous step. The amount of light coupled in to the output waveguide was estimated by carrying the inner product of the field in the output waveguide and the mode supported by that waveguide.

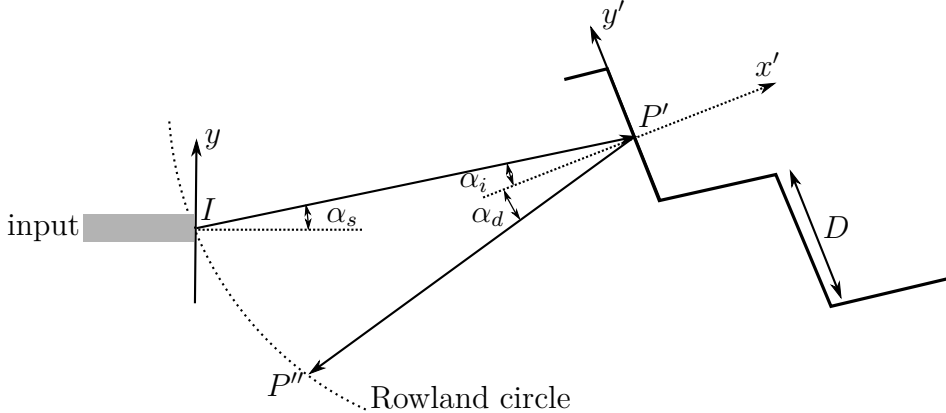


Figure 5.7.1: Sketch of the geometry of the simulated spectrometer.

According to the Fresnel-Kirchhoff diffraction formula, the incident electric field E_{inc} at the center points of the grating facets (P') at a distance r_1 and at an angle α_s can be calculated as

$$E_{\text{inc}} = \frac{1}{2} \sqrt{\frac{n_{\text{eff}}}{\lambda}} \int E_{\text{wg}}(y) \frac{e^{-jkr_1}}{\sqrt{r_1}} (1 - \cos \alpha_s) dy \quad (5.7.1)$$

where $k = 2\pi n_{\text{eff}}/\lambda$ is the wavenumber within the slab waveguide, and E_{wg} is the electric field profile of the TE-polarized fundamental mode of the input waveguide. Similarly, the diffracted field E_{out} on the collection waveguides is calculated as

$$E_{\text{out}}(P'') = \eta \sqrt{\frac{n_{\text{eff}}}{\lambda}} \sum_{\text{Grating}} \int_{-D/2}^{+D/2} E_{\text{inc}}(y) \frac{e^{-jkr_2}}{\sqrt{r_2}} \frac{(\cos \alpha_i - \cos \alpha_d)}{2} dy' \quad (5.7.2)$$

where α_i and α_d are the incident and diffracted angles with respect to the normal of each grating facet, and η is the reflection coefficient of the grating. This formula is simplified if we assume that the magnitude of the incident field $|E_{\text{inc}}|$ is constant over each facet and the phase of this field changes linearly along the length of the facet

$$E_{\text{inc}}(y') = E_{\text{inc}}(y' = 0) e^{+iky' \sin \alpha_i}. \quad (5.7.3)$$

This approximation is valid if the size of the facets is small compared with the distance to

the input and if the angle of incidence α_i is small. This is the case if the blaze point (O) is positioned near the input waveguide (I).

5.8 Numerical simulation of spectral defects and aberrations using Fresnel-Kirchhoff model

Numerical simulations also provides us with a tool to observe the effects of some fabrication limitations, as, for example, the precision to which we can place a grating groove. Two grating conditions were simulated. First we shifted each groove of the waveguide in its facet normal direction by a random value in a range with different amplitudes. Figure 5.8.1 shows the transmission spectrum of a single channel for different amplitudes. Up to a randomness of amplitude 100 nm the signal to noise ration is greater than 20 dB. Since e-beam lithography can deliver a patterning precision better than 100 nm then random errors should not be a problem.

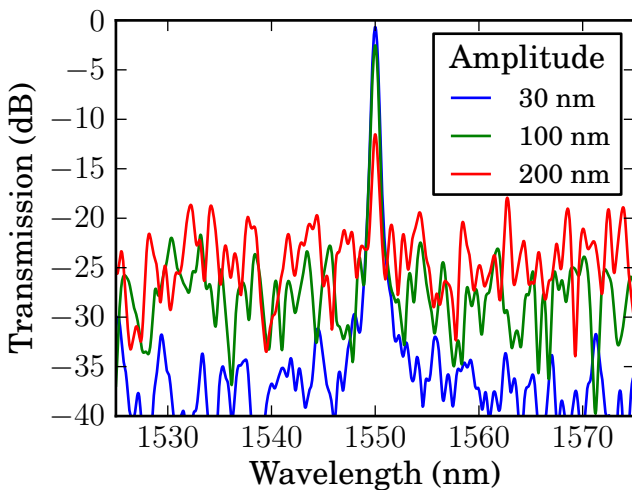


Figure 5.8.1: Transmission spectrum of a single channel of a grating spectrometer with the position of the grating randomly shifted. The range of possible random numbers is the amplitude.

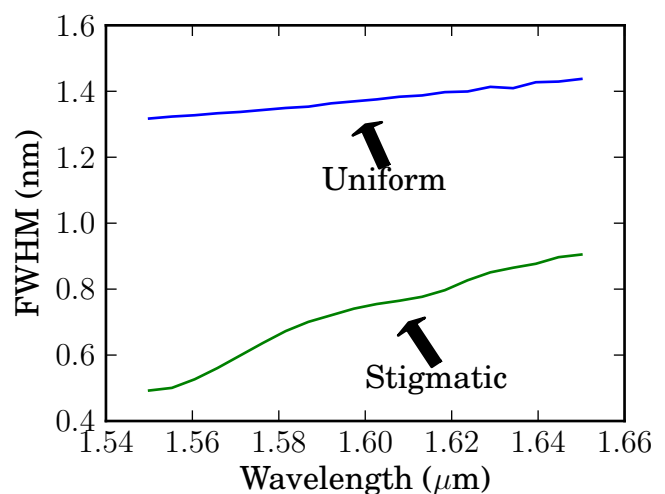


Figure 5.8.2: Beam waist FWHM after focusing a diffracted field on a Rowland mounting.

5.9 Implementation

5.9.1 Design

We have designed a WDM that uses a Rowland configuration with one the stigmatic point correction. The system was designed so that stigmatic point was located at the central waveguide of the 21 output waveguide array. The central wavelength was chosen to be 1500 nm and the diffraction order was 10. The Rowland circle was chosen to be 750 μm . The designed grating contains 340 grooves. The resulting free spectral range was estimated to be 117 nm, and the groove spacing approximately 4 μm . The input and output waveguide apertures were 1.4 μm . A reference waveguide was placed next to the spectrometer so that the transmission efficiency could be estimated. Unfortunately, because the TE and TM mode effective index are governed by different equations (4.2.15 and 4.2.16), the designed device is polarization sensitive. We chose to optimize the device for TE polarization.

Wavelength

Due to the availability of testing equipment operating at 1460-1610 nm range we decided to design the system to operate somewhere at this range. Germanium detectors have a peak detection at 1500 nm so we decided to design the spectrometer operating range centered at 1500 nm.

Grating size

The spectrometer was patterned using a JEOL 9300FS¹² electron beam lithographer. The system is capable of writing using only beam deflection on an area (denominated *field size*) of 1x1 mm. By moving the sample to be written (process called as *stitching*) one is capable of writing a whole 5x5 inches mask. Unfortunately due to the extreme precision required, it is difficult to align the borders of neighboring fields perfectly. With the system working its best alignments of 10 nm are possible, though achieving this kind of precision requires a good amount of trials and experience, alignments of 50 nm are more routinely achieved. In order to avoid errors in the spectrometer grating during stitching we limited the size of the grating in order it to fit in a single 1x1 mm field, which meant placing the grating along the diagonal of the field, which, ignoring the grating curvature, gave us a grating size of 1.4 mm.

¹²<http://www.jeol.com/PRODUCTS/SemiconductorEquipment/ElectronBeamLithography/JBX9300FS/tabid/152/Default.aspx>

Input and output waveguides angle

Input and output waveguides angle are defined by the compromise between the rate with which the beam sweeps across the Rowland circle as wavelength change (linear dispersion¹³) and space in the Rowland circle occupied by an output waveguide. From equation 5.9.1 we see that it increases with decreasing input angle, and from equation 5.9.2 the section of the Rowland circle used by the output waveguide (perimeter used) increases with input angle. We found a good compromise with the value of input angle 35.

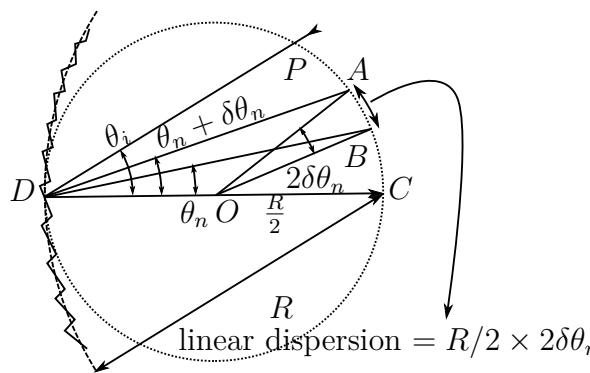


Figure 5.9.1: Linear dispersion schematics.

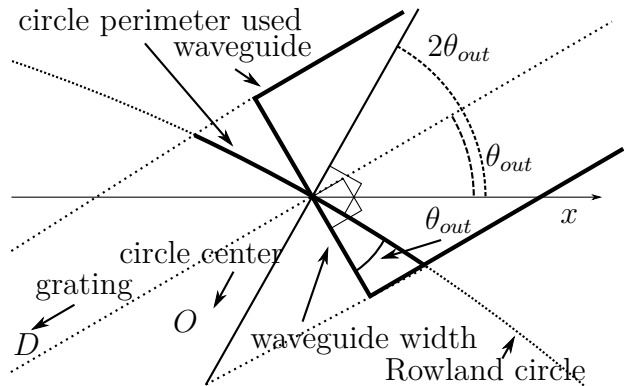


Figure 5.9.2: Rowland circle perimeter used by an output waveguide.

From figure 5.9.1 we see that the linear dispersion is the rate o change of output angle with the input angle $\delta\theta_{\text{out}} = \frac{\partial\theta_{\text{out}}}{\partial\lambda}\delta\lambda$ multiplied by the radius.

$$\text{Linear dispersion} = \frac{R}{2} (2\delta\theta_{\text{out}}) = \frac{Rm\delta\lambda}{a \left[1 + (m\frac{\lambda}{a} + \sin \theta_{\text{in}})^2 \right]}. \quad (5.9.1)$$

As shown in figure 5.9.2 the section of the Rowland circle used by the output waveguide (perimeter used) multiplied by the cosine of the output angle has to be the waveguide width. Using the dependency of the output angle with the input angle

$$\text{perimeter used} = \frac{\text{waveguide width}}{\cos \theta_{\text{out}}} = \frac{\text{waveguide width}}{m\frac{\lambda}{a} + \sin \theta_{\text{in}}} \quad (5.9.2)$$

Number of grooves

The higher the number of grooves the higher resolving power we can get. Therefore we want to maximize the number of grooves. But we alsooo want to limit the grating size, in this particular device to 1.4 mm. Hence a small pitch is necessary to achieve a high number of grooves. Since

¹³Chowdhury and Inc, “Design of low-loss and polarization-insensitive reflectiongrating-based planar demultiplexers”.

diffraction angle increases with decreasing pitch, the number of grooves is effectively limited. By trial and error a reasonable compromise was achieved with 340 grooves.

Number of output waveguides

Theoretically we had space to pattern a hundred output waveguide. But this component was also the one that takes most time during e-beam writing. Due to limitations on the writing time we had to decrease the number of output waveguides to 21.

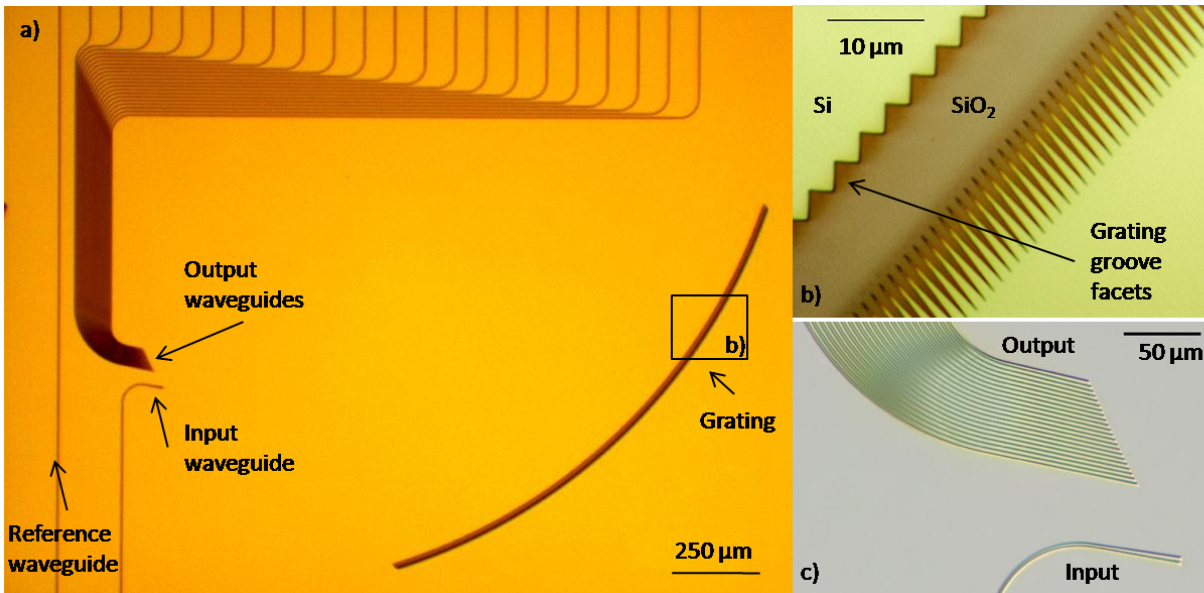


Figure 5.9.3: Microscope photo of the WDM.

5.9.2 Effective index dispersion

As previously discussed, the materials that the waveguide is made of and waveguide itself cause a dispersion of the effective refractive index of the mode. Figures 5.9.4 show the dispersion for TE mode slab waveguides with 200, 250 and 300 nm of thickness with material dispersion was used during calculation. Proper design needs to take into account this dispersion to position the output waveguides.

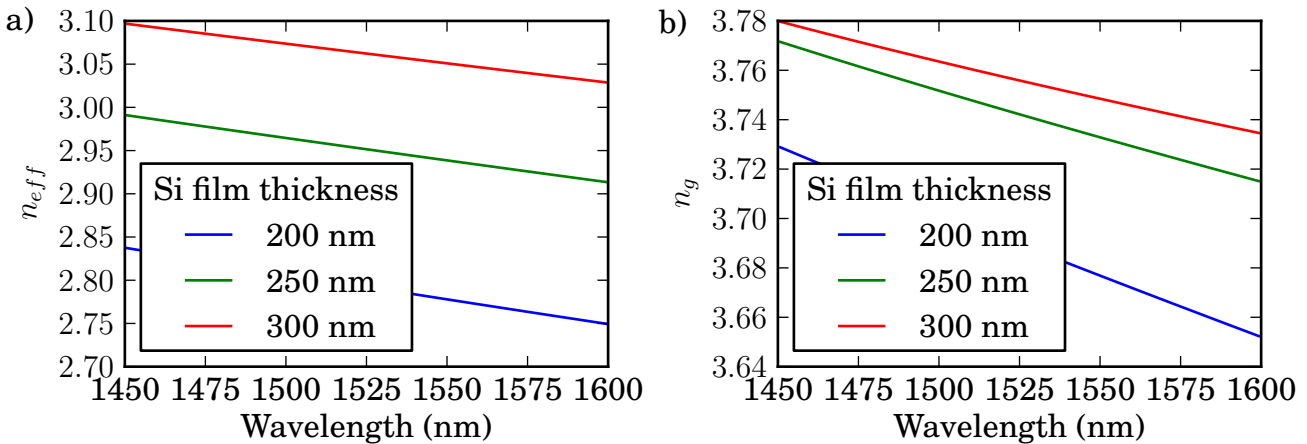


Figure 5.9.4: Effective index (a) and group index (b) dispersion for a Si slab waveguide surrounded by Silica for different slab thicknesses.

5.9.3 Fabrication

The fabrication was done in the Cornell Nanoscale Facility (CNF)¹⁴. A research micro-fabrication laboratory, funded in part by the National Science Foundation (NSF) and by its users. The research facility counts with state of the art electron beam lithography writer.

We fabricated the device using CMOS compatible procedures. First, we start with an SOI wafer with 250 nm silicon and 3 μ m buried oxide. An 80 nm layer of SiO_2 was deposited using plasma enhanced chemical vapor deposition (PECVD) to be used as a hard mask. A 200 nm layer of PMMA was spun and then the grating and the waveguides were defined using e-beam lithography. The pattern was transferred from PMMA to the oxide layer using CHF_3/O_2 reactive ion etch. The silicon layer was etched using Cl_2 inductively coupled plasma and then 2.3 μ m of SiO_2 was deposited using PECVD to clad the device. The wafer was diced and polished for optical testing.

¹⁴<http://www.cnf.cornell.edu>

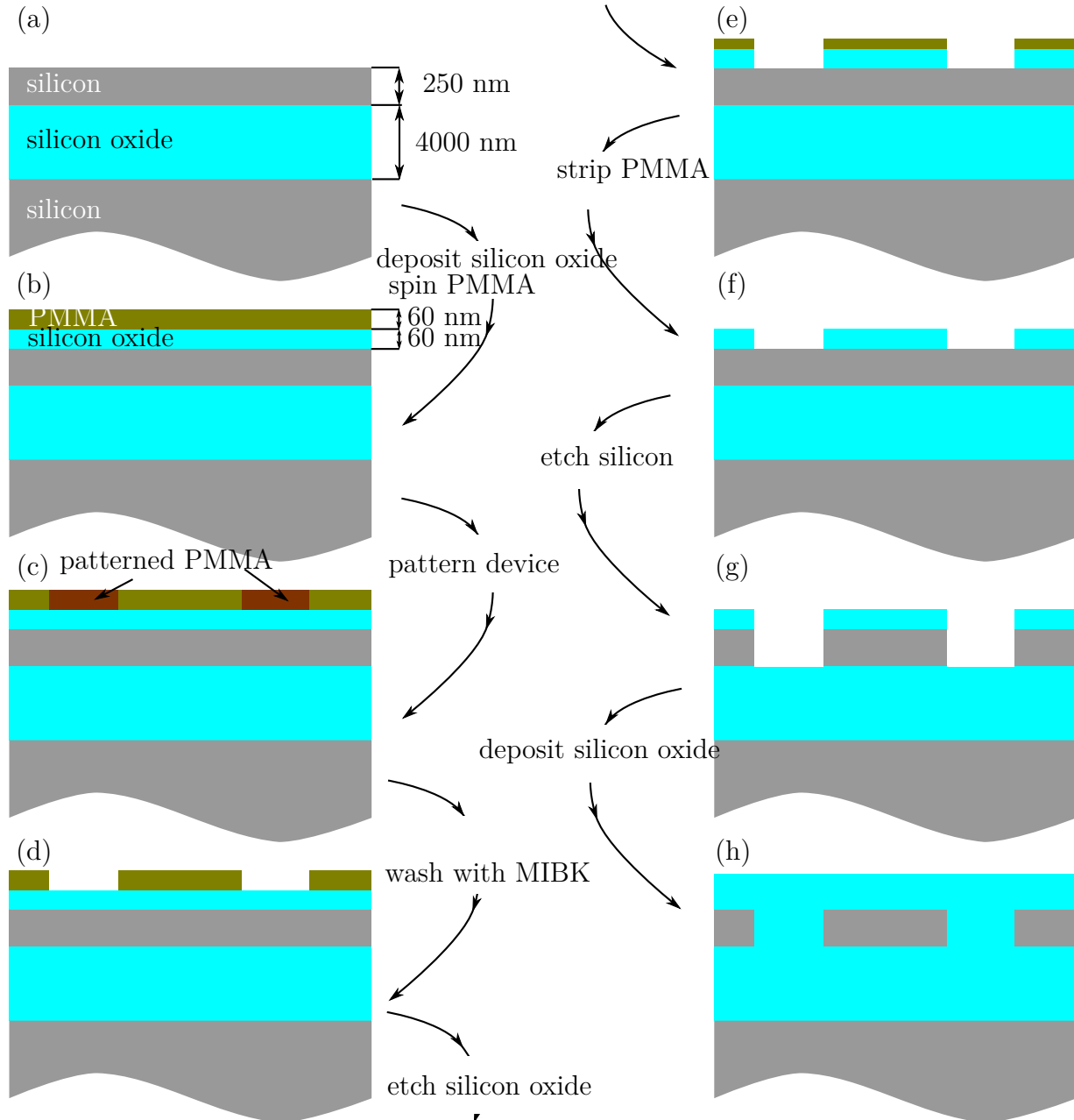


Figure 5.9.5: Fabrication process.

5.9.4 Testing setup

Testing was done by inserting a monochromatic tunable laser light in the device and measure the light power at each of the spectrometer output as the laser sweeps the wavelength.

The laser used was an external cavity laser (Tunics Reference). Light guided in fiber optic was passed through a polarization controller and coupled in the chip waveguide using a lensed fiber, as shown in figures 5.9.6 and 5.9.7. Light at the output waveguide is focused using a focusing lens pass through a polarizer, an iris and is detected. The iris was placed to block the light

of channels neighboring the one is being measured. The lens, polarizer, iris and detector or mounted over a translation stage, figure 5.9.7. The channel to be measured can be selected by translating the detection arrangement.

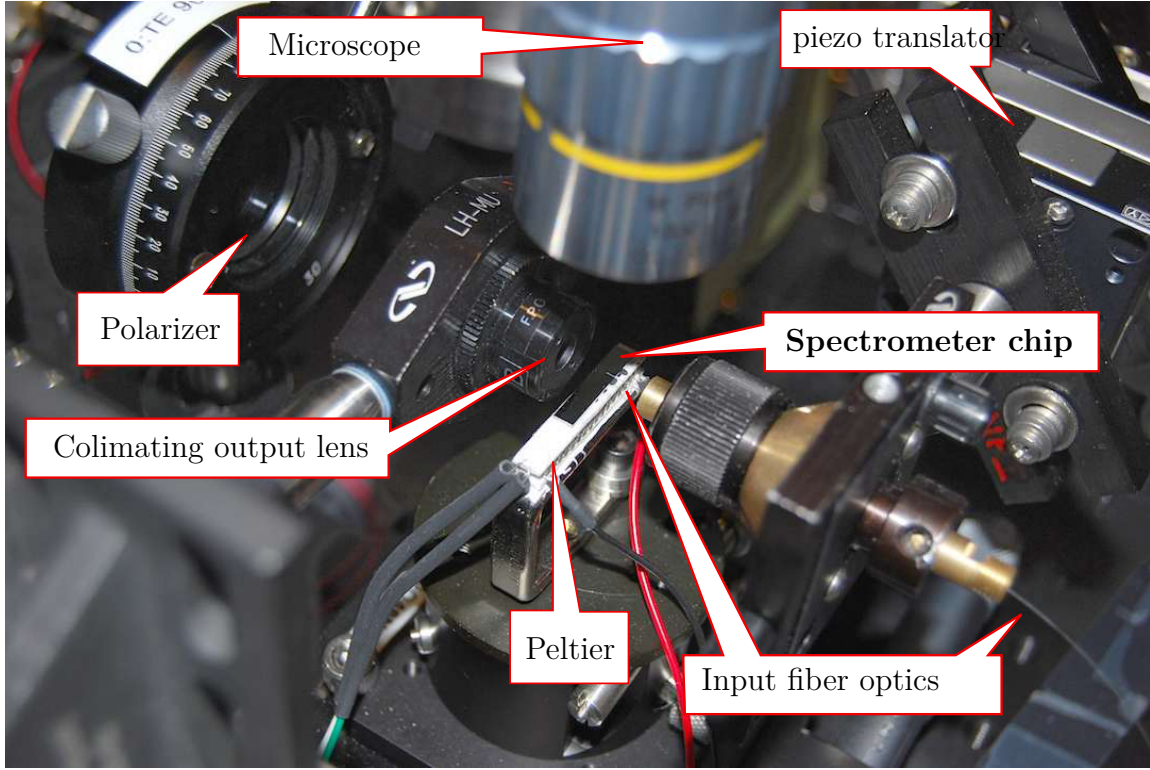


Figure 5.9.6: Experimental setup used to test the on chip spectrometer.

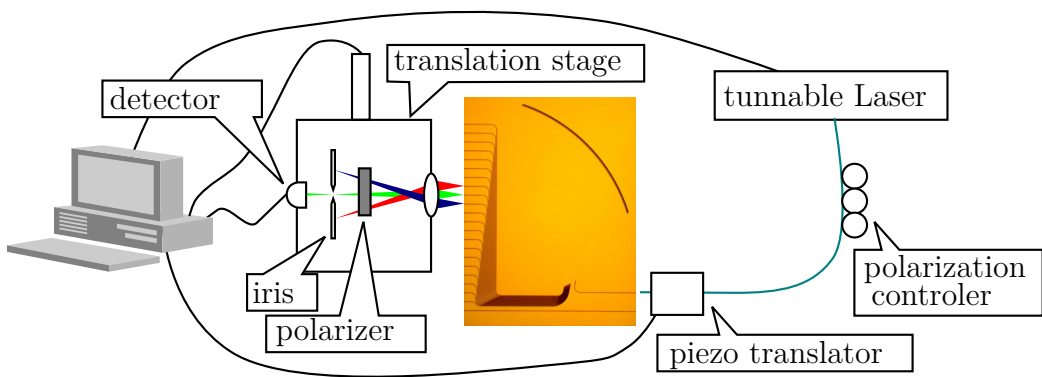


Figure 5.9.7: Schematics of the setup used to test the on chip spectrometer.

5.9.5 Results

The measured performance of our WDM showed -10 dB crosstalk and 1 nm channel spacing across 21 channels. As shown in figure 5.9.8, a relatively flat transmission spectrum was ob-

tained. An insertion loss of -10 dB was estimated by comparing to the transmission through the reference waveguide. This can be attributed to Fresnel reflection between the Si-SiO₂ interfaces at the grating groove facet and can be reduced by coating the grating facets with a reflective metal.

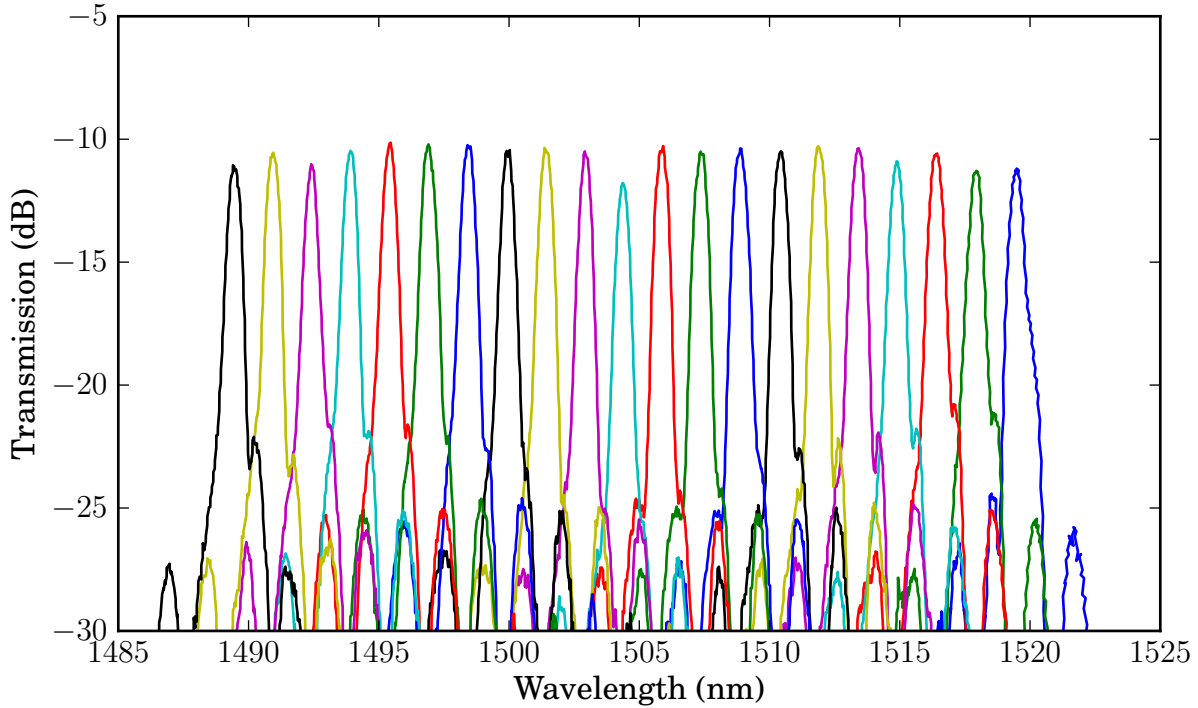


Figure 5.9.8: Transmission spectra of 21 channels of Rowland planar diffraction grating spectrometer.

5.9.6 Conclusion

In conclusion, we demonstrate a one point stigmatic Rowland grating WDM with 21 channels, 1 nm channel spacing and better than -10 dB crosstalk. Since the free spectral range is greater than the 100 nm, by adding additional output waveguides it is possible to construct a WDM that covers the whole C-band (1530 - 1565 nm).

Chapter 6

Ring Enhanced Spectrometer

All for one, and one for all.

Alexandre Dumas

How can we use resonators to make a spectrometer? An array of resonators can be used. But fabrication limits prevent its use without requiring individually tuning each resonator. Grating spectrometers uses a lot of space. Is there a middle way. Yes! we can combine resonators and a diffraction grating spectrometer. The device described in this chapter was published in Optics Express and presented on the Conference of Lasers and Electro-Optics 2010 (CLEO) as an invited paper and received an honorable mention in the Maiman Student Paper Competition in the same conference.

6.1 Device theory

The principle of operation consists of using a resonator to pre-filter the light to be analyzed by a diffraction grating spectrometer. Initially we need a resonator and a spectrometer, figure 6.1.1, with transmission spectrum such that the resonance peaks and the channels peaks coincide, figure 6.1.2. For this to happen, the resonator FSR and the spectrometer channels spacing needs to be equal, and the transmission peak of a spectrometer channel and a resonance peak needs to match. If we have this condition and we connect the resonator output to the spectrometer input, as in figure 6.1.3, the transmission spectrum of the resulting device will be the overlap of the resonator and spectrometer transmission spectrum, figure 6.1.4.

The approach mixes the high quality achievable by resonator with the multitude of channels offered by spectrometer.

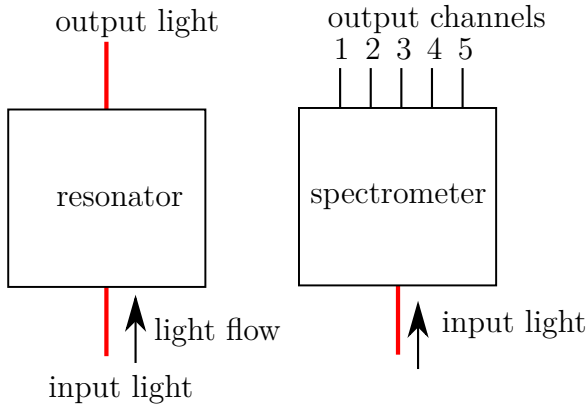


Figure 6.1.1: Block elements for the resonator and spectrometer.

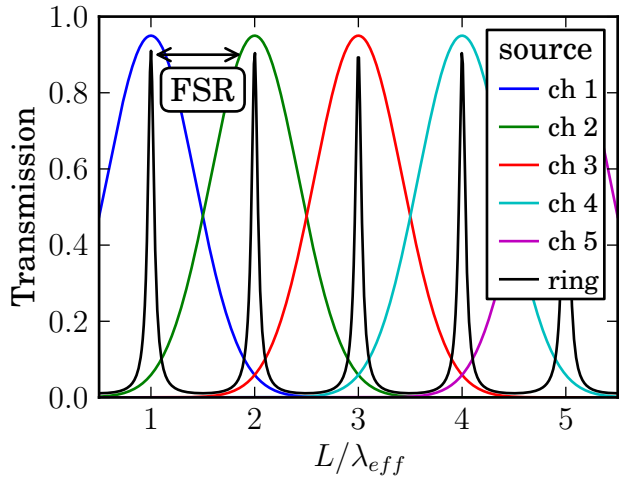


Figure 6.1.2: Transmission spectrum for the resonator and spectrometer on the left.

6.2 Design

Although the described mechanism can be realized with bulk components, as it has already been done¹, making these device using micro-fabrication techniques allow us to add more devices with little cost, which is of advantage when we increase channel density as we will see later.

For a PIC device, we used a ring cavity as the resonator and a diffraction grating spectrometer. As the DG spectrometer the same design as in section 5.9 was used. A ring resonator with a drop port was designed to have 1 nm FSR in order to match the DG spectrometer channel spacing. Metal heaters are added above the silicon layer to align the resonator and spectrometer transmission combs using the thermo-optic effect in silicon. The diffraction grating spectrometer contains 25 channels. To match the ring resonator FSR to the DG spectrometer channel spacing we use an 83.5 μm radius ring with waveguide cross-section of 450 x 250 nm. The FSR changes with wavelength according to $2\lambda/n_gL$, but considering a slight positive group velocity dispersion ($\partial n_g/\partial \lambda \approx 3.6 \times 10^{-3}\text{nm}^{-1}$) this change is extremely small: the total change in FSR across the range of operation (25 nm) is approximately 1% for light polarized in the plane of the device (TE polarization).

6.3 Fabrication

The fabrication of the dielectric part was carried the same way as the DG spectrometer, described in 5.9.3. An alternation was done between layers before cladding the device with PECVD silicon oxide, which was to first cover the device conformally with 160 nm of SiO_2

¹Bajraszewski et al., “Improved spectral optical coherence tomography using optical frequency comb”.

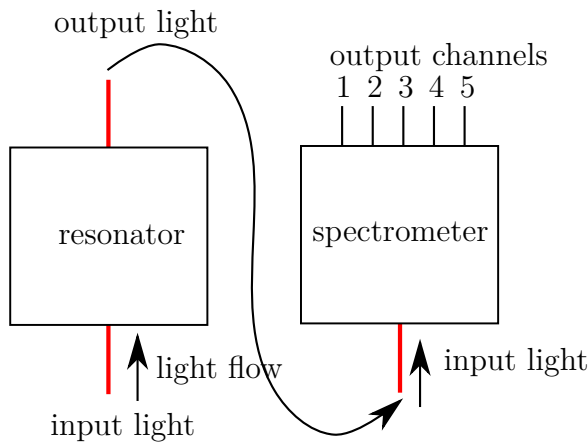


Figure 6.1.3: Output of a resonator filter connected to the input of a spectrometer.

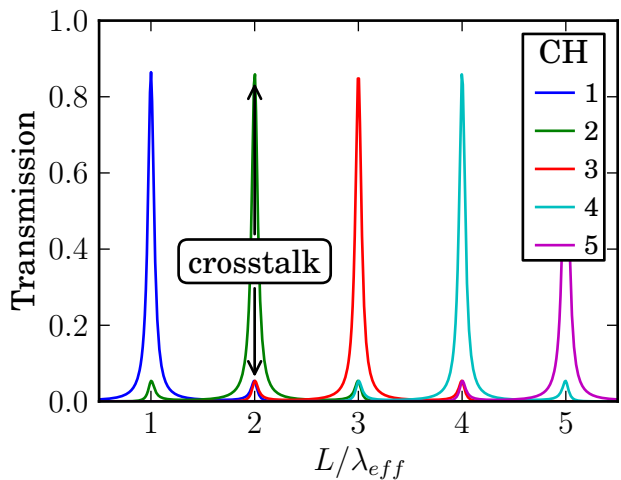


Figure 6.1.4: Transmission spectrum for the resonator connected to a spectrometer as depicted on the left. Small peaks are the overlap of the resonance neighboring the one that match a channel peak and that channel residual transmission at that wavelength.

using a chemical vapor deposition at 1200°C. This was done because SiO₂ deposited using PECVD does not completely fill the gap in the coupling to the ring waveguides. Here we only describe the additional steps to produce the ring heater.

In figure 6.3.1(a) we have the fabricated dielectric part as explained in figure 5.9.5. Over the cladding silica, we spin coat LOR5A (MicroChem) at 3000 RPM for 30 seconds and bake the result for 5 minutes in hot plate heated at 180°C. After letting the device cool down, SPR955CM (MicroChem) is spun coat at 4000 RPM for 30 seconds, and baked for 2 minutes in hot plate at 90°C, 6.3.1(b).

The ring heater pattern is then transferred from a previously patterned mask to the device using contact photolithography. The exposure time was 10 seconds with near-UV radiation (405-365 nm), 6.3.1(c). The mask was patterned using a pattern generator from the designed CAD file. Development was carried by immersing the sample in a solution of MIF300 (AZ Electronic Materials) for 60 seconds, and then rinsed for 20 seconds in de-ionized water, 6.3.1(d). 120 nm of NiCr was evaporated over the sample, 6.3.1(e). In the evaporator the sample was tied to a rotating disc, rotating at 200 RPM for the deposition to be angularly even. The resist together with the NiCr over it were striped leaving the device emerged in a solution of acetone overnight, 6.3.1(f). The device wafer was then diced and the pieces waveguide edges were polished.

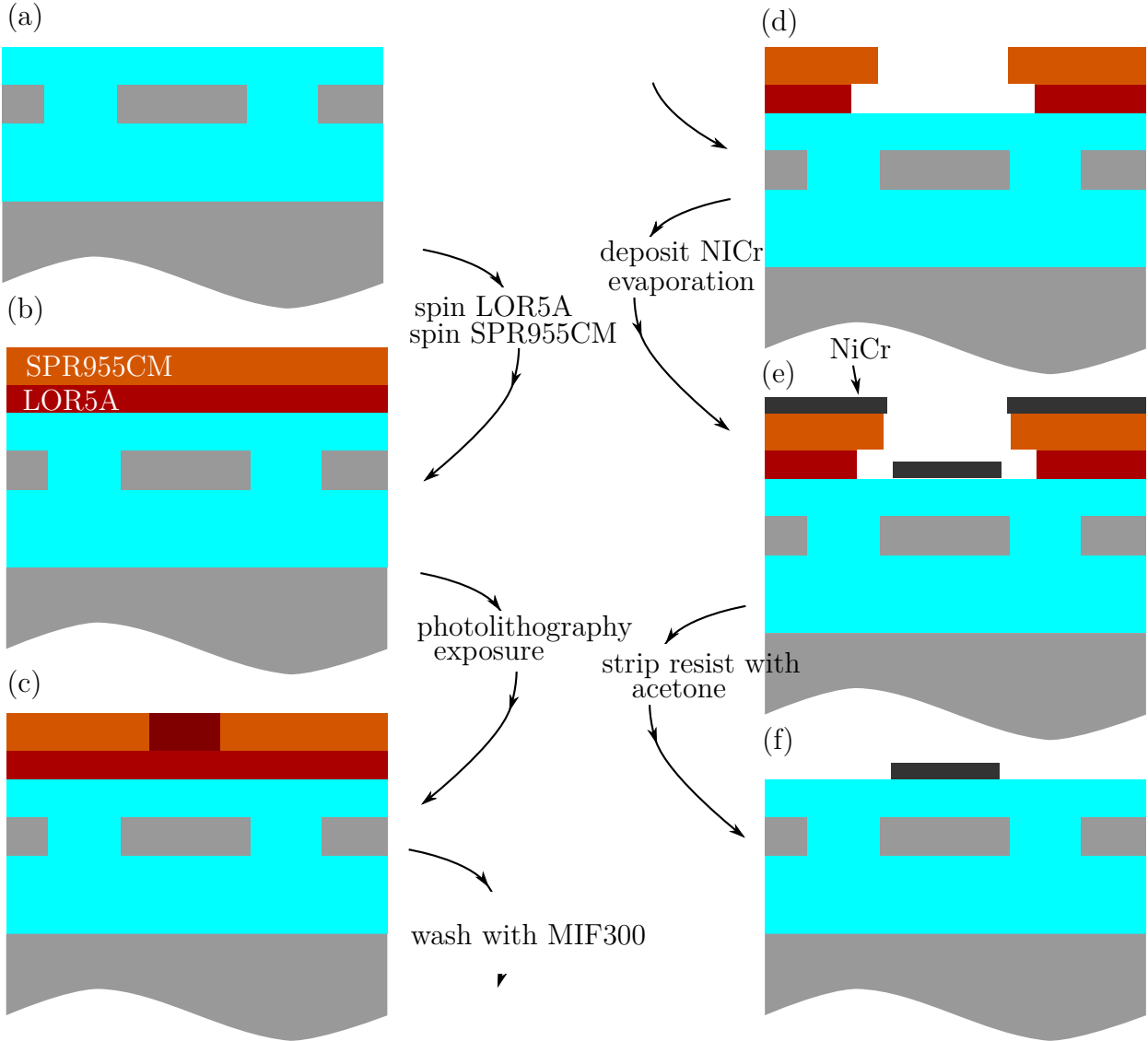


Figure 6.3.1: Ring heater fabrication process.

6.4 Testing setup

A similar setup used to test WDM was employed. In this setup an electrical probe was added to drive current to the ring heater. Although it was not mentioned before, the base the chip rests over is a peltier heater-cooler with a thermocouple mounted on it to measure the temperature. Figure 6.4.1 shows a schematics of the setup.

To test the ring performance, light inserted in input waveguide is measured in the ring through port while the laser is scanned. Graph in figure 6.4.2 shows the through port transmission spectrum. Unfortunately the measured FSR was 0.97 nm, 30 pm lower than the designed. A zoom in the selected resonance shows, figure 6.4.3, shows that the FWHM is 50 pm, corresponding to a quality factor $Q = \lambda/\Delta\lambda = 30000$. We measure the device transmission spectrum by

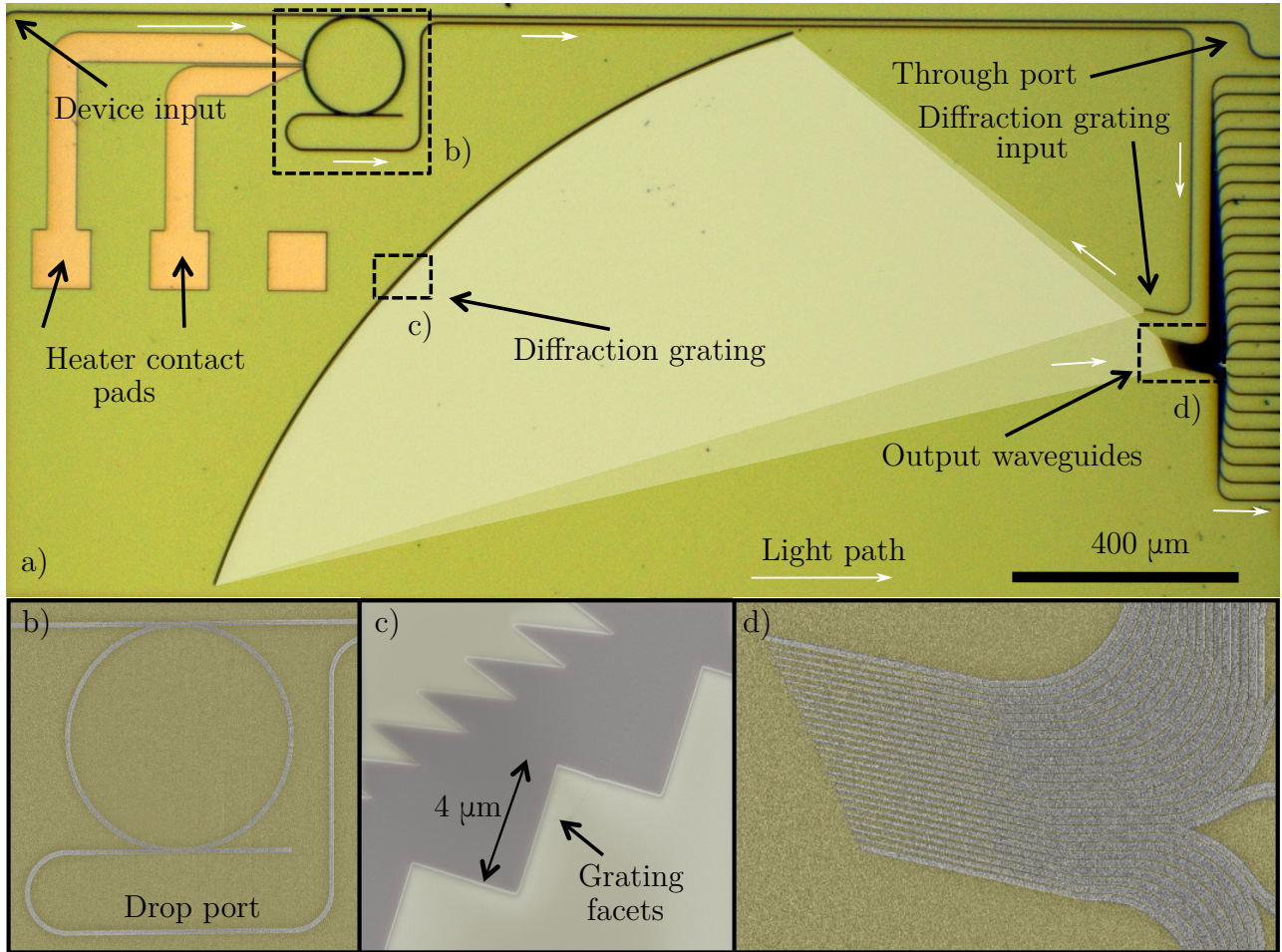


Figure 6.3.2:

coupling laser light from a tunable laser into the input waveguide using a lensed fiber and measuring the transmitted power as a function of wavelength. The input light is TE polarized and the output light is collected using a microscope objective and filtered for the TE polarization before detection. We achieve a channel FWHM of 0.05 nm across 10 different channels of the composed ring and EDG spectrometer, which represents a decrease in the channel width by 10 times compared with the DG spectrometer alone.

Figure 6.4.4 shows the device transmission. The transmission is normalized to the ring through port power level to eliminate coupling losses. The device insertion loss varies between -18 and -23 dB, where -10 dB is due to the Fresnel reflection of the diffraction grating and can be eliminated by coating it with a metal or using Bragg reflectors². Other losses are attributed to stitching in the waveguide definition during e-beam lithography. A small mismatch between the resonator FSR (0.97 nm) and the DG spectrometer channel spacing (1 nm) causes a misalignment between the resonance and the DG spectrometer channel that builds up from one

²Brouckaert et al., "Planar concave grating demultiplexer with high reflective Bragg reflector facets".

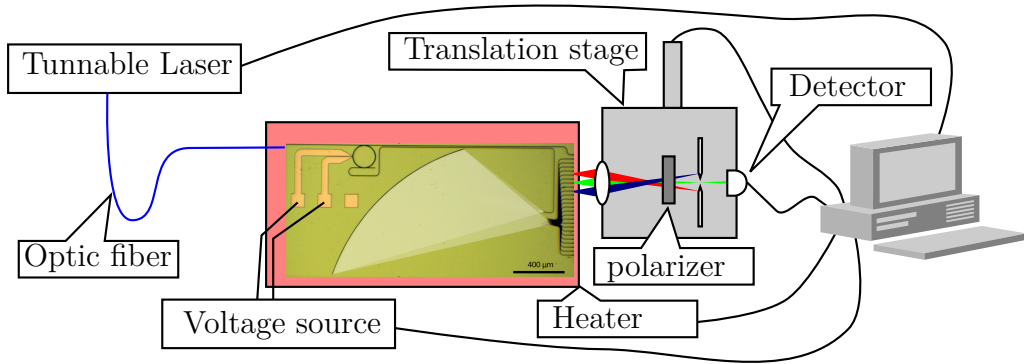


Figure 6.4.1: Schematics of the setup used to test the ring enhanced spectrometer.

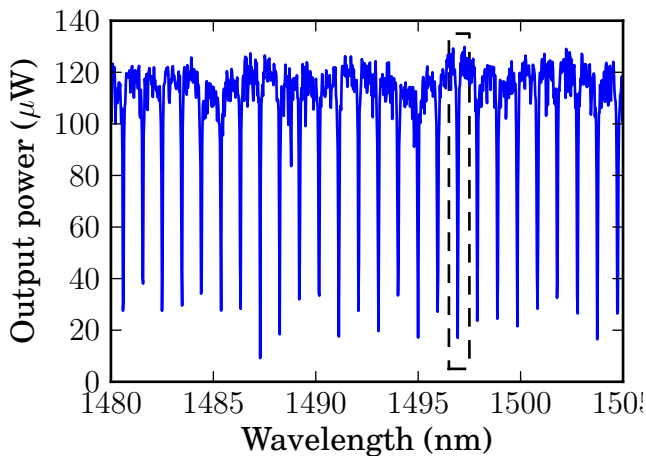


Figure 6.4.2: Output spectrum of the through port of the ring resonator.

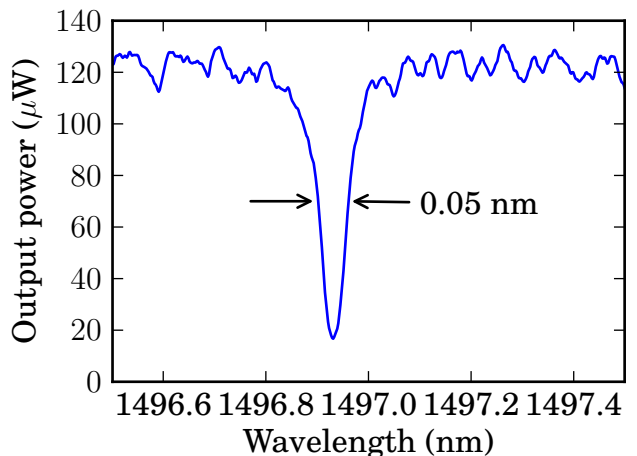


Figure 6.4.3: Zoom in the resonance marked on the left.

channel to the next in a Vernier effect. The outcome is a misalignment between the 11th spectrometer channel and the 11th ring resonance. Therefore only 10 of the 25 channels on the DG spectrometer are used. This issue can be eliminated by more detailed characterization of fabrication.

6.5 Increasing channel density

Channel width was greatly reduced due to the resonator. But the channel density, channels per unity of spectral range, is still equal to the DG spectrometer. Two ways can be readily suggested to increase the channel density. One denoted as space serialization and the other time serialization.

The space serialization approach consists of using multiple combined ring-DG spectrometers, so that the input of a spectrometer is connected to the through port of the previous device,

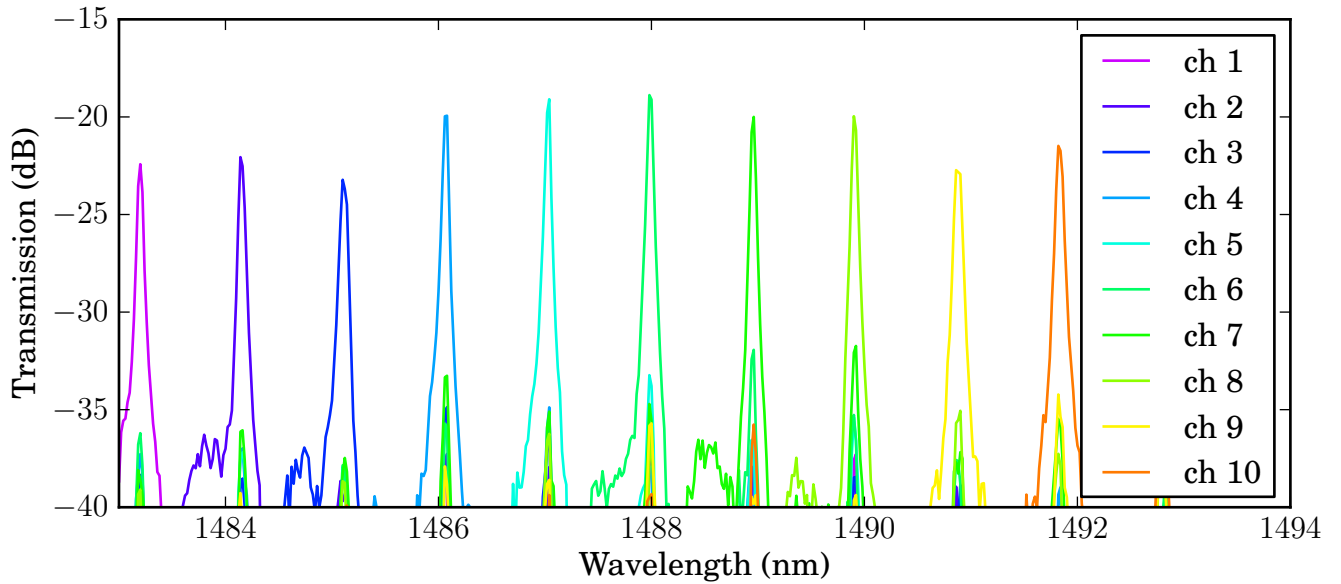


Figure 6.4.4: Transmission spectrum for 10 channels of the ring enhanced spectrometer.

as shown in figure 6.5.1. The peak wavelength of each spectrometer is shifted relative to the others. The number of devices needed in order to achieve the a spectral density where the channels are separated by $\Delta\lambda_{FWHM}$, is equal to the DG spectrometer channel width divided by $\Delta\lambda_{FWHM}$. In spite of the area increase, this approach is still more compact than using a traditional diffraction grating spectrometer since in this proposed approach the area increases linearly with resolution as opposed to quadratic in traditional DGs.

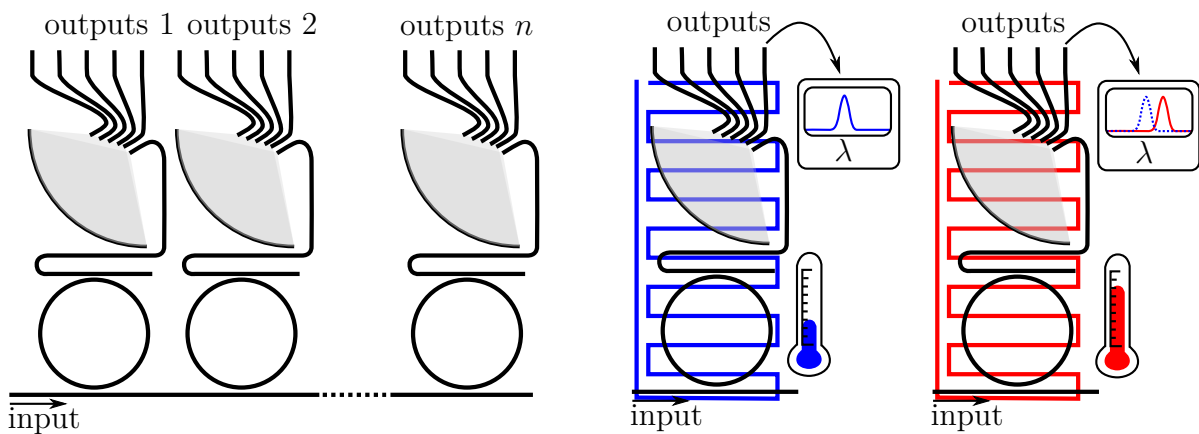


Figure 6.5.1: Multiple RES connected in tandem.

Figure 6.5.2: Single RES at difference temperatures. Transmission spectrum shifts.

In time serialization, figure 6.5.2, only a single combined spectrometer is used and the output spectrum is measured several times. In each measurement the device transmission spectrum is shifted. Notice that this approach also requires active tuning of the ring and the EDG

spectrometer.

6.6 Application of time serialization

We applied the time serialization technique to our device. Thermo-optic effect was used to shift the spectrometer transmission spectrum. Since our FWHM was 50 pm and the channel spacing was 970 pm, we saw that an increment of channel density in 10 times could be done without introducing much crosstalk.

To achieve this, we would have to shift the ring resonances and EDG spectrometer channels by 97 pm. Watching a resonance of valley on the through port as we changed as the temperature, figure 6.6.1 were changed we measured the rate of change of the resonance wavelength shift with temperature as being 79 pm/K, figure 6.6.2. Resonance wavelength shift with ring heater driving power was also measured. It is checked whether the coefficient would change with the overall sample temperature. Although in principle this should happen, there was not an appreciable change in the range of temperature we driven the device.

Figure 6.7.2 shows a density plot where each horizontal line corresponds to the transmission spectrum of each channel. Notice that the overlap of the residual transmission from the DG spectrometer with the neighboring resonances can be seen in the side diagonal lines, and their transmissions are at least 10 dB lower than the peak (main diagonal line).

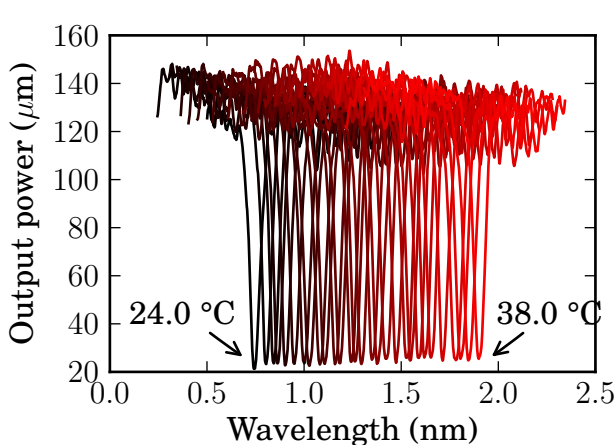


Figure 6.6.1: Through port output power as a temperature increase.

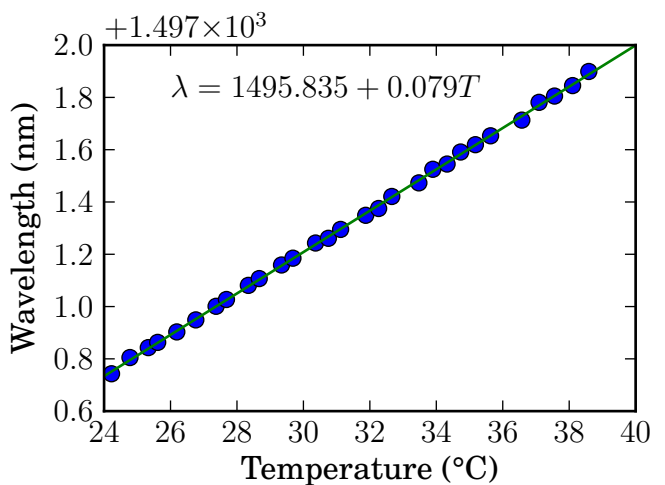


Figure 6.6.2: Resonance wavelengths as temperature increases and fitted linear function.

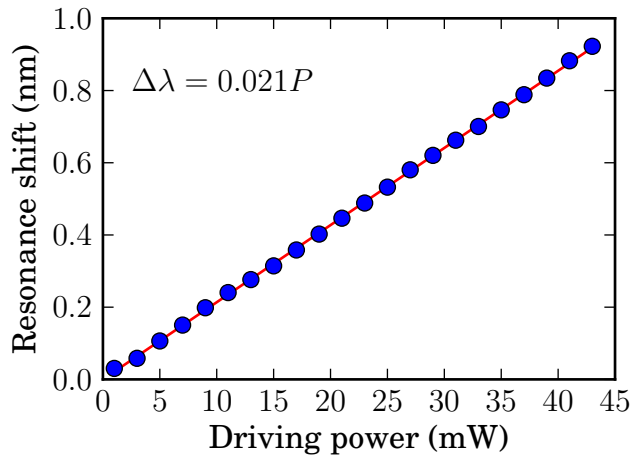


Figure 6.6.3: Resonance wavelength shift for the ring driven by different powers. Ring resistance is $2.2\text{ k}\Omega$.

6.7 Results

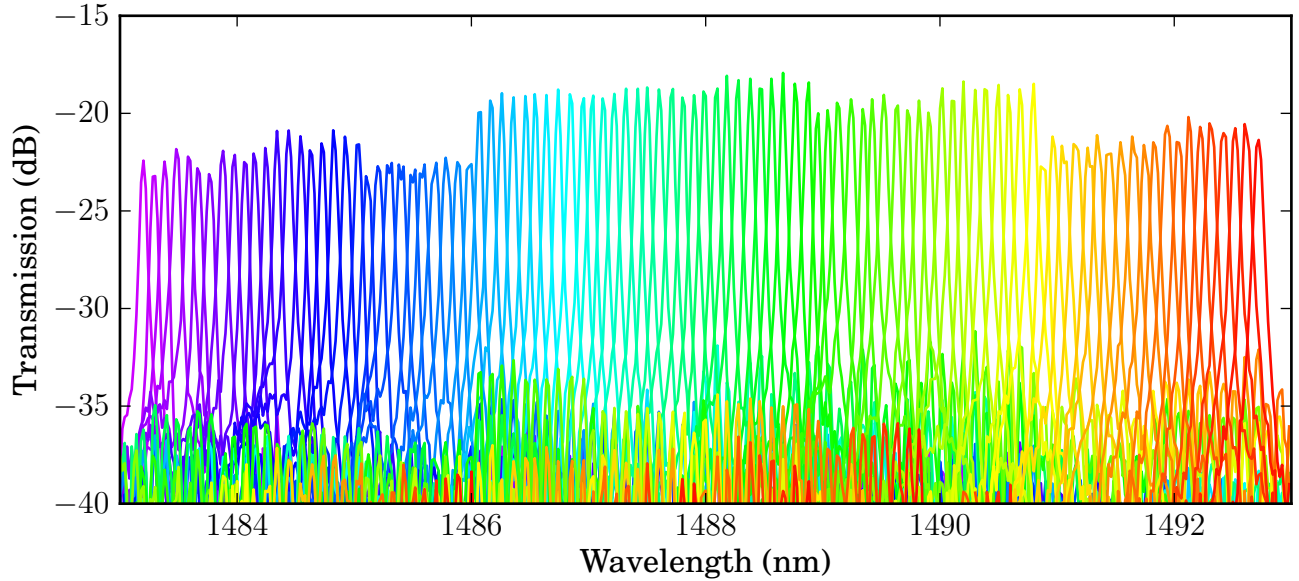


Figure 6.7.1: Transmission spectrum for a combined ring and diffraction spectrometer using a time serialization technique for reducing channel spacing.

Figure 6.7.1 shows the transmission spectrum for the ring enhanced spectrometer for a set of 10 different temperature. We start with a configuration of chip temperature and ring heater driven power such that the DG comb and the ring resonances are aligned, the temperature of the chip is then raised in steps such that the transmission spectrum shifts by 97 pm.

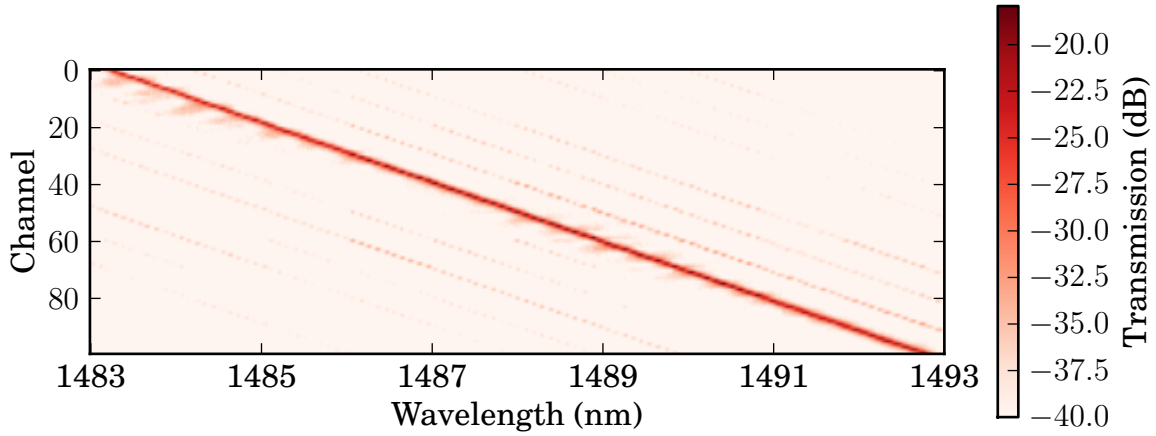


Figure 6.7.2: Density plot of the transmission spectrum for a combined ring and diffraction spectrometer using a time serialization technique, where each horizontal line refers to a channel of the spectrometer.

6.8 Device comparison

Reference	Diagonal (mm)	Resolution (nm)	FSR (nm)	Crosstalk (dB)	Diagonal × Resolution
Brouckaert ¹	0.3	20	150	-30	6
Cheben ²	11	0.2	10	-10	2.2
Horst ³	0.3	3.2	75	-19	0.9
Current work ⁴	1.4	0.1	115	-8	0.14

Table 6.1: Comparison of integrated spectrometer features.

¹ Brouckaert et al., “Planar concave grating demultiplexer fabricated on a nanophotonic silicon-on-insulator platform”

² Cheben et al., “A high-resolution silicon-on-insulator arrayed waveguide grating microspectrometer with sub-micrometer aperture waveguides”

³ Horst et al., “Silicon-on-insulator Echelle grating WDM demultiplexers with two stigmatic points”

⁴ Kyotoku, Chen, and Lipson, “Sub-nm resolution cavity enhanced microspectrometer”

6.9 About the DG spectrometer channels spacing and resonator FSR mismatch

As mentioned, the mismatch between the DG spectrometer channel spacing and the resonator FSR caused a misalignment of the corresponding peaks that limited the useful set of spectrometer channels. It is interesting, therefore, to investigate how this interferes in production of ring enhanced spectrometer (RES).

The best alignment of the DG spectrometer channels and the resonance comb is achieved when the middle channel peak is matched with a resonance. In this configuration, the peak wavelength mismatch of the channel and resonance is going to be

$$\Delta\lambda_{\text{mismatch}} = (\Delta\lambda_{\text{CS}} - \Delta\lambda_{\text{FSR}}) \frac{N}{2}, \quad (6.9.1)$$

where $\Delta\lambda_{\text{CS}}$ is the DG spectrometer channel spacing, $\Delta\lambda_{\text{FSR}}$ is the resonator free spectral range, and N is the number of spectrometer channels. Ideally we want a zero mismatch, but assuming that mismatch smaller than τ can be tolerated, we conclude that the tolerable relative channel spacing and resonator FSR error τ_{error} must be

$$\tau_{\text{error}} = \frac{\Delta\lambda_{\text{CS}} - \Delta\lambda_{\text{FSR}}}{\Delta\lambda_{\text{FSR}}} \leq \frac{2\tau}{N\Delta\lambda_{\text{FSR}}}. \quad (6.9.2)$$

Supposing a tolerance equal half of the DG spectrometer channel FWHM for device with 100 channels and 1 nm channel spacing, a tolerable error of 1% between the channel spacing and resonator FSR is reached. To evaluate this result it is necessary to understand to what precision can we fabricate a device with determined FSR or channel spacing.

6.10 Conclusion

We showed that by using an optical micro ring cavity combined with a diffraction grating spectrometer it is possible to decrease the final device channel width while preserving small footprint. This is because the channel width of the combined device is decoupled from the number of grooves of the diffraction grating. Using time serialization, a device with channel spacing of 0.1 nm, 100 channels, -10 dB crosstalk was demonstrated in a 2x1 mm². To the best of our knowledge this is the highest number of channels and smallest channel spacing for a device of the reported size. While the idea was implemented in a silicon based material which is suitable for IR spectroscopy, the concept can be extended to other wavelength regimes such as the visible range by employing other material platform such as SiN for the realization of the resonator and the grating.

Bibliography

- [1] N. Attar et al. “Micoleakage of class V cavities with different adhesive systems prepared by a diamond instrument and different parameters of Er:YAG laser irradiation”. eng. In: *Photomed. Laser Surg.* 26.6 (2008), pp. 585–91.
- [2] T Bajraszewski et al. “Improved spectral optical coherence tomography using optical frequency comb”. In: *Opt. Express* 16.6 (2008), pp. 4163–4176.
- [3] H. Beutler. “The theory of the concave grating”. In: *J. Opt. Soc. Am.* 35.5 (1945), pp. 311–350.
- [4] M Braem, P Lambrechts, and G Vanherle. “Clinical relevance of laboratory fatigue studies”. eng. In: *J. Dent.* 22.2 (1994), pp. 97–102.
- [5] R Brandenburg, B Haller, and C Hauger. “Real-time in vivo imaging of dental tissue by means of optical coherence tomography (OCT)”. In: *Opt. Commun.* (2003).
- [6] A. K. S. Braz et al. “Evaluation of crack propagation in dental composites by optical coherence tomography”. eng. In: *Dent. Mater.* 25.1 (2009), pp. 74–9.
- [7] J Brouckaert et al. “Planar concave grating demultiplexer fabricated on a nanophotonic silicon-on-insulator platform”. In: *J. Lightwave Tech.* 25.5 (2007), pp. 1269–1275.
- [8] J Brouckaert et al. “Planar concave grating demultiplexer with high reflective Bragg reflector facets”. In: *IEEE Photon. Technol. Lett.* 20.4 (2008), p. 309.
- [9] F. J. Burke et al. “Influence of patient factors on age of restorations at failure and reasons for their placement and replacement”. eng. In: *J. Dent.* 29.5 (2001), pp. 317–24.
- [10] B. Cense et al. “Ultrahigh-resolution high-speed retinal imaging using spectral-domain optical coherence tomography”. In: *Opt. Express* (2004).
- [11] P. Cheben et al. “A high-resolution silicon-on-insulator arrayed waveguide grating microspectrometer with sub-micrometer aperture waveguides”. In: *Opt. Express* 15.5 (2007), pp. 2299–2306.
- [12] L.-P. Choo-Smith et al. “Shedding new light on early caries detection”. eng. In: *J. Can. Dent. Assoc.* 74.10 (2008), pp. 913–8.

- [13] D Chowdhury and C Inc. “Design of low-loss and polarization-insensitive reflectiongrating-based planar demultiplexers”. In: *IEEE J. Sel. Top. Quant.* 6.2 (2000), pp. 233–239.
- [14] G Cocorullo and I Rendina. “Thermo-optical modulation at 1.5 μm in silicon etalon”. In: *Electron. Lett* 28.1 (1992), pp. 83–85.
- [15] B. W. Colston et al. “Imaging of hard-and soft-tissue structure in the oral cavity by optical coherence tomography”. In: *Appl. Opt.* 37.16 (1998), pp. 3582–3585.
- [16] R. A. Danforth. “Cone beam volume tomography: a new digital imaging option for dentistry”. eng. In: *J Calif Dent Assoc* 31.11 (2003), pp. 814–5.
- [17] W. Drexler. “Ultrahigh-resolution optical coherence tomography”. In: *J. Biomed. Opt.* 9 (2004), p. 47.
- [18] A. F Fercher et al. “Measurement of intraocular distances by backscattering spectral interferometry”. In: *Opt. Commun.* 117.1-2 (1995), pp. 43–48.
- [19] D. Fonseca et al. “In vitro imaging of remaining dentin and pulp chamber by optical coherence tomography: comparison between 850 and 1280 nm”. In: *J. Biomed. Opt.* 14 (2009), p. 024009.
- [20] M. Foster et al. “Silicon-chip-based ultrafast optical oscilloscope”. In: *Nature* 456.7218 (2008), pp. 81–84.
- [21] A. Freitas et al. “Imaging carious human dental tissue with optical coherence tomography”. In: *J. Appl. Phys.* 99.2 (2009), p. 024906.
- [22] L. H. Gabrielli et al. “Silicon nanostructure cloak operating at optical frequencies”. In: *Nat. Photonics* 3.8 (2009), pp. 461–463.
- [23] S. K. Garoushi, L. V. J. Lassila, and P. K. Vallittu. “Fatigue strength of fragmented incisal edges restored with a fiber reinforced restorative material”. eng. In: *J. Contemp. Dent. Pract.* 8.2 (2007), pp. 9–16.
- [24] P Gidon, J. Jadot, and S Valette. “Multiplexer-demultiplexer using an elliptical concave grating and produced in integrated optics”. In: *US Patent 4,786,133* (1988).
- [25] J Goodman. *Statistical Optics*. 1985.
- [26] E Götzinger et al. “High speed full range complex spectral domain optical coherence tomography”. In: *Opt. Express* 13.2 (2005), pp. 583–594.
- [27] C Hanks et al. “Cytotoxicity of dental composites and other materials in a new in vitro device”. In: *J. Oral Pathol.* (1988).
- [28] F Horst et al. “Silicon-on-insulator Echelle grating WDM demultiplexers with two stigmatic points”. In: *IEEE Photon. Technol. Lett.* 21.23 (2009), pp. 1743–1745.

- [29] I Hsu et al. “Optical coherence tomography using nonlinear optics in fiber for broadband source generation”. In: *Opt. Commun.* 212 (2002), pp. 391–396.
- [30] C Kauffman et al. “Characterization of the dental pulp using optical coherence tomography”. In: *Proc. IEEE* (2006).
- [31] B. B. C. Kyotoku, L. Chen, and M. Lipson. “Sub-nm resolution cavity enhanced microspectrometer”. In: *Opt. Express* 18 (2010), pp. 102–107.
- [32] B. B. C. Kyotoku et al. “Fiber-reinforced composite analysis using optical coherence tomography after mechanical and thermal cycling”. In: *Proc. SPIE* 6425 (2007), 64250B.
- [33] L. V. J. Lassila et al. “Flexural properties of fiber reinforced root canal posts”. eng. In: *Dent. Mater.* 20.1 (2004), pp. 29–36.
- [34] R. A. Leitgeb, C. K Hitzenberger, and A. F Fercher. “Performance of fourier domain vs. time domain optical coherence tomography”. In: *Opt. Express* 11.8 (2003), pp. 889–894.
- [35] R. A. Leitgeb et al. “Phase-shifting algorithm to achieve high-speed long-depth-range probing by frequency-domain optical coherence tomography”. In: *Opt. Lett.* 28.22 (2003), pp. 2201–2203.
- [36] B. Little et al. “Microring resonator channel dropping filters”. In: *J. Lightwave Tech.* 15.6 (1997), pp. 998–1005.
- [37] G. M. Loughran, A. Versluis, and W. H. Douglas. “Evaluation of sub-critical fatigue crack propagation in a restorative composite”. eng. In: *Dent. Mater.* 21.3 (2005), pp. 252–61.
- [38] E Marcatili. “Dielectric rectangular waveguide and directional coupler for integrated optics”. In: *Bell Syst. Tech. J.* (1969).
- [39] R Marz and C Cremer. “On the theory of planar spectrographs”. In: *J. Lightwave Tech.* 10.12 (1992), pp. 2017–2022.
- [40] K. McGreer. “Theory of concave gratings based on a recursive definition of facet positions”. In: *Appl. Opt.* 35.30 (1996), pp. 5904–5910.
- [41] J. J. Mecholsky. “Fractography: determining the sites of fracture initiation”. eng. In: *Dent. Mater.* 11.2 (1995), pp. 113–6.
- [42] L. D. Melo et al. “Evaluation of enamel dental restoration interface by optical coherence tomography”. In: *J. Biomed. Opt.* 10.064027 (2005).
- [43] I Mjör. *Pulp-dentin biology in restorative dentistry*. 2002.
- [44] T Namioka. “Theory of the Concave Grating. II. Application of the Theory to the Off—Plane Eagle Mounting in a Vacuum Spectrograph”. In: *J. Opt. Soc. Am.* 49.5 (1959), pp. 460–465.

- [45] L. I. Rantala et al. “Fatigue resistance of removable orthodontic appliance reinforced with glass fibre weave”. eng. In: *J. Oral Rehabil.* 30.5 (2003), pp. 501–6.
- [46] A Rollins et al. “In vivo video rate optical coherence tomography”. In: *Opt. Express* 3.6 (1998), pp. 219–229.
- [47] H. Rowland. “On concave gratings for optical purposes”. In: *Philos. Mag.* 16.99 (1883), pp. 197–210.
- [48] K. J. Söderholm and M. J. Roberts. “Influence of water exposure on the tensile strength of composites”. eng. In: *J. Dent. Res.* 69.12 (1990), pp. 1812–6.
- [49] H. Takahashi et al. “Arrayed-waveguide grating for wavelength division multi/demultiplexer with nanometre resolution”. In: *Electron. Lett.* 26.2 (1990), pp. 87–88.
- [50] W. Tropf, T. Harris, and M. Thomas. “Optical Materials: Visible and Infrared”. In: *McGraw-Hill* (1994).
- [51] C. Velzel. “A general theory of the aberrations of diffraction gratings and gratinglike optical instruments”. In: *J. Opt. Soc. Am.* 66.4 (1976), pp. 346–353.
- [52] A Vorckel et al. “Asymmetrically coupled silicon-on-insulator microring resonators for compact add-drop multiplexers”. In: *IEEE Photon. Technol. Lett.* 15.7 (2003), pp. 921–923.
- [53] S White and M. Pharoah. “Oral radiology: principles and interpretation”. In: *lavoisier.fr* (2000).

Appendix A

Huygens-Fresnel Diffraction

A.1 Numerical calculation

On computing Helmholtz and Kirchhoff integral theorem 5.1.5 numerically, a few optimization can be made. The following optimization is particularly useful when the calculation needs to be taken over many elements. To make it more clear, consider the arrangement in figure A.1.1. We have a light source at point S and two obstacles that have apertures \mathbb{Q} and \mathbb{P} , and we

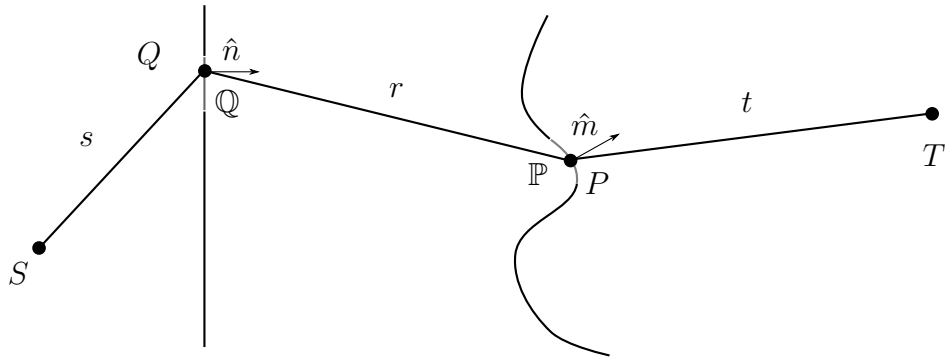


Figure A.1.1:

want to evaluate the electric field at T . Using the integral theorem, this would be a three step operation. First we would compute the field at \mathbb{Q} from S , then compute field at \mathbb{P} from field at \mathbb{Q} , to then finally calculate the field at T from the field at \mathbb{P} . From the integral theorem we see that at each point P we need to compute the field $U(P)$ and derivative of the field in the direction of normal \hat{m} of aperture defining plane \mathbb{P} , $\frac{\partial U(P)}{\partial \hat{m}}$. By analytically carrying the derivative of U in respect of \hat{m} , numerical derivative is avoided which would introduce round-off

error¹ and processing cost. The resulting pair of equations will then be.

$$U(P) = \int_{\mathbb{Q}} \frac{e^{ikr}}{\sqrt{kr}} \left[\frac{ikU(Q)}{2} \cos(r, n) - \frac{\partial U(Q)}{\partial n} \right] dS \quad (\text{A.1.1})$$

$$\frac{\partial U(P)}{\partial m} = \frac{ik}{2} \int_{\mathbb{Q}} \frac{e^{ikr}}{\sqrt{kr}} \left[U(Q) \frac{ik}{2} \cos(r, n) - \frac{\partial U(Q)}{\partial n} \right] \cos(r, m) dS \quad (\text{A.1.2})$$

We, then, can use the above set of equations to iteratively compute the electric field at points Q , P and T .

A.2 Small aperture approximation

If the aperture \mathbb{Q} is much smaller than r , then we can consider that $\cos(r, m)$ does not vary a lot in the integral, therefore we can pull it outside the integral, which convert the integral to $U(P)$. We therefore can simplify the equations to

$$\begin{cases} U(P) = \int_{\mathbb{Q}} \frac{e^{ikr}}{\sqrt{kr}} \left[\frac{ikU(Q)}{2} \cos(r, n) - \frac{\partial U(Q)}{\partial n} \right] dS \\ \frac{\partial U(P)}{\partial m} = \frac{ik}{2} \cos(r, m) U(P) \end{cases} \quad (\text{A.2.1})$$

$$\frac{\partial U(P)}{\partial m} = \frac{ik}{2} \cos(r, m) \int_{\mathbb{Q}} \frac{e^{ikr}}{\sqrt{kr}} \left[U(Q) \frac{ik}{2} \cos(r, n) - \frac{\partial U(Q)}{\partial n} \right] dS = \frac{ik}{2} \cos(r, m) U(P) \quad (\text{A.2.2})$$

A.3 Numerical program validation

To validate the program, we simulated a geometry that could also be solved analytically. Figure shows the chosen geometry. It consists of a circular screen with radius R , and a source field concentric with the screen consisting of a uniform field E over a line segment with length W . Analytically the first approximation off equation, to the chosen geometry will be equal to

$$E_{\text{circle}} = \sqrt{\frac{\pi}{2}} W E e^{-ikR} \sqrt{\frac{k}{R}} (\cos(\alpha) + 1) \text{sinc}\left(\frac{kW \sin(\alpha)}{2\pi}\right) \quad (\text{A.3.1})$$

where k is the wavenumber. For $R = 2\text{mm}$, $k = 1.24 \times 10^5 \text{cm}^{-1}$ and $W = 3\mu\text{m}$, the simulation (circle markers) and analytic function (continuous line) are plotted in figure X.

¹http://en.wikipedia.org/wiki/Rounding_error

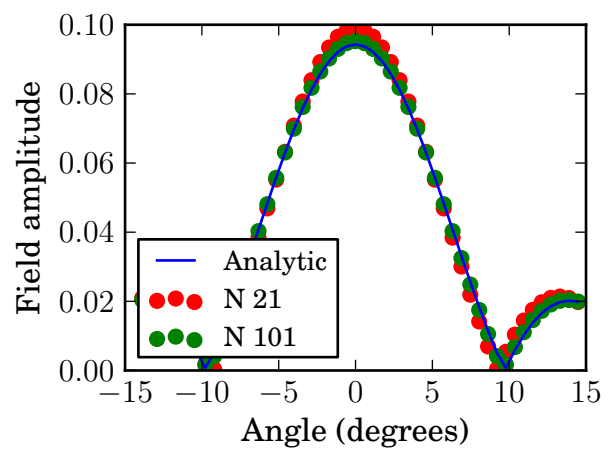
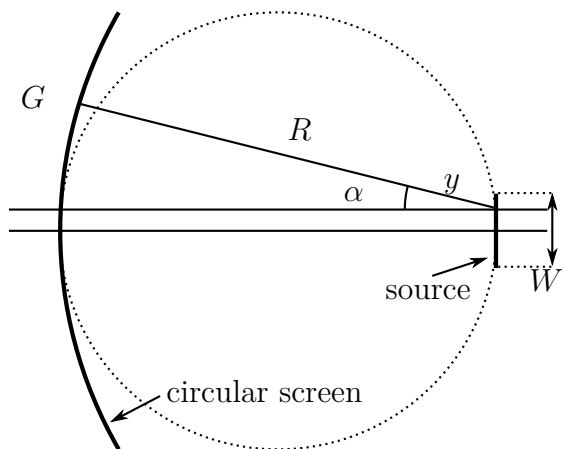


Figure A.3.1: (a) Schematic of the geometry used to validate simulation program against the analytic solution. (b) Electric field in the circle screen in (a) versus the angle α .

Appendix B

Fourier transform

B.1 Relation

$$\sum_{n=-\infty}^{\infty} f(n) e^{ikn} = \sum_{m=-\infty}^{\infty} \hat{f}\left(\frac{k}{2\pi} - m\right) \quad (\text{B.1.1})$$

Using Dirac delta integral

$$\sum_{n=-\infty}^{\infty} f(n) e^{ikn} = \sum_{n=-\infty}^{\infty} \int_{-\infty}^{\infty} \delta(x-n) f(x) e^{ikx} dx,$$

which can be reordered to

$$\sum_{n=-\infty}^{\infty} f(n) e^{ikn} = \int_{-\infty}^{\infty} f(x) \sum_{n=-\infty}^{\infty} \delta(x-n) e^{ikx} dx.$$

Using the relation $\sum_{n=-\infty}^{\infty} \delta(x-n) = \sum_{m=-\infty}^{\infty} e^{-2\pi mx}$

$$\sum_{n=-\infty}^{\infty} f(n) e^{ikn} = \int_{-\infty}^{\infty} f(x) \sum_{m=-\infty}^{\infty} e^{-2\pi mx} e^{ikx} dx,$$

and reordering the sum

$$\sum_{n=-\infty}^{\infty} f(n) e^{ikn} = \sum_{m=-\infty}^{\infty} \int_{-\infty}^{\infty} f(x) e^{i2\pi(\frac{k}{2\pi}-m)x} dx.$$

Notice that the integral is Fourier transform then we get,

$$\sum_{n=-\infty}^{\infty} f(n) e^{ikn} = \sum_{m=-\infty}^{\infty} \hat{f}\left(\frac{k}{2\pi} - m\right)$$

Q.E.D.

B.2 Common Fourier transforms

Function	Fourier transform unitary, ordinary frequency	Fourier transform unitary, angular frequency	Remarks
$f(x)$	$\hat{f}(\xi) = \int_{-\infty}^{\infty} f(x)e^{-2\pi i x \xi} dx$	$\hat{f}(\omega) = \frac{1}{\sqrt{2\pi}} \int_{-\infty}^{\infty} f(x)e^{-i\omega x} dx$	
$\text{rect}(ax)$	$\frac{1}{ a } \cdot \text{sinc}\left(\frac{\xi}{a}\right)$	$\frac{1}{\sqrt{2\pi a^2}} \cdot \text{sinc}\left(\frac{\omega}{2\pi a}\right)$	where $\text{sinc}(x) = \sin(\pi x) / (\pi x)$.
$e^{-ax} S(x)$	$\frac{1}{a+2\pi i \xi}$	$\frac{1}{\sqrt{2\pi(a+i\omega)}}$	The function $S(x)$ is the Heaviside unit step function and $a > 0$.
$e^{-\alpha x^2}$	$\sqrt{\frac{\pi}{\alpha}} \cdot e^{-\frac{(\pi \xi)^2}{\alpha}}$	$\frac{1}{\sqrt{2\alpha}} \cdot e^{-\frac{\omega^2}{4\alpha}}$	For this to be integrable we must have $\text{Re}(a) > 0$.

Table B.1: Fourier transform of function found in the text.

Glossary

- CBVT** cone beam volumetric tomography. 26
- coherence length** . 6
- FDL** Fourier delay line. 11
- FDOCT** Fourier domain optical coherence tomography. 13, 16
- FRC** fiber reinforced composite. 22
- FSR** free spectral range. 48, 49
- FWHM** full width half maximum. 6, 64, 81
- GVD** group velocity dispersion. 12
- OCT** optical coherence tomography. 1, 21
- PIC** photonic integrated circuit. 42
- PSD** power spectrum density. 6, 17
- RES** ring enhanced spectrometer. 86
- slab waveguide** . 41
- SROCT** spectral radar optical coherence tomography. 1, 18
- TDOCT** time domain optical coherence tomography. 1, 9, 13, 15
- TE** transversal electric. 45
- TM** transversal magnetic. 45
- WDM** wavelength division multiplexer. 59, 68, 74, 75